PHOTONICS

Review of Undergraduate Research

Contributions from undergraduate research experiences within the
NSF Center on Materials and Devices for Information Technology Research

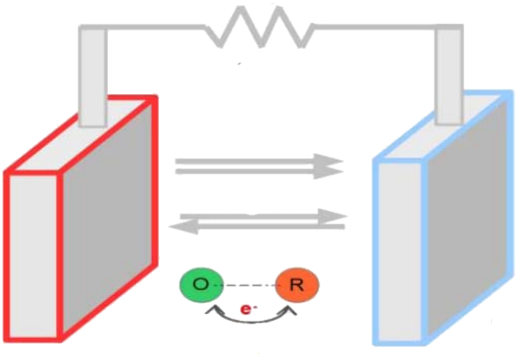

Volume 9, Number 1

This material is based upon work supported by the STC Program of the
National Science Foundation No. DMR 0120967.

Printed in the United States at the University of Washington, Seattle, WA.

Inquires should be addressed to:

Chemistry Department
University of Washington
Department of Chemistry
Box 351700
Seattle, WA 98195-1700

hopreu@uw.edu

http:hookedonphotonics.org

Volume 9, Number 1

Table of Contents

Welcome to the Eighth Edition of
Review of Hooked on Photonics Undergraduate Research

This volume features extended abstracts written by student participants in the National Science Foundation (NSF) Center on Materials and Devices for Information Technology Research (CMDITR) Summer 2012 Research Experiences for Undergraduates (REU) program: Hooked on Photonics (HoP).

The REU experience is intended to serve as a catalyst for undergraduates to enter into careers involving science, technology, engineering, and mathematics. Hooked on Photonics placed undergraduate students from across the United States in research laboratories at the University of Washington, the University of Arizona, and the Georgia Institute of Technology. All of the participants worked on interdisciplinary research projects that contributed to advancements in information technology encompassing activities in chemistry, physics, optics, materials science and engineering. The program emphasized the teamwork nature of scientific research, and was supplemental by a collection of activities including ethics training and workshops in scientific communication.

HoP provides a rich learning opportunity not only for the undergraduate participants who experience hands-on research prior to committing to graduate study, but also for the student's mentors, be they faculty members, research scientists, post-doctoral fellows or graduate students. While working with REU students, mentors develop teaching and mentoring skills, and benefit from reflecting on the excitement of the cutting-edge research upon which their careers have been built.

This publication offers a forum for participants to share their research with their peers, future students, graduate students and faculty, and others interested in the research activities of the Chemistry Department. To learn more about Hooked on Photonics please visit *hookedonphotonics.org.*

A special thanks to all of the students for their hard work, to their mentors for their time and patience, and to the REU program coordinators for their organizational efforts.

The extended abstracts included here are presented in alphabetical order by the participant's last name.

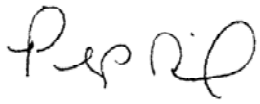

Philip Reid, Hook Program Coordinator

Power Consumption Accounting of Aggregation Nodes in an Optical Network

SEAN ASHLEY, University of Arizona
Dr. Jun He, Weiyan Mo, Dr. Nasser Peyghambarian, University of Arizona

Introduction

Information and communication technology (ICT) contributes 8-15% of the energy consumption[1] in the UK and the US while contributing 3-5% to the world's energy consumption[2]. ICT advancements are increasing the amount of data traffic that networks can handle at an exponential rate. As a result, the networks' demands for power are growing just as fast. Currently, the rate of innovation in green networking technology will not be able keep up with the growing power demand[3]. ICT needs advancement in energy-efficient networking technology to be sustainable.

The common layout of todays' optical networks is an integration of optical and electrical devices[4], utilizing the fibers' high-bandwidth in data transmission and electronics' ability to facilitate complex switching and routing processes. But, modern revolutions in all-optical routing and switching are making networks even faster and even more versatile[5]. This moves optical aspects of networking closer to the end-user from the core network down to the access and aggregation network levels. Energy-aware processing technologies, such as power-aware routing and wavelength assignment (PA-WRA) and selective switch-off controls, contribute to a smarter and more energy-efficient optical network.

The purpose of this project is to create a comprehensive accounting of the power consumption of the equipment in CIAN's Testbed for Optical Aggregation Networking (TOAN) lab. The project will focus on the Fujitsu's *Flashwave 9500* (FW), which functions as an aggregation node in an optical network. Aggregation nodes are hubs in a network where various types of data packets are sent from the source client to the aggregation node. As the many types of data crosses from the client-side to the network-side of the node, the data is reformatted and then sent out towards the data packets' destinations. The FW nodes are each made of several components that allow the FW to be able to handle and route different data packets. Some components are compact pieces of equipment, usually called line-cards, while others are bulkier. Accurate data on power consumption of the smaller individual components and of the larger sub-systems will provide a thorough reporting on the power consumed by the node. Establishing a bank of data will be a tangible product from this project, from which information can be pulled to supplement future studies on increasing the energy-efficiency of optical networking. But, beyond just data-collecting, completion of this project will establish a better understanding on power consumption in optical ICT devices.

The FW nodes in the TOAN lab can be seen as samples of industrialized aggregation nodes which are active systems working in commercial optical networks. Investigating how the FW nodes use power provides insight into the energy use in a vital piece of an optical network, adding to the understanding of power consumption in entire optical networks.

A FW node is divided into a high-density shelf (HDS) and a photonic shelf (PhS). The HDS holds the following components which are called line-cards:

- *IFP5-ETA1:* 10GbE network-side narrow-band transceiver that transmits data between the FW node and the wavelength-division multiplexer (WDM). The ETA1 is selective to only a single wavelength.
- *IFP5-EXX1:* 10GbE network-side no-mux transceiver capable of transmitting data between the two nodes without the WDM.
- *IFP5-TGD1:* 8+1 muxponder with built-in WDM functionalities and can transmit data without the switch fabric unit (SWF).
- *IFP5-EGS1:* 20 1GbE port client-side transceiver with 20 ports available to relay data between the client and the SWF.

The wavelength-selectable switch (WSS) and ROADM amplifier unit are also line-cards on the HDS but they function more closely with the PhS.

The SWF is an electronic switch fabric which facilitates communication between the line-cards through the node's backplane. The EoS mapper provides an interface between SONET and Ethernet signals through the SWF.

The PhS houses the following components except the WSS and ROADM amplifier. These components facilitate reconfigurable optical add-drop multiplexing (ROADM) operations.

- *WDM:* Multiplexes and de-multiplexes up to 44 optical signals and sends/receives high bandwidth signals to/from the WSS.
- *WSS:* The WSS balances the output signal by operating on each wavelength.
- *ROADM Amplifier Unit:* Amplifies the output signal from the WSS.
- *Physical Inventory Unit:* Communicates between the photonic shelf PhS and HDS.
- *Dispersion Compensation Module (DCM):* Reduces the adverse effects of optical dispersion in the signal.

All of the components above constitute the ROADM system.

The management unit controls the backstage processes and operations of the node, such as assigning, provisioning, and lighting alarms on the line-cards. From a network management computer, the *NetSmart 500* software allows the user to command the management unit to carry out those operations while displaying the status of the line-cards and signal quality reported by the management unit.

Experimental Methods

The power supply (PS) rectifies the AC power coming from the outlet and becomes a DC power source for the circuit breaker panel (CBP). The CBP carries the DC power source to the FW nodes while monitoring for spikes in voltage or current. I used the *ExTech 382065 Clamp-On Power Meter* as a multimeter to measure power. The multimeter measures current flowing from the CBP to the individual nodes through the black wires -- illustrated in Figure 1 -- and measures the voltage across the node's terminals. Multiplying the readings for current and voltage together produces the node's measured power consumption. Figure 1 shows the multimeter set up to measure node 1's power consumption.

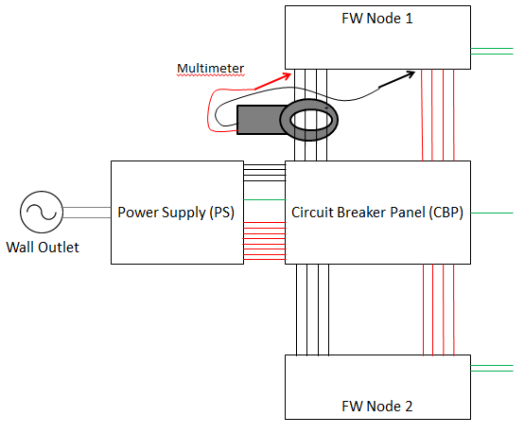

Figure 1. Schematic of power supply from a U.S. wall outlet to the FW nodes. Black wires feed current from the source toward the nodes. Red wires carry the current from the nodes back out to the source. Green wires represent grounding wires. Green wires on the far right are connected to the FW's frame.

The power consumption of the smaller components in a node is derived from fluctuations in the node's power consumption as the component's state is altered. Measuring power after removing a line-card from the FW node and then again after re-equipping the line-card provides data from which we can conclude how much power the line-card consumes when it is equipped but unassigned. Then, after fully provisioning the line-card, the power consumption is measured. The resultant change is used to calculate how much power a fully provisioned line-card consumes relative to the card being unassigned.

The procedure for measuring how much power line-cards consume while handling data traffic is similar. First, a specific data path is set up between the two nodes. Connecting involved components – such as the IFP5-ETA1, ROADM system, or SWF – with optical fiber establishes physical connections. Logical connections and data services between components are established through the *NetSmart 500* software. Then, power measurements are taken for each node with the involved line-cards fully provisioned and with no data traffic flowing through the system. Finally, the traffic generator sends data through the system. The data return to the traffic generator where data rate and traffic directions are measured. Data rate, traffic direction, and power consumption is recorded.

Figure 2 shows an example of one configuration of an established and functioning data path.

For any configuration of the network, many components are involved in the transmission of data. Because of the design of the FW, the power consumption of individual components cannot be directly measured. To circumvent this, fluctuations in power consumption are measured for many different configurations. Comparison of the different behaviors in power consumption between the configurations will reveal the power behaviors of the individual components. And, because of the complexity of the network, there is a proportional uncertainty in measurement. To reduce uncertainty, each configuration is tested several times.

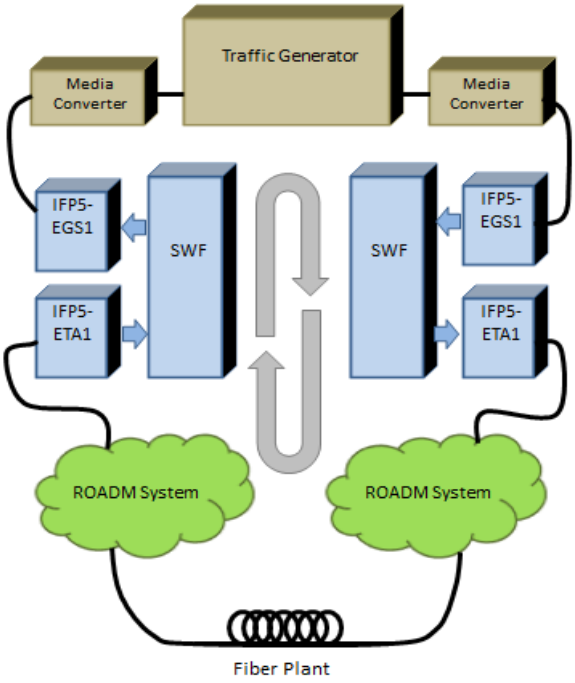

Figure 2. A tested data path example. Brown models are traffic generation devices. Blue models are components on the HDS of a node. Green clouds are the ROADM system. One-directional traffic flows in the direction of the grey arrows. The fiber plant holds large spools of optical fiber to simulate long distance between the two nodes.

Results and Discussion

(The tests produced a comprehensive "cumulative data table" which lists the power consumption of the various components of the FW in different modes and data rates. Notable results pertaining to the power-related nature of the FW are incorporated into this abstract and represent only a small portion of numerical information which can be found on the cumulative data table.)

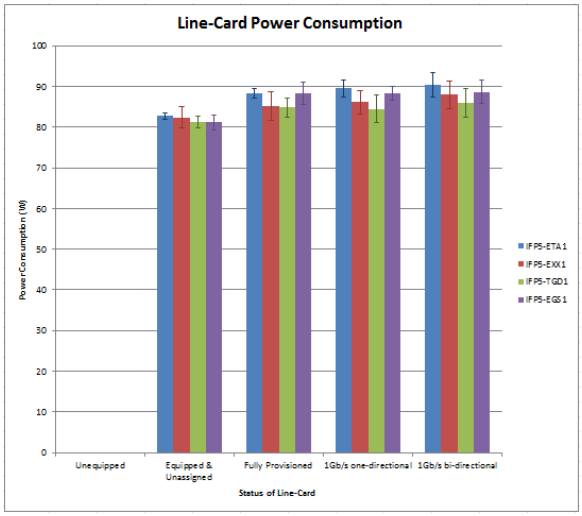

Graph 1. Graph of line-card power consumption versus the condition in which the card was measured. Error bounds shown reflect approximate 95% confidence intervals.

As shown in Graph 1, there is a tendency for the average power consumption of the line cards to increase as they progress from being unassigned to fully provisioned and from handling 1 Gb/s of one-directional data traffic to 1 Gb/s of bidirectional data traffic. However, differences in power are within the error of my measurements, so a definitive rise in power consumption through these stages cannot be concluded.

The smallest change in current that the multimeter can measure is $\pm$ 0.1A. The FW is designed to maintain a constant 48V voltage across the terminals of a node while changing the flow of current to appropriate the necessary power to the nodes. With this design of the FW, the smallest change in power that the multimeter can confidently measure is $\pm$ 4.8W. Data from Graph 1 indicates that changes in power consumption on the order of watts or 0.1W should be measured to produce confident conclusions. (The team is currently discussing the purchase of a new power meter with finer granularity to achieve greater-precision in results.)

When a line-card is equipped to the FW but unassigned, it will consume relatively the same amount of power as when the line-card is handling one or two gigabits per second of data traffic. I believe this is because the FW is designed to always be sending a carrier wave through its system. A product manager from Fujitsu verified that there is constant light provided by the smaller SFP modules in each line-card. This carrier wave allows the FW's management unit and *NetSmart 500* to constantly

monitor signal quality and strength even when no data traffic is flowing through the system. In regards to power consumption, the FW and its cards are always in an "on" mode. Data is sent by modulating the wave and this modulation causes the small variations in power consumption. This design helps prevent current and voltage spikes on start-up, decreases the delay to start data transmission, and reduces complications involved with repetitive warming-up of optical amplifiers and other optical components in the FW.

One of the tests carried out in this project is arbitrarily called the “current drop test”. This test was run because of suspicious drops in amperage which came up during data-logging. The test is designed to investigate long-term trends of the multimeter’s amperage and voltage readings without re-zeroing the meter. There was no data traffic through the FW. The tests did find a decline in both readings and the measurement procedure was changed accordingly. After the 19-hour over-night test, the multimeter was zeroed and I took another power reading. That reading was identical to the power reading at the start of the test. The FW does not seem to have energy-conserving features such as a sleep-mode or selective switch-off function.

1 Gb/s one-directional traffic and 1 Gb/s bidirectional traffic are the only types of data rates tested in this project. Recent developments, however, will allow for greater data rates to be tested within the next few weeks. Testing higher data rates might reveal a clearer trend in the relationship between power consumption and the amount of data traffic through the system.

Conclusions

Our results confirm that the FW does not have energy-saving features. However, despite not having energy-saving features such as a sleep-mode or selective switch-off function, the FW is a leading product in energy-efficient aggregation technology, as exemplified by the FW meeting the Telecommunications Energy Efficiency Ratio (TEER) metric established by the Alliance for Telecommunications Industry Solutions (ATIS)[6]. But, we want future network elements to be even more energy-efficient.

Because of the importance of energy-awareness, we will use the data from our findings to design energy-saving features for network elements, including the FW. Aggregation nodes successfully implementing sleep-mode and selective switch-off functions have the potential to demonstrate even greater energy-efficiencies. Work done in a framework by the Building the Future Optical Network in Europe (BONE) project shows that integration of sleep-modes and switch-off control can result in up to 35% to 40% power savings in low load networks with relatively low chances of path blocking[7]. Industrial partners, such as Fujitsu, show great interest in our work. Collaborating with industry will allow for the speediest application of our findings in commercial networking. We will develop a new algorithm (PA-RWA) and hopefully deploy the algorithm to their products. PA-RWA is another technology that has been tested to be effective in improving power-efficiency[8]. The challenge for future work is to find a way to integrate these energy-saving operations to aggregation nodes without risking damage to the FW that the constant current design prevents.

From our findings, it seems there is not a sufficient focus on energy-conservation in optical communications so far. However, there is significant incentive to pursue studies in energy-efficient optical networking, especially in selective switch-off functions and PA-RWA. Energy-saving features are a requirement for sustainable next-generation optical networks. Research of these technologies is in CIAN’s future work.

References

1. Nannan, Hao. *Green ICT Applications and Development*. In Beijing, China, 2 September 2011. ITU/MIIT Seminar on ICT as an Enabler for Creative and Green Economy.

2. Ruth, Stephen. *Reducing ICT-related Carbon Emissions: An Examplar for Global Energy Policy?* Scholl of Public Policy, George Mason University. June 2011.

3. Van Landegem, Thierry. *Reducing the carbon footprint of ICT devices, platforms and networks.* GeSI Global Assembly, 2012. www.greentouch.org.

4. Jajszczyk, Andrzej. *Optical networks – the electro-optic reality*. Department of Telecommunications, AGH University of Science and Technology. Krakow, Poland. 8 November 2004.

5. Johnston, O.J. *Optical Switching: Implementing a Future-Proof Infrastructure.* ONPATH Technologies. www.onpathtech.com

6. *Fujitsu FLASHWAVE® 9500 Packet Optical Networking Platform Demonstrates Low Energy Use, OPEX Savings*. BusinessWire. 28 September 2010. www.businesswire.com.

7. *Final TP report on Green Optical Networking*. Building the Future Optical Network in Europe (BONE). 15 January 2011. www.ict-bone.eu.

8. Kuipers, Fernando; Yang, Song. *Energy-Aware Path Selection for Scheduled Lightpaths in IP-over-WDM Networks*. Delft University of Technology. Delft, Netherlands. www.nas.eqi.tudelft.nl

Acknowledgments

Funds for this research were provided by the Center for Materials and Devices for Information Technology Research (CMDITR) and the National Science Foundation (NSF) Science and Technology Center No. DMR 0120967. I would also like to acknowledge my faculty mentor Dr. Jun He, TOAN lab leader Dr. Massoud Karbassian, graduate student mentor Weiyang Mo, the Hooked on Photonics (HoP) program coordinators Kimberly Sierra-Cajas and Trin Riojas and program assistant Amanda Anderson.

Sean Ashley just finished his first year of undergraduate studies at the University of Arizona where he is pursuing a Bachelor of Science degree in optical Sciences & Engineering and a Bachelor of Science degree in Applied Mathematics.

Magneto Second Harmonic Generation of Magnetite Nanowires

JOEL BAHENA, UC San Diego
Paden Roder, Peter Pauzauskie, University of Washington

Introduction

Magnetite nanowires are biocompatible which makes them suitable as pharmaceutical payloads for nanomedical applications. Moreover, these magnetic nanowires mechanically respond in the presence of a magnetic field, which make them desirable for applications such as MRI contrast agents. When subjected to a magnetic field and irradiated by a laser, it is predicted that these wires could produce magneto second harmonic generation (SHG)[1]. SHG is the process of frequency doubling by symmetry breaking in nonlinear crystal materials. SHG allows for the tracking of nanoparticles in nanomedical applications. Moreover, it has been shown that magnetic materials can exhibit SHG by breaking time reversal symmetry in the presence of a magnetic field. In this study, we attempted to synthesize magnetite nanowires[1], optically trap magnetite nanowires, and probe for magneto SHG.

Experimental Methods

Synthesis

In order to test for SHG, magnetite nanowires were synthesized using a hydrothermal synthesis. The synthesis required reagents consisting of hydrated ferrous sulfate ($FeSO_4 7H_2O$), hydrated sodium thiosulfate ($Na_2S_2O_3 5H_2O$), sodium hydroxide (NaOH), and polyethylene glycol of 4000 mw (PEG)[2].

The initial step of the synthesis was creating a mixture, with a ratio 1:2, of melted PEG to deionized water. The measurements were not exact, and an 18mL solution of the mixture was created consisting of a 1:2.6 ratio of PEG to deionized water. The mixture was then poured into a Teflon lined autoclave. The synthesis also required grinding hydrated ferrous sulfate (1.102795 g) and hydrated thiosulfate (0.46175 g), which was done using a pestle and mortar, and was then poured into the autoclave. NaOH (2.0163 g) was the final reagent poured into the autoclave. Once all reagents were inserted in the autoclave, the autoclave was sealed and placed in an oil bath, which was then heated to 150°C for 24 hours.

Characterization

Various characterization techniques were implemented to confirm the composition and phase of the synthesized nanowires. X-ray diffraction (XRD)[5], Raman spectroscopy[3,4], transmission electron microscopy (TEM), and scanning electron microscopy (SEM), were all used in characterizing the hydrothermally synthesized nanowires.

Separation

In order to trap the nanowires using the optical laser tweezers, a low concentration sample of nanowires is needed. The synthesis required to create magnetite wires leaves a residue of PEG in the solution, and that can cause disruption when trapping nanowires. Three methods were used to create a sample composed mainly of nanowires. The first method was using centrifugation in an attempt to pull the wires to the bottom of an eppendorf, and then drawing off the supernatant. The precipitate was then mixed with deionized and place in a sonicator, and the process was repeated until the best results were achieved. The second method used attempted to utilize magnetite's magnetic properties to pull all magnetic material to the bottom of the eppendorf using a magnet. Similar to the method using centrifugation, the precipitate was then mixed with deionized water and sonicated. This process was also repeated until the best results were acquired. Lastly, Reeve Angel qualitative filter paper was used to filter larger particles from the smaller particles in hopes to retain only nanowires in the solution.

Photoluminescence

Before trapping individual nanowires and testing for magneto SHG, a photoluminescence (PL) spectrum was taken of a concentrated sample of magnetite nanowires. The PL spectra were taken before and

after the presence of a magnetic field with expectations of seeing an indication of SHG.

Optical Laser Tweezers

To test for magneto SHG, optical laser tweezers were used to trap individual magnetite nanowires.

Once the nanowire was trapped a magnetic field was applied, by placing a magnet near the sample, in hopes of producing SHG. Since the laser used in the optical tweezers has a wavelength of 975 nm, an output with wavelength of 487.5 nm, which should be a blue luminescence, was expected once the magnetic field was applied.

Results and Discussion

Nanowires

The synthesis produced various wires of all sizes including residue of PEG. A particular trait of these nanowires was that they would aggregate which could be because of their small size, but also because of their magnetic properties. Figure 1 shows the various wires synthesized along with displaying their aggregating attributes.

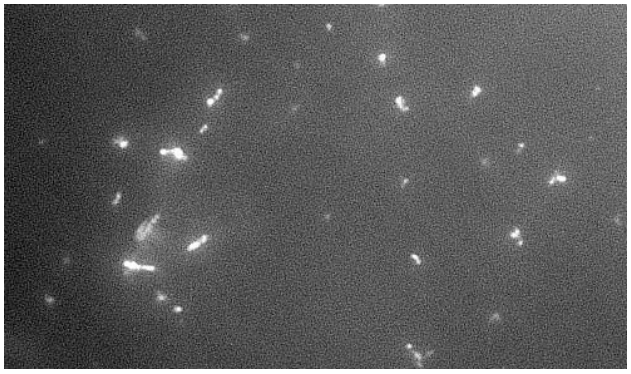

Figure 1. A Dark field image of nanowires synthesized using hydrothermal synthesis.

Characterization

The first test completed in characterizing the nanowires was Raman spectroscopy. The results indicated that the synthesized nanowires were hematite (Fe_2O_3)[3], another phase of iron oxide. While the results from Raman spectroscopy indicate that the nanowires were hematite, XRD results demonstrated that the sample consisted of a high concentration of magnetite nanowires along with a lower concentration of hematite nanowires. Studies have shown that magnetite oxidizes at higher temperatures[6], and we believe that the laser from Raman spectroscopy could have caused the magnetite to photo-thermally oxidize to hematite.

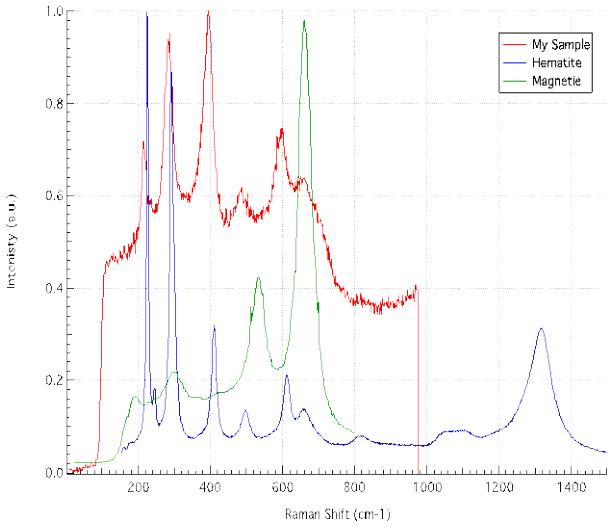

Figure 2. The results from Raman spectroscopy that indicate that the synthesized nanowires are hematite nanowires.

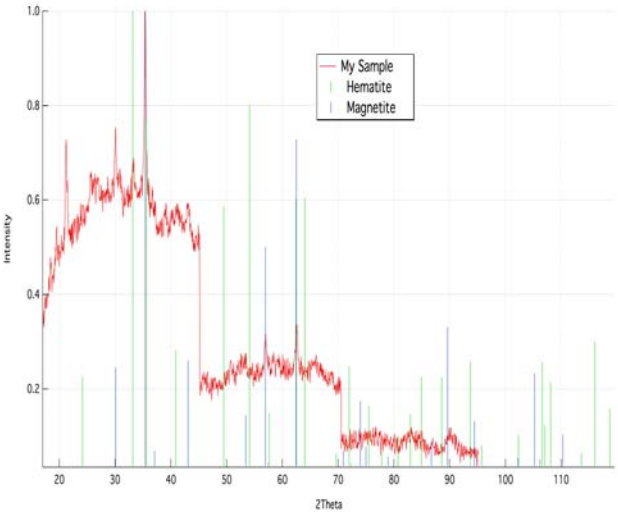

Figure 3. The XRD results of the synthesized nanowires[3,4].

Separation Results

The separation method involving centrifugation did not show evident separation of the nanowires and PEG. While the second method of using a magnet to separate the nanowires from the PEG residue supplied better results in comparison to the centrifugation method, the results were not satisfactory for trapping in the optical laser tweezers. The final method of using filter had the

best results of all three methods, and produced a solution that consisted primarily of nanowires.

Photoluminescence Results

PL spectra of the magnetite wires were collected to indicate SHG in the presence of a magnetic field. Tests were done before the magnetic field was applied and is shown in figure 4 below. It was expected to see a spike with the presence of a magnetic field at 487.5 nm wavelength point on the graph which is half the wavelength of the 975 nm wavelength infrared laser that was used during the PL testing. The graphs show an increase in intensity, but we believe that is a result of the configuration of the testing. In order to apply the magnetic field, a magnet was held as a minimal distance from the sample, which could have caused reflection that would have caused unwanted signals to be detected. Therefore we believe that we did not receive the SHG signal that we were expecting in the PL spectra.

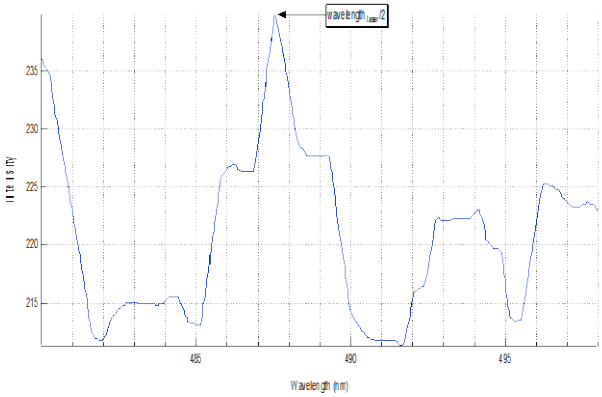

Figure 4. PL spectrum of magnetite nanowires without magnetic field.

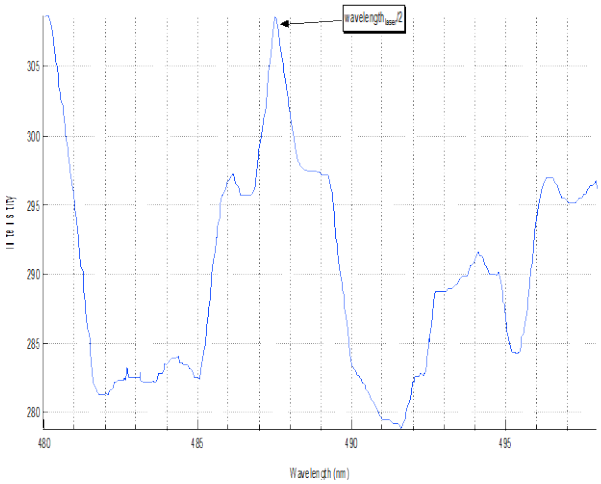

Figure 5. PL specturm of magnetite nanowires with magnetic field[5].

Trapping Results

After PL spectra was analyzed, we attempted trapping individual magnetite wires using optical laser tweezers. Through seperation using filter paper we had an appropiate sample to use in trapping. After many attempts we were able to trap a magnetite nanowire. Figure 6 shows a single nanowire trapped in the optical laser tweezer. Once trapped a magnet was placed near the site of the sample to induce SHG. Testing showed that there was no sign of SHG when we the sample the magnetic field.

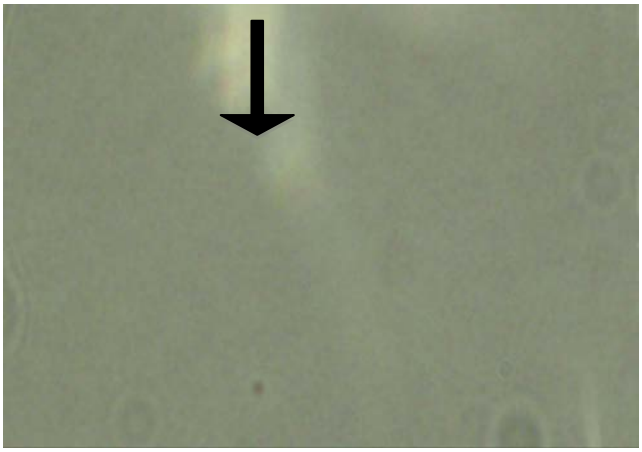

Figure 6. Image of trapped magnetite nanowires.

Conclusions

While we did not detect a magneto SHG of the magnetite nanowires, we believe that the problem arises from not having a strong enough localized magnetic field during our PL testing and optical trapping. We are convinced that if we had designed a loop, like the one imaged in figure 7, we could have produce a stronger localized magnetic field. This stronger magnetic field could have potentially improved upon the initial results, and we would have possibly been able to produce SHG.

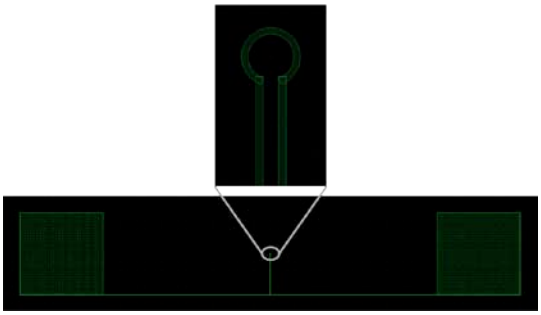

Figure 7. CAD drafted loop that could potentially increase localized magnetic field in our testing.

References

1. McGilp, J.F et al., Journal of Magnetism and Magnetic Materials 2010, 322 1488–1493

2. Harraz, F.A, Physica E 2008, 40, 3131–3136

3. de Faria, D.L.A; Silva, S.; de Oliveira, M.T, Journal of Raman Spectroscopy, 1997, Vol. 28, 873-878,

4. Shebanova, O.N; Lazor, P., Journal of Raman Spectroscopy, 2003, Vol. 34: 845–852

5. Crystallographic and Crystallochemical Database for Minerals and their Structural Analogues, http://database.iem.ac.ru/mincryst/index.php (accessed August 2, 2012)

6. Lepp, H., The American Mineralogist, 1957, 42.

Acknowledgments

Funds for this research were provided by the Center on Materials and Devices for Information Technology Research (CMDITR), and the NSF Science and Technology Center No. DMR 0120967. I would like to thank Peter Pauzauskie and Paden Roder for guidance in my research. I would also like to thank Bennet Smith for helping with the characterization of my samples.

JOEL BAHENA is a junior NanoEngineering major at the University of California, San Diego. Upon gradauation, he plans to pursue a Masters in NanoEngineering.

Carbon Nanotubes for Ultrafast Fiber Lasers: Separation, Spectroscopic Analysis, and Integration

KRISTEN E. BAILEY, Central Methodist University
Palash Gangopadhyay, Kaushik Balakrishnan, Khanh Kieu, and Robert A. Norwood, University of Arizona

Introduction and Objective

Carbon nanotubes (CNT) were first identified in the 1970's as carbon filaments in the core structure of vapor-grown carbon fibers; these initial CNTs were multi-walled. In 1993, single-walled CNT were synthesized, which brought about many experiments to characterize these small structures. Starting in the early 1990's, a number of research groups have been devoted to analyzing CNTs in accordance with their synthesis, structure, properties and applications[1]. CNTs are basically sheets of graphene rolled up to form a tube (Figure 1). From the different ways of rolling the sheet up, there are numerous combinations of CNT structures possible. Amongst these combinations the electrical characteristics can be classified into two types of CNTs, metallic (MCNT) and semiconducting (SCNT).

Over the last decade carbon nanotubes have become increasingly popular in various optical, electronic, and opto-electronic applications. While CNT are exceptional materials, there is some concern with respect to the predictability of properties when applied to a specific application. Researchers have theorized that if CNT were to be separated into their metallic (MCNT) and semiconducting (SCNT) varieties, much better control over CNT performance could be acheived[2]. The key challenge in making this process commercially amenable is that the procedure for separating the CNTs is very time consuming and expensive.

The objective of this research is to separate metallic and semiconducting carbon nanotubes from a commercially available mass of CNTs in a relatively simple and inexpensive laboratory setup including identification of a set of easily accessible characterization tools that can be used to discriminate MCNT from SCNT. After successful completion of the separation procedure, optical devices, such as an ultrafast fiber laser[3], will be assembled using either pure MCNT or pure SCNT as the saturable absorber; it is hypothesized that a fiber laser using exclusively one type of CNT as a saturable absorber will have superior performance, in particular the possibility of operating with lower pump laser power threshold, thereby improving the efficiency of the laser. Further, the identification of the type of nanotube responsible for the good performance metrics will enable high reliability from the CNT fiber lasers.

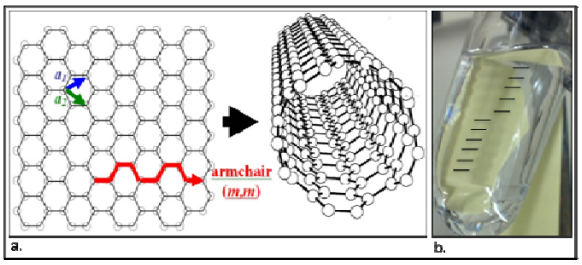

Figure 1: (a) Structure of CNTs and their rolled confirmation. (b) Step density gradient.

Research Methods

2.1 Linear Density Gradient

In our research approach, CNT separation was performed using the linear density gradient separation technique. It has been demonstrated that the proper surfactant can separate single walled CNT mixtures into MCNT and SCNT through this technique[2]. The density gradient medium was made by stacking solutions of Optiprep 60% w/v iodixanol and 2% w/v sodium cholate (SC) with increasing densities from 8% (w/v) at the top to 35% (w/v) at the bottom for every 3% resulting in 10 different layers in increasing density from top to bottom (Figure 1). The original 60% Optiprep solution was used as a stationary layer at the bottom to cover the hemispherical bottom of the centrifuge tube. The 20% (w/v) layer at the center initially receives the CNT. By stacking each layer, a step density gradient medium was created which was allowed to settle for 3-4 hours. Within this period the layer interfaces diffused into each other to create a uniform linear density gradient, an important step required for efficient separation of the CNT

step required for efficient separation of the CNT (capped with surfactants) based on their buoyant densities. The efficiency and yield of this process depends on the CNT diameters, electronic properties and their ability to bind with specific surfactants. The reported procedure produces only microgram (μg) quantities of separated and pure MCNT and SCNTs. One of the key objectives of this research was to scale up this process to the milligram level by using a larger centrifugation bottle and finer density steps.

2.2 Analysis

Once there is enough MCNT and SCNT separated, tests are done to examine their optical properties (absorption spectroscopy), structure (Raman and photoluminescence spectroscopy), diameter and length (transmission and scanning electron microscopy techniques). Most of these tests, except for absorption spectroscopy, are conducted at the University Spectroscopy and Imaging Facilities (USIF) on the University of Arizona campus.

2.3 Incorporation in the Fiber Laser

Once the properties of the separated CNTs are characterized, they can be incorporated into specially fabricated optical fiber tapers and incorporated into fiber laser devices. Before the current work, ultrafast lasers used a random mixture of CNTs as the saturable absorber. This causes a lot of uncertainty with respect to laser performance, since the mixture was random and of unknown compositions, leading to uncontrollable variations in spectral performance from batch to batch. For this experiment, the separated CNT will be used as a saturable absorber in a short pulse laser. Each type of CNT is washed with distilled water and isopropanol. Once cleaned, all liquid is removed and the tubes are placed in the oven at 72°C until CNT are dry. The CNT are then dispersed in a small amount of THF, to which the polymer PDMS is then added drops at a time, until reaching the right consistency. From there, the mixture is pulse sonicated until the THF is evaporated off. This step allows for dispersing the CNTs into the polymer. Khanh Kieu, Assistant Professor in the College of Optical Science at the UA, will then take the polymer and incorporate it into his short pulse laser[3] by coating a custom fabricated fiber taper with the polymer-CNT mixture. The laser is a mode-locked 1550nm laser. If this research supports the hypothesis that one CNT will have a better performance, then this technology could be inserted into a commercially available fiber laser platform.

Results and Discussion

3.1 Linear Density Gradient

After performing the density gradient steps, the separation of CNTs was evident by the different fractions on the as-prepared gradient column. With the results, further separation was able to ensue because the results showed some signature peaks of CNTs. Despite reasonable separation of the various fractions, the yields were relatively low, impeding detailed analysis of and the ability to fabricate a number of laser devices using these separated CNTs. Further separation into large quantities of metallic and semiconducting CNT was not pursued due to time constraints. In order for that separation to occur, multiple loops of the density gradient separation would be necessary, using the collected CNT as the middle layer. The present attempts at separation only produced a few μg of CNT.

3.2 Analysis

Since very few CNT were purified and separated, this group analyzed MCNT and SCNT that Dr. Palash Gangopadhyay had separated previously. After analyzing the already separated MCNT and SCNT, the results were as follows. TEM did not produce a clear image due to the fact that there were considerable amounts of surfactant still "glued" to the CNT. STEM analysis, however, shows that CNTs are indeed present in the separated fractions. Figure 2 shows the bundles of CNTs from such an analysis of SCNTs. The Raman spectra showed signature peaks from both the MCNT and the SCNT, which meant that the CNTs were of high quality (Figure 2). Absorption spectroscopy was used in identifying the wavelengths at which each

CNT would absorb light (Figure 3). Our data here from Raman, TEM, and absorption spectroscopy are consistent with the reported separation of the CNTs[2] using similar approaches.

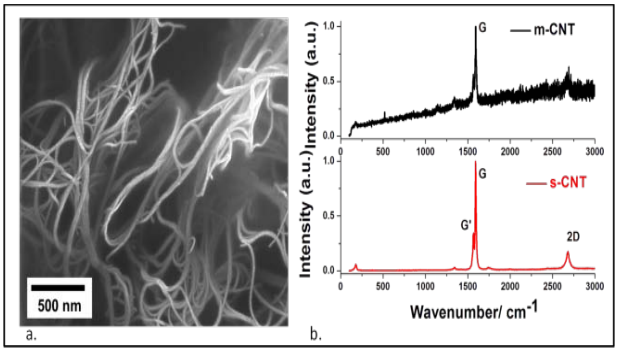

Figure 2: (a) STEM image of bundles of SCNTs. (b) Raman spectra of both MCNT and SCNT.

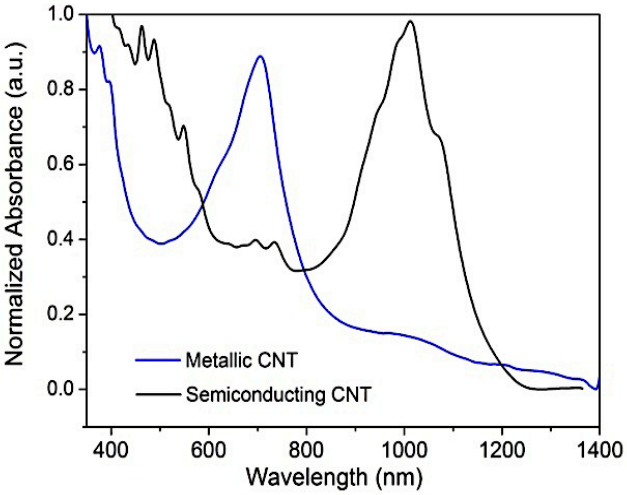

Figure 3: Absorption spectra of both MCNT and SCNT.

3.3 Incorporation in the Fiber Laser

The culmination of this summer research on separating and analyzing CNT was inserting the separated CNTs into an ultrafast laser to function as saturable absorbers, which are needed for creating a periodic train of ultrashort (< 1 picosecond) pulses. Both MCNT and SCNT were first dispersed in THF and finally into the polymer PDMS. The CNT containing polymer was then wrapped around the fiber taper (Figure 4) and inserted into the laser by fusion splicing. The CNTs act as the saturable absorber for the laser. The fiber taper is still being prepared and then it will be incorporated into the laser setup. Measurements will be taken to confirm if one type of CNT performs better than the other as well as the original mixture of CNTs originally used in the laser.

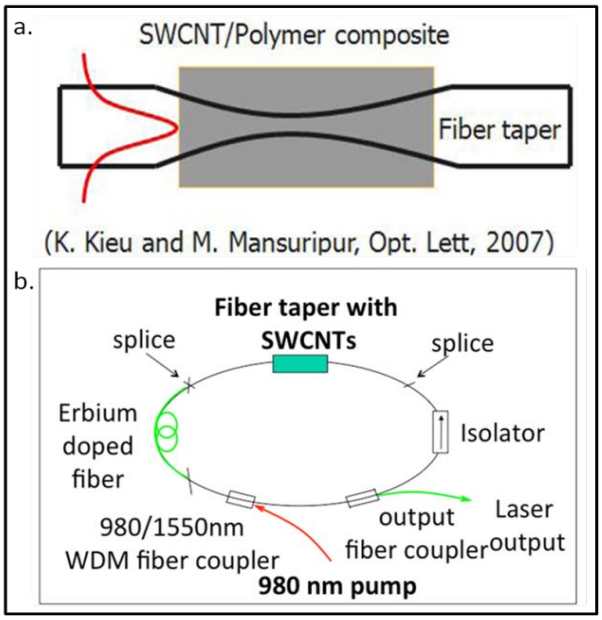

Figure 4: (a) Fiber taper of single-walled CNT/polymer composite. (b) Ultrafast fiber laser setup.

Conclusions

Although, at present we have been successful in separating the as-purchased CNTs into MCNT and SCNT, the yields of the processes are low and need substantial development for the large-scale separation for practical applications. Large batch separations are not refined enough at this point in order to be provide sufficient separation of the CNTs. The microscopic and spectroscopic analysis of both CNTs confirmed that the CNTs were indeed separated and very clean. While the laser integration is still underway, the separated CNTs will provide valuable fundamental information pertaining to their applicability in ultrafast laser technology. (R. Saito, 2011)

References

1. R. Saito, M. H. (2011). Raman Spectroscopy of Graphene and Carbon Nanotubes . *Advances in Physics*, 413-550.

2. Arnold, M. S., Green, A. A., Hulvat, J. F., Stupp, S. I., & Hersam, M. C. (2006). Sorting carbon nanotubes by electronic structure using density differentiation. *Nature*, 60-65.

3. Green, A. A., Duch, M. C., & Hersam, M. C. (2009). Isolation of Single-Walled Carbon Nanotube Enantiomers by Density Differentiation. *Nano Research*, 69-77.

4. Heller, D. A., Barone, P. W., Swanson, J. P., Mayrhofer, R. M., & Strano, M. S. (2004). Using Raman Spectroscopy to Elucidate the Aggregation State of Single-Walled Carbon Nanotubes. *J. Phys. Chem*, 6905-6909.

5. Kieu, K., & Mansuripur, M. (2007). Femtosecond laser pulse generation with a fiber taper embedded in carbon nanotube/polymer composite. *OPTICS LETTERS*, 2242-2245.

6. R. Saito, M. H. (2011). Raman Spectroscopy of Graphene and Carbon Nanotubes . *Advances in Physics*, 413-550.

Acknowledgments

The Center for Materials and Devices for Information Technology Research (CMDITR), NSF Science and Technology Center Grant No DMR-0120967 provided funds for this research. I wish to thank the *Hooked on Photonics* REU program for giving me this opportunity to conduct research and the USIF team for helping me with the TEM, STEM, and Raman.

KRISTEN BAILEY is a senior chemistry major with an education minor. She would like to pursue a graduate degree and someday teach at the university level.

Increased Surface Contact to Carbon Nanotube Arrays from Solvent Evaporation

DENZELL BOLLING, Georgia Institute of Technology
Parisa P.S.S. Abadi, Thomas L. Bougher, and Baratunde A. Cola, Georgia Institute of Technology

To ensure the functional integrity of many computer products it is necessary to dissipate the heat generated by that device's microelectronics via thermal conduction. Carbon nanotube (CNT) thermal interface materials (TIMs) could facilitate that heat conduction more effectively than the typical metal soldering solution since CNTs are more mechanically pliable than most metal solders. The difficulty with using CNTs within an interface lies in producing sufficient thermal contact because variability in CNT heights within an array can preclude many CNTs from bridging the interface gap. The objective of this study is to determine the effects on CNT interfacial contact area and thermal resistance when a CNT array is pressurized in the presence of a solvent that is evaporated from the interface under pressure. A photoacoustic (PA) technique was used to measure thermal contact resistance and distinguish the effects of changing interfacial contact area on thermal resistance. Three different types of PA measurements were performed: 1. Dry contact measurements where Ag foil is placed atop CNT arrays grown on silicon substrates. 2. Dry contact measurements taken after compressing CNT samples at 20 psi and 100 psi. 3. Dry contact tests conducted on CNTs that were compressed at 20 psi and 100 psi with toluene wetted to and evaporated from the CNTs under pressure. Each set of samples was tested in the PA cell at 1 psi and 20 psi of contact pressure. Results show that solvent evaporation from CNT arrays under pressure increases the length of CNT contacts to the interface surface, which produces an increase in contact area and a substantial reduction in thermal resistance compared CNT arrays that were not exposed to solvent.

Acknowledgments:
I would like to acknowledge the Center on Materials and Devices for Information Technology Research (CMDITR), the NSF Science and Technology Center No. DMR 0120967, and the 3M Company.

Synthesis and Optical Characterization of Small TricyanopyrrolineChromophores Based on 4-(diethylamino)-2-hydroxybenzaldehyde

HANNAH BUEHLER, Luther College
Nathan Sylvain, Larry Dalton, University of Washington

Introduction

Nonlinear optical (NLO) chromophores, the component responsible for signal interconversion in electro-optic (EO) devices, are currently of great interest in the fields of materials and optics. The most efficient NLO chromophores are those with high NLO susceptibility, fast response time, a low dielectric constant, small dispersion in the refractive index, structural flexibility, large bandwidth, and ease of material processing.[1] In order to manufacture efficient electro-optic (EO) devices, the most favorable chromophores also have high microscopic molecular nonlinearity, thermal and photo stability, low absorption, and weak electrostatic interaction in polymer matrix.[1] The chromophores are incorporated into the EO devices by way of polymer films which require that the chromophoresalso be soluble in organic solvents suitable for this application.

The effectiveness of an NLO chromophore is determined by its hyperpolarizability (β) on the molecular level and by its EO response (r_{33}) on a macroscopic level.[2]The first molecular hyperpolarizabilty, β, is determined by the strengths of the donor and acceptor and by the length and type of bridge employed.[2,3] The tricyanopyrroline (TCP) acceptor has been shown to exhibit high microscopic nonlinearities when used in NLO chromophores.[3] It would be expected that these chromophores, with their high β values, should have correspondingly high r_{33} values[3] but this has not been found to be the case.[1,2,3,4] These donor-π-acceptor, or push-pull chromophores, adopt nearly planar geometries allowing for very pronounced electrostatic interactions leading to centrosymmetric, or antiparallel, alignment.[1,3,4] This alignment gives rise to the formation of dimers and aggregates that do not dissociate, even under a poling field.[4] Because of this, the r_{33} value of the chromophores is greatly diminished, making them much less efficient. Another problem with these chromophores is their poor solubility in most organic solvents, making it difficult to incorporate them into devices.[3]

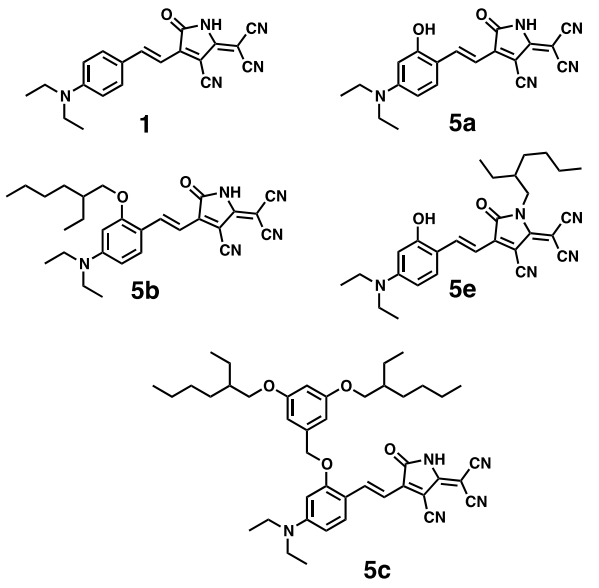

Figure 1.Chromophores investigated during the study.

A series of chromophoreswere synthesized based on 4-(diethylamino)salicylaldehyde (Figure 1). This provided a base where the effects of bulky substituents could be tested as to their efficacy in improving solubility and inhibiting electrostatic interactions, thusreducing the formation of aggregates.

Experimental Methods

Materials and characterization

All the reagents were used as received unless stated. 1H NMR spectra were determined by a Bruker AV300 (300 MHz) NMR spectrometer; MS spectra were obtained via ESI (electrospray ionization) on a Bruker Esquire Ion Trap

spectrometer. UV-Vis spectra were performed on a Shimadzu UV-1600 photo spectrometer and films were imaged with a Zeiss Axiolab A reflected light microscope.

Product was placed in vacuum oven at 64°C overnight. 5c.3,5-bis[(2-ethylhexyl)oxy]-benzenemethanol(0.360g, 0.987mmol) and tetrabromomethane (0.457g, 1.38mmol) were

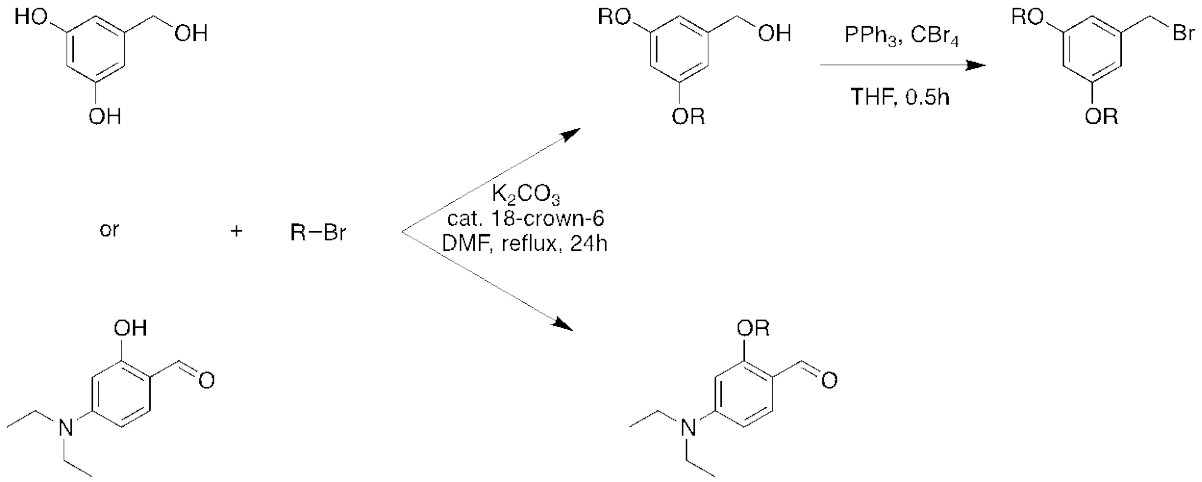

Scheme 1. Syntheses of dendrimers and substitution of 4-(diethylamino)-2-hydroxybenzaldehyde.

Syntheses

5a. The malonitrile dimer (0.737g, 5.58mmol), ethyl pyruvate (1.990g, 17.14mmol), and methanol (1mL) were refluxed under nitrogen for 20 minutes at 70°C. After the 20 minutes, 4-(diethylamino)salicylaldehyde (0.812g, 4.20mmol) was added to the reaction. The solution was refluxed under nitrogen for 2 hours at 70°C. The reaction was then removed from the heat. The green product was filtered and washed with methanol and isospropanol until the filtrate appeared clear. Product was placed in vacuum oven at 64°C overnight. (0.582g, 38.5% yield)

5b.The malonitrile dimer (0.289g, 2.19mmol), ethyl pyruvate (0.640g, 5.51mmol), and methanol (1mL) were refluxed under nitrogen for 20 minutes at 70°C. After the 20 minutes, 4-(diethylamino)salicylaldehyde (0.493g, 1.62mmol) was added to the reaction. The solution was refluxed under nitrogen for 2 hours at 70°C. The reaction was then removed from the heat. The green product was filtered and washed with methanol, ethanol, and isopropanol until the filtrate appeared clear. dissolved in THF under nitrogen at room temperature. After all solids had dissolved, triphenylphosphine (0.350g, 1.33mmol) was added. The solution was stirred for 30 minutes, and then poured into water (50mL). The organic phase was extracted with dichloromethane (2 x 50mL), washed with water (1 x 50mL), and dried over sodium sulfate. Solvent was evaporated under vacuum. 4-(diethylamino)salicylaldehyde (0.580g, 3.00mmol), potassium carbonate (0.735g, 5.32mmol), and 18-crown6 (cataclysmic amount) were added. Reactants were then dissolved in dimethylformamide (20mL) and refluxed under nitrogen for 24 hours at 70°C. Reaction was quenched by pouring products into water (70mL). Organic phase was extracted with dichloromethane (4 x 50mL), washed with water (1 x 50mL) and brine (1 x 50mL), and dried over magnesium sulfate. Solvent was removed under vacuum. This constituted product A. The malonitriledimer (0.165g, 1.25mmol), ethyl pyruvate (0.340g, 2.93mmol), triethylamine (0.127g, 1.26mmol), and methanol (1mL) were refluxed under for 10 minutes at 70°C. After the 10 minutes, product A (0.493g, 1.62mmol) was added to the reaction. The solution was refluxed under nitrogen for 2 hours at 70°C. The reaction was then removed from the heat. The

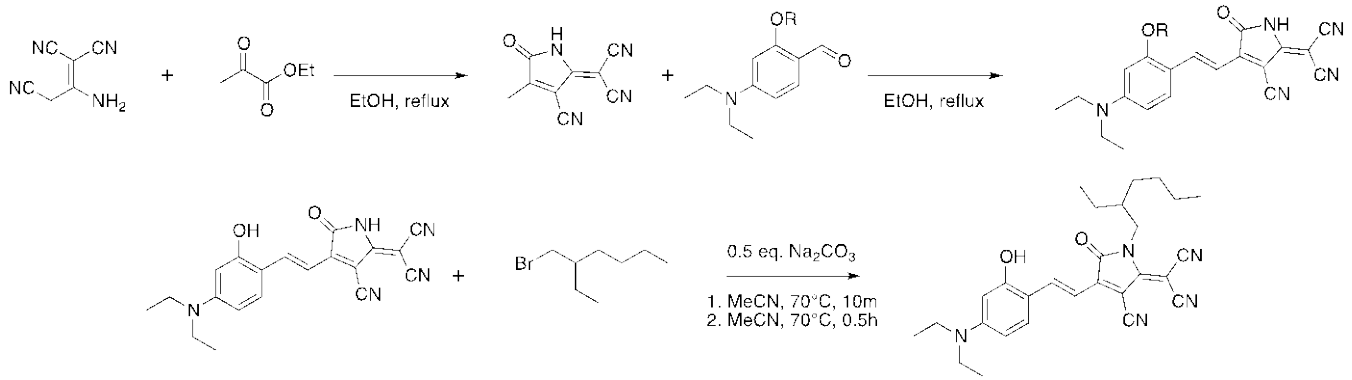

Scheme 2. Syntheses of chromophores

product was filtered and washed with methanol, and isopropanol until the filtrate appeared clear. Product was placed in vacuum oven at 70°C overnight. (0.052g, 7.9% yield)

5e.5b (0.200g, 0.557mmol) and sodium carbonate (0.064g, 0.604mmol) were dissolved in MeCN. The solution was stirred under nitrogen and heated to 70°C for 10 minutes. At the end of 10 minutes, 2-ethylhexyl bromide (0.408g, 2.11mmol) was added and the solution was stirred at 70°C for 30 minutes. Product was vacuum filtered, washed with water and placed in a vacuum oven at 64°Covernight. (0.133g, 43.0% yield).

ethanol or isopropanol. For 5a, 5b and 5e this was sufficient but this was not found to be the case for 5c. The presence of contaminants was most noticeable UV-Vis measurements and during film preparation.

The UV-Vis results of the chromophores in tetrahydrofuran (THF) and N,N-dimethylformamide (DMF) are shownin figure 2 and tabulated in table 1. When moving from THF to the more polar DMF, there was a substantial hypsochromic shift of at least 100nm observed for all chromophores. This suggests that the ground state of these chromophores might exhibit more zwitterionic character and are better stabilized by the more

	THF		DMF		
Compound	λ_{max} (nm)	$Log_{10}\varepsilon$	λ_{max} (nm)	$Log_{10}\varepsilon$	$\Delta\lambda$ (eV)
1	686	4.44	562	4.54	-0.3988
5a	703	4.87	599	4.43	-0.3062
5b	705	4.85	599	4.52	-0.3112
5c	682	3.95	564	—	-0.3804
5e	695	4.19	590	4.49	-0.3175

Results and Discussion

During the synthesis of the chromophores, purification became an ever-increasing problem as the size of the bridge substituents was increased. This was most noticeable for 5c and 5d (data not shown). In a typical procedure, the chromophore was filtered and washed with

polar solvent.[6]

An opposite trend, however, was noticed when films were cast from PMMA. In moving from a 20% solution of THF in dibromomethane, figure 3b shows a slight bathochromic shift on the order of c.a. 10nm. However, this is inconclusive as most of the solutions produced films of poor quality (figure 3a) full of crystallites (figure 4).

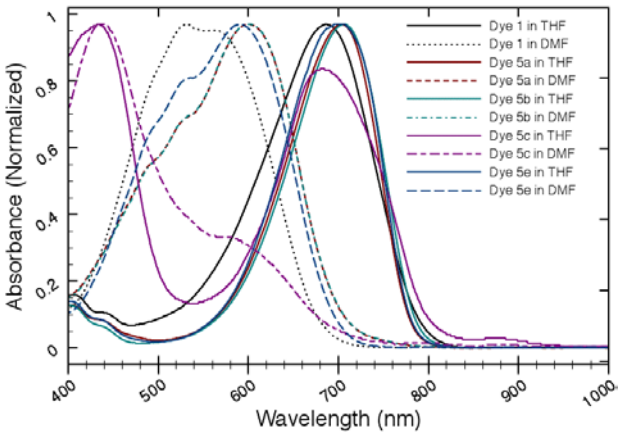

Figure 2.UV-Vis spectra for compounds 1, 5a-c, and 5e in THF and DMF. When moving from the less polar THF to the more polar DMF there was a pronounced hypsochromic shift of ~100nm. This may suggest that the ground state exhibits more zwitterionic character and is, thus, better stabilized in moving from a less polar to more polar solvent.[6]

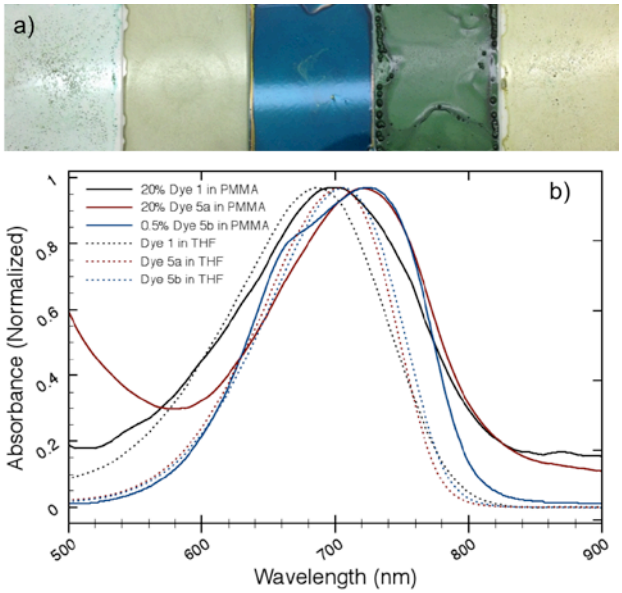

Figure 3. a) Digital images of chromophore films and b) UV-Vis spectra of films in PMMA compared to solutions in THF. A small bathochromic shift was observed for all films with what appears to be a low energy shoulder for films of 1 and a high energy shoulder for films of 5b.

In comparing chromophores**1** and **5a,** which differed by a hydroxyl group on the bridge, both formed films of crystallites within the PMMA film with **1** producing slightly larger crystallites on average.By functionalizing the donor with a plasticizer via the amide, chromophore**5e** produced a near uniform distribution of evensmaller crystallites within the PMMA film (Figure 3c).

Chromophore5b yielded the most successful films. This chromophore was cast in three different ways: from a room temperature solution, from a hot solution, and from a room temperature 0.5% solution (because the first two castings exhibited optical densities greater than 3) (Figure 4). More aggregate formation was observed in the room temperature solution than the hot solution. Chromophore5b also went into solution successfully as evidenced by the homogenous color of the film. The film from chromophore**5c** suggests that this

chromophore is contaminated. Some areas of the film exhibited excellent coating, but there were also many areas where large aggregates were present (Figure 3d)

Conclusions

Addition of substituents to the phenyl ring appears to have some effect on reducing dipole-dipole interactions in the small D-π-A systems. When comparing films of 5b and 5e, having substituents along the bridge appears to have a greater effect in reducing the formation of crystallites leading to more homogenous films.

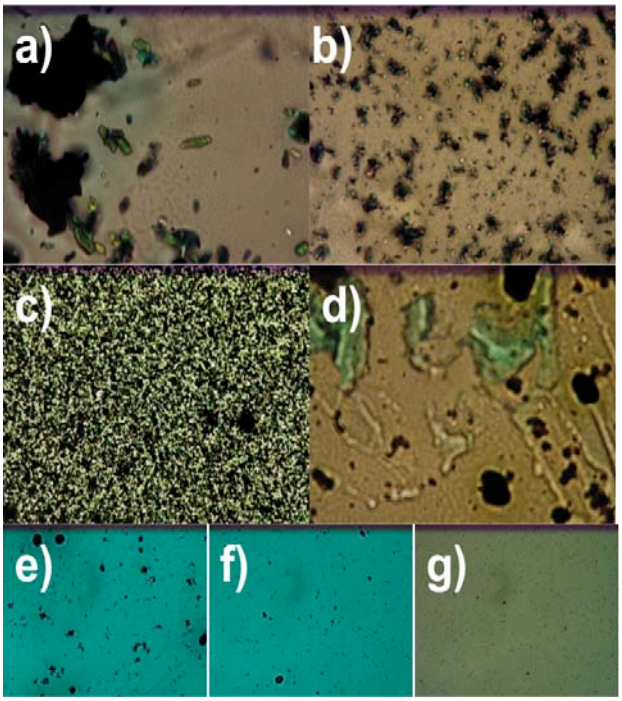

Figure 3.Optical microscope images at 20x of films spun from a) 1, b) 5a, c) 5e, d) 5c and e-g) 5b. Films were cast from 20% THF in dibromomethane.a-f) are for 12% dye in 20% PMMA and g)is 0.5% dye in 20% polymer. e) and g) were cast 25°C solutions and the rest from 90°C solutions.

Future work will involve improvements to the purification process, which became more difficult as the size of the substituents increased, looking at additional groups and positions for bridge substitution and a more in-depth study of
thesolvatochromic shift observed in these small TCP chromophores.

References

1. Cho, M. J.et al. A tricyanopyrroline-based nonlinear optical chromophore bearing a lateral moiety: A novel steric technique for enhancing the electro-optic effect. ScienceDirect 2008;79:193-199.

2. Jang, S. H. et al. Pyrroline Chromophores for Electro-Optics. Chem. Mater. 2006;18:2982-2988.

3. Liu, J. et al. Synthesis and nonlinear optical properties of branched pyrroline chromophores. J. Phys. Org. Chem. 2011;24:439–444.

4. Liu, J. et al. The synthesis and characterizations of NLO-tricyanopyrroline chromophore derivative and the substituent effect on the electro-optical coefficients. J. of Optoelectronics and Advanced Mat. 2009;11:1765 – 1768.

5. Xianqing P. et al. Enhancement of electro-optic activity by introduction of a benzyloxy group to conventional donor-π-acceptor molecules. Organic Electronics. 2011;12:1093–1097

6. Papdopolous, M. G. et al. Non-linear Optical Properties of Matter: From Molecules to Condensed Phases. Dordrecht: Springer, 2006. DOI: 10.1007/1-4020-4850-5

Acknowledgments

The Center on Materials and Devices for Information Technology Research (CMDITR), the NSF Science and Technology Center No. DMR 0120967, Air Force Office of Scientific Research (AFOSR), and the Hooked on Photonics REU program are gratefully acknowledged for enabling this research opportunity. I would also like to thank all the members of the Dalton and Robinson research groups, especially my mentor, Nathan Sylvain, for the excellent guidance in this endeavor.

HANNAH BUEHLER is a senior majoring in chemistry, biology, and math at Luther College in Decorah, IA. After graduation, she will attend either graduate school for chemistry, or medical school.

The Role of Self-exchange Reactions in Ionic Diffusion in Thermocells

IRVIN J. CENTENO, Universidad de Puerto Rico- Mayagüez
Pablo Salazar, Baratunde Cola, Georgia Institute of Technology

Introduction

A thermo-electrochemical cell (or thermocell) uses redox couples as electrolyte and symmetric metal electrodes to generate power from a heat source.

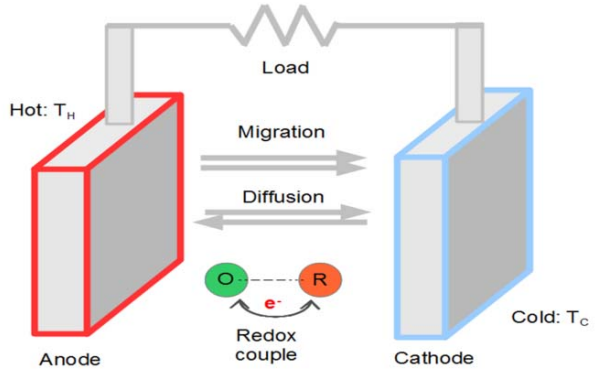

Figure 1. Thermocell Schematic

Voltage is driven by a temperature gradient across the cell.

$$V_{OC} = E_C - E_H = \frac{\Delta S^0_{rx}\,(T_H - T_C)}{nF}$$

Equation 1. Cell voltage equation.

In order for ionic transfer to occur, within a thermocell, one of the following processes should occur; Convection: net velocity of ions and solvent molecules, Thermal diffusion: its driving force is a Thermal gradient, Migration: it's driving for is a Potential gradient, or Diffusion: which is driven by a Concentration gradient.

$$N = -D\nabla C - ZuFC\nabla\emptyset - \frac{Q*}{RT^2}DC\nabla + Cv$$

Equation 2. Mass Transfer-Nernst-Plank model.

Other than diffusion, migration, and convection of ions, electron-transfer processes can also contribute to ionic transfer if the solution contains an oxidation-reduction system.

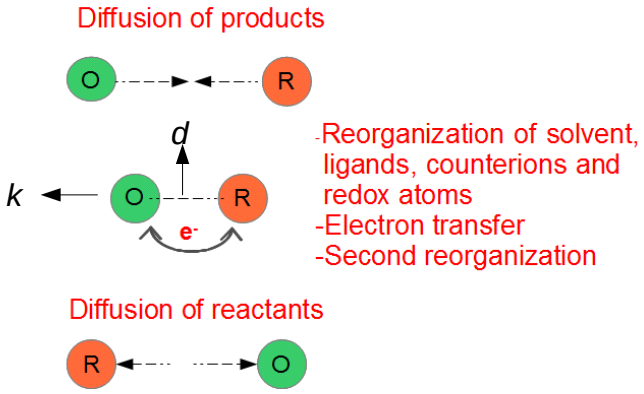

Figure 2. Self-exchange reactions schematic.

Self-exchange reactions take place between redox couples in the bulk electrolyte of thermocells. A self-exchange reaction is a chemical process where an electron moves from one chemical specie to the other, changing the oxidation states of both species. These reactions are usually very fast. The species must diffuse into close proximity for the self-exchange reactions to occur.

When a redox electrolyte is used in a thermocell, diffusion is the process that makes possible the flux of ions in the cell in order to maintain the electric current. This diffusion is enhanced by self-exchange currents, which effectively reduce the distance over which individual ions must diffuse. Using the redox couple ferri/ferrocyanide we strive to understand the balance of electronic (self-exchange) and ionic (diffusion) conduction in a thermocell, and discover ways to enhance current and improve the efficiency of thermocells.

Methods

For self-exchange reactions, we can derive a simple expression to evaluate the effect of exchange redox reactions on the effective diffusivity (eq.3).

$$D_{eff} = D_{int} + kd^2C$$

Equation 3. Effective diffusion equation.

Since Nernst-Einstein equation for mobility (eq.4) is proportional to the diffusion of the ions we replace the mobility in the mass transfer equation (eq.2) for the this equation.

$$u = \frac{DzF}{RT}$$

Equation 4. Nernst-Einstein equation for mobility.

Then we replace the effective diff equation (eq.3) on the mass transfer equation and we get the contribution.

$$\sigma_M - \sigma_A = \sigma_e = \frac{F^2 d^2 k C_R C_O}{RT}$$

Equation 5. Derivation of the conductivity difference model (self-exchange reactions contribution).

Materials

Impedance spectroscopy studies, with three electrodes, and the redox couple ferro/ferricyanide were conducted an interpreted with model available in the literature to help elucidate the contribution of self-exchange reactions to the overall flux of ions in the thermocell.

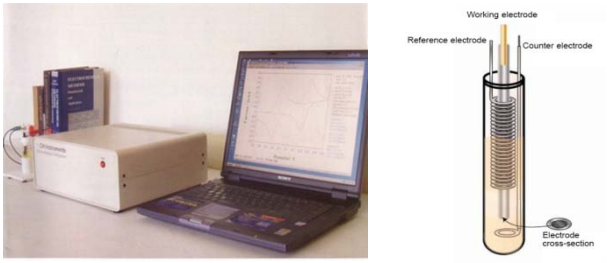

Figure 3. Experimental Setup.

The impedance tests resulted in graphs which represented the equation of two circles. The intersection between the two circles was measured as the ionic resistance. The inverse of these values was then interpreted as the conductance.

Results and Discussion

The studies revealed that the contribution to the generated current attributed to self-exchange or electronic conduction is significant compared to contribution attributed to ionic conduction (diffusion).

Conductance (uS/m)			
C (mol/m³)	σ_A	σ_M	$\sigma_M - \sigma_A = \sigma_e$
10	1.38	1.30	-0.08
20	1.65	1.37	-0.28
100	2.53	2.24	-0.29
200	3.30	3.30	0.00
400	3.75	4.49	0.73

Table 1. Experimental conductance difference values.

If we were to use the model to find the values of conductance, using k=$1.9x10^4$ $M^{-1}s^{-1}$ and$d = 7 - 8$ A, the order of magnitude for the experimental conductivity differences at high concentrations are in the same range as in the theoretical model. At a lower concentration there seems to be an offset in the values, which can be attributed to possible reactions occurring at these concentrations.

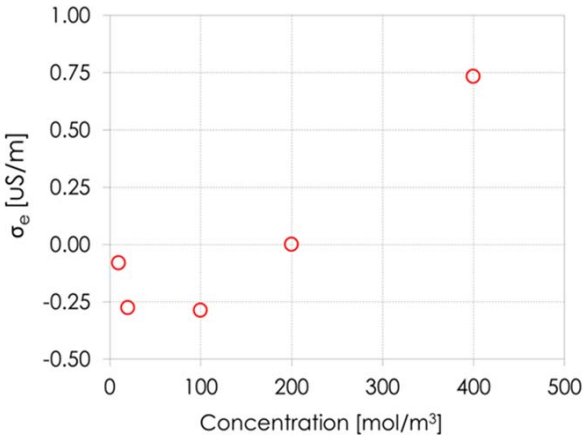

Graph 1. Concentration vs. conductance difference.

The results also suggest that catalytic dispersants such as carbon nanotubes (CNTs) could be used to mediate self-exchange reactions and enhance the effective ionic diffusion in thermocells.

Conclusions

Adding carbon nanotubes to the electrolyte mixture could be used to mediate self-exchange reactions and enhance the effective ionic diffusion in thermocells.

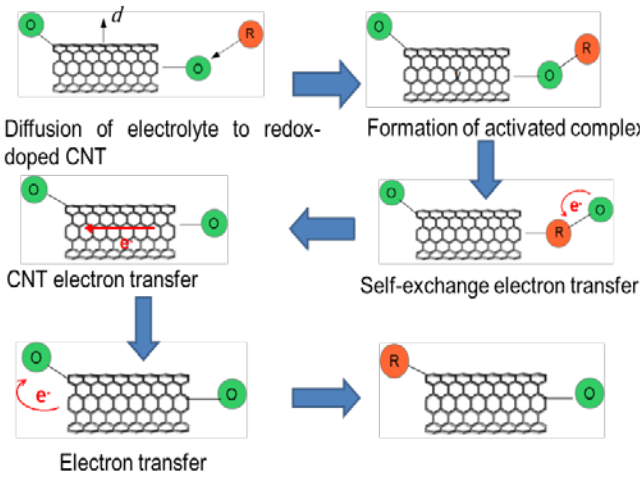

Figure 5. Redox mechanism in redox-doped CNT.

By adding CNT we look to increase the effective electron transfer distance in self-exchange reactions.

References

1. "Electronic conduction in aqueous solution" by Harald Dahms (1987)
2. "Application of Diffusion Constant Measurement to the determination of the Rate Constant of Electron-Exchange Reactions" by I. Ruff (1970)
3. "Harvesting Waste Thermal Energy Using a Carbon-Nanotube-Based Thermo Electrochemical Cell" by Renchong Hu, and Baratunde A. Cola (2010)

Acknowledgements

Funds for this research were provided by the Center on Materials and Devices for Information Technology Research (CMDITR), and the NSF Science and Technology Center No. DMR 0120967.

Irvin J. Centeno is a rising sophomore in Mechanical Engineering in the University of Puerto Rco-Mayaguez. After completing his undergraduate studies he plans to enroll in graduate school and pursue his MD/Ph.D.

Synthesis and Characterization of Externally Initiated P3HT

HOI K. (CHRISTY) CHEUNG, Edmonds Community College
Dr. Prakash Sista, Dr.Christine Luscombe, University of Washington

Introduction

Poly(3-hexylthiophene) (P3HT) is a conventional π-conjugated polymer used in optoelectrical devices. A regioregular P3HT has a better charge mobility because polymer chains can pack closely to each other.1 In the past decades, there were many innovations in synthesizing regioregular P3HT. The luscombe group had also developed an externally initiated polymerization method to synthesize regioregular P3HT with controlled molecular weights and narrow polydispersity.2 A chain growth polymerization, as the name has mentioned, can form a chain by adding monomers onto the catalyst. The aromatic part of the catalyst serves as the initiator of the chain, while the other half of catalyst attaches on to the termination of the chain. When the polymerization is quenched with acid, the proton replaces Ni(dppp)Cl and attach as the end group of the polymer (Figure 1). In this way, every polymer chain will have an uniform hydrogen end group. External initiated polymerization can also control the length of the polymer chain, which depends on the ratio of the catalyst to the monomers.3

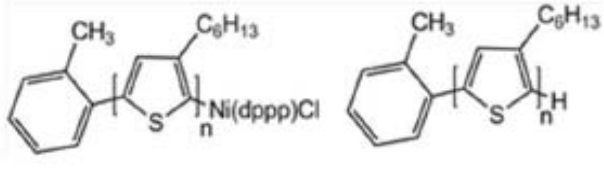

Figure 1. The structure on the left shows the end group of the polymer chain, before quenching the reaction, as Ni(dppp)CL, while the one on the right shows hydrogen as end group after quenching with acid.

The objective of this project is to synthesize and characterize externally initated P3HT at high regioregularity with the catalyst cis-chloro(tolyl)(dppp)nickel(II) complex (figure 2).

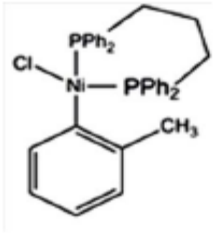

Figure 2. Structure and catalyst

Both regioregular P3HT and regioirregular P3HT are shown in figure 3. A head-to-tail polymer chain is regioregular, while a head-to-head and a tail-to-tail coupling decrease regioregularity.4

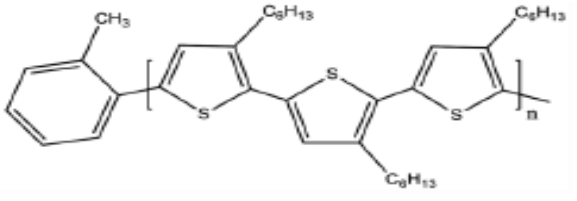

Figure 3a: Regioregular P3HT

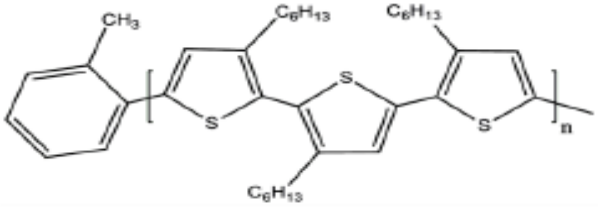

Figure 3b: Regioirregular P3HT

Grignard reaction plays an important role in controlling regularity. When grignard reagent is added to 2-bromo-3-hexyl-5-iodothiophene, both 5-chloromagnesio-2-bromo-3-hexylthiophene and 2-chloromagnesio-3-hexyl-5-iodothiophene (figure 4) are formed. In order to aim high regioregularity, the percentage of 5-chloromagnesio-2-bromo-3-hexylthiophene has to be much higher. This can be achieved by lowering the temperature of the mixture to 0 ºC when the Grignard reagent is added. After P3HT is made, its molecular weights, polydispersity index, regioregularity, and end group are obtained by Gel Permeation Chromatography (GPC), 1H Nuclear Magnetic Resonance (NMR), and Matrix-Assisted Laser Desorption/Ionization (MALDI).

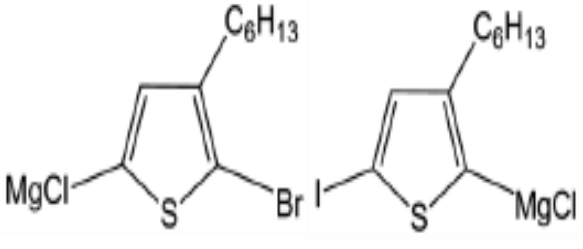

Figure 4: 5-chloromagnesio-2-bromo-3-hexylthiophene (left) and 2-chloromagnesio-3-hexyl-5-iodothiophene (right)

Experimental Methods

The experiment was divided into four steps. First, the monomer, 2-bromo-3-hexyl-5-iodothiophene was prepared from 2-bromo-3-hexylthiophene. Second, the, catalyst, cischloro(tolyl)-(dppp)nickel(II) complexes, was prepared. Third, poly(3-hexylthiophene) was synthesized with the prepared monomer and catalyst. The last step was characterizing the polymer.

(1)Preparation of 2-bromo-3-hexyl-5-iodothiophene[3]

2-bromo-3-hexylthiophene (1.27g, 20.2 mmol) was stirred in dichloromethane at 0 ºC and then mixed with iodine (0.579g, 11.2 mmol) and iodobenzene diacetate (0.788g, 12.2 mmol). The mixture was stirred for 4 hours at room temperature. 10% sodium thiosulfate (50 mL) was added to react with the residual iodine. After extraction with ether, the organic layer was dried over anhydrous magnesium sulfate and filtered. The residual dichloromethane and iodobenzene were removed by the rotavapor. 2-bromo-3-hexyl-5-iodothiophene was further purified using column chromatography (with hexane as the eluent) and vacuum distillation. The monomer was analyzed with NMR to confirm iodine attached on 5' position of the ring. 1H-NMR (CDCl3, ppm) δ: 6.99(s, 1H), 2.55(t, 2H), 1.57(m, 2H), 1.33(m, 6H), 0.92(m, 3H).

(2)Preparation of cis-chloro(tolyl)(dppp)nickel(II) complexes[2]

The following steps were performed in glove box. Tetrakis(triphenyl-phosphine)nickel(0) (66.6 mg, 0.0602 mmol) was mixed with o-chlorotoluene (4 mL) and stirred overnight. The solution was checked with 31P NMR to make sure the starting materials had bound together. 1,3-Bis(diphenylphosphino)propane (37.3 mg, 0.0903 mmol) was then added to perform ligand exchange. The mixture was further stirred for 3 hours. 31P-NMR (CDCl3, ppm) δ: 21.3, -5.4ppm.

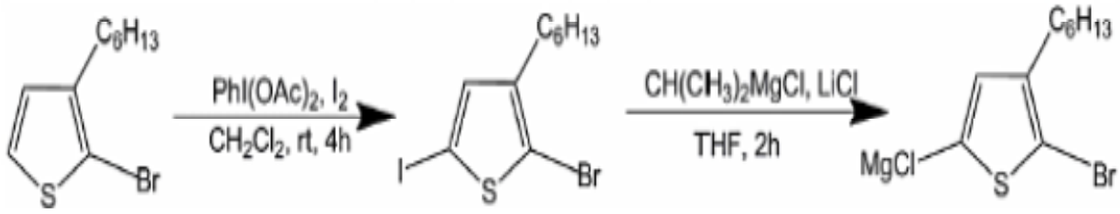

Scheme 1: Synthesis route of 2-Bromo-3-Hexyle-5-iodothiophene

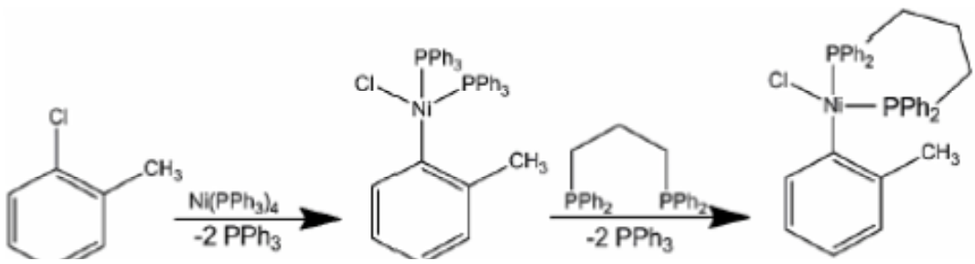

Scheme 2: Preparation of catalyst, cis-chloro(totyl)(dppp)nickel(II0 complexes

Scheme 3: Synthesis route of poly(3-hexylthiophene)

(3) Synthesis of poly(3-hexylthiophene)[2]

The synthesis was air-free. 2-bromo-3-hexyl-5-iodothiophene (0.674 g, 1.807 mmol) and lithium chloride (0.0766 g, 1.807 mmol) was mixed in tetrahydrofuran (18.07 mL) at 0 ºC. Isopropy magnesium chloride (0.271 mL, 2 M) was added through a syringe, and then the ice bath was removed to bring the mixture up to room temperature. After stirring for 2 hours, all the catalyst, cis- chloro(tolyl)(dppp)nickel(II) complex, was transferred rapidly from the schlenk flask into

the reaction flask. The mixture turned into deep red color in a short period of time. After an hour of stirring, the polymerization was quenched with a mixture of methanol and hydrochloric acid. The resulting crude polymer was filtered out using a fritted funnel. After washing the crude polymer with hexane and dried, the polymer was characterized using GPC, 1H-NMR, and MALDI. 1H-NMR (CDCl3, ppm) δ: 6.98(s, 1H), 2.80(t, 2H), 2.49(s, 3H), 1.55(m, 8H), 0.91(s, 3H).

(4) Characterization of P3HT

A small amount of P3HT was dissolved in THF to prepare the GPC sample. NMR sample was prepared by dissolving 2 mg of P3HT in 1 mL of d-chloroform. For MALDI, 5 mg of P3HT was dissolved in 1 mL of chloroform so that the concentration was high enough. For the samples prepared with high molecular weight P3HT, heat was applied to improve solubility.

Results and Discussion

P3HT was characterized by GPC, NMR, and MALDI.

Table 1: Molecular Weight and Polydispersity index obtained by GPC				
Polymer	1	2	3	4
Molecular Weight (kDa)	28.3	24.1	8.78	3.5
Polydispersity index (PDI)	1.18	1.43	1.25	1.34

From the GPC data, it is shown that polymer 1 has much lower PDI than the other three. This is related to how fast the catalyst is added to the monomer during synthesis. If the catalyst is transferred to the monomer through cannula, the force may not be strong enough to transfer all at once. In this way, some catalyst starts reacting with monomer, while other hasn't. Polymer chains result in having inconsistent molecular weight, which leads to high PDI. If the catalyst is added through syringe, all catalyst is transferred one time. This results in small PDI.

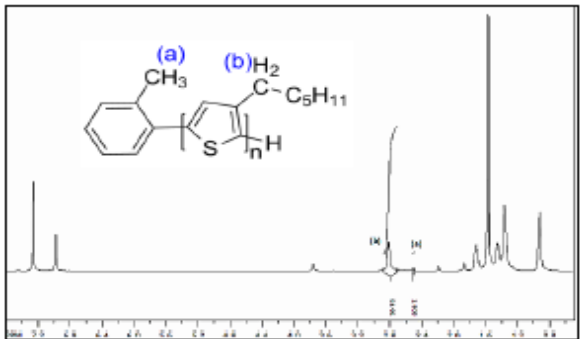

Figure 5: 1H NMR Spectrum of P3HT with 8kDa is shown. The number of repeating units can be calculated through the integration at 2.8 ppm

NMR integrates the area under the peak and shows the ratio of proton attaches to the carbon. However, the number of repeating units and the molecular weight of P3HT are not shown. Thus, in order to get these numbers, the CH3 on tolyl group (a) were integrated against the CH2 protons on the hexyl chain (b) of the polymer(figure 5).

Table 2: Repeating Units, molecular weights calculated through NMR integration				
Polymer	1	2	3	4
Integration at 2.4 ppm	1			
Integration at 2.8 ppm	102.1	92	34	12.4
# of repeating units	153	138	51	19
Molecular weight(kDa)	25.5	23.0	8.56	3.25

Table 2 lists the integration of the peak at 2.4 ppm, which indicates the proton of CH3 on the tolyl group, and the integration of the peak at 2.8 ppm, which indicates the proton of CH2 proton on the hexyl chain. For example, the ratio of the integration at 2.4 ppm and 2.8 ppm of polymer 3 is 1:34. By adjusting the ratio from 1:34 to 3:102, it is shown that there are actually 102 CH2 protons in one chain. Thus, there are 51 repeating units. As one repeating unit is 166 Da, molecular weight of the P3HT chain is 8.56 kDa.

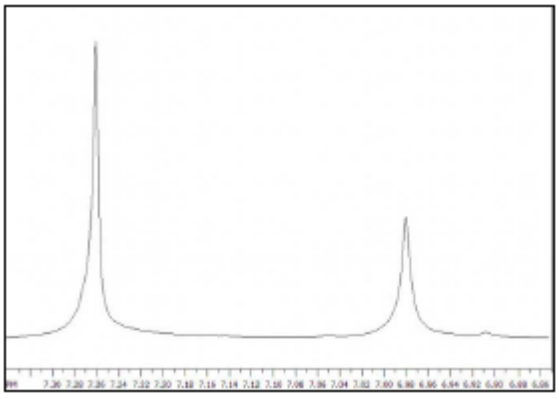

Figure 6 shows a close-up of the peak of 6.98ppm. The smooth curve indicates the formation of regioregular P3HT.

The regioregularity of P3HT can also be observed through NMR spectrum. Figure 6 shows the polymer 2 has regioregularity close to 100% because there is no other small peak around 6.98 ppm except the peak of chloroform-d at 7.26 ppm and the coupling between 13C and 1H at 6.91 and 7.05 ppm. The other spectra of P3HTs also reports high regioregularity.

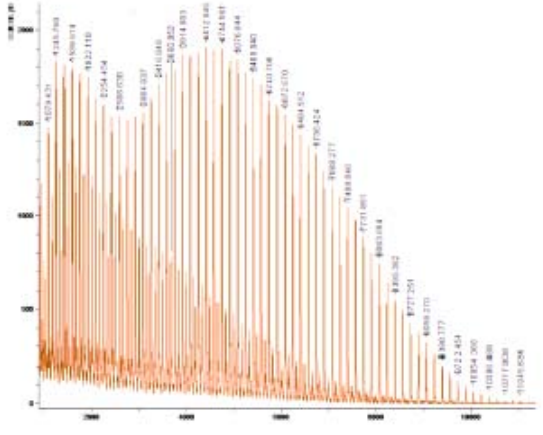

Figure 7: MALDI Spectrum of P3HT with 8kDa is shown. The difference between the two consecutive mass-to-charge ratios (m/z) is 166. This confirms the end group of the polymer as hydrogen because the repeating unit of polymer chain has the molecular weight of 166.

MALDI spectrum of P3HT with 8 kDa is shown in figure 7. By getting the difference between two consecutive mass-to-charge ratio, the molecular weight of one repeating unit is obtained, and hence the end group of the polymer chain is determined. For P3HT with hydrogen as the end group, the difference is 166. However, if the end group is bromine, the difference will be 245.

Conclusions

Four P3HT with different molecular weights were synthesized, using cis-chloro(tolyl)(dppp)nickel(II) as the catalyst. GPC shows that the four polymers have the molecular weights as 28.3, 24.1, 8.78, and 3.50 kDa. The PDIs of the three polymers are 1.18, 1.43, 1.25, and 1.34 respectively. NMR integration calculates the molecular weights as 25.5, 23.0, 8.56, and 3.25kDa, which agrees with GPC data. NMR also shows all three polymers have regioregularity close to 100%. MALDI spectrum confirms the end group of P3HT as hydrogen.

Acknowledgments

I would like to thank the Center on Materials and Devices for Information Technology Research (CMDITR), and the NSF Science and Technology Center No. DMR0120967 for funding the research. I would also like to thank Dr. Christine Luscombe for giving me the opportunity to work on this project, Dr. Prakash Sista for guiding me along the research, Dr. Ken Okamoto for helping us gain access to instruments, and Dr. Ming Jian Yuan for giving suggestion for improvement.

References

1. Mauer, R.; Kastler, M.; Laquai, F. *Adv. Funct. Mater.* 2010, *20*, 2085.
2. Bronstein, H. A.; Luscombe, C. K. *J. Am. Chem. Soc*. 2009, *131,* 12894.
3. Yokoyama, A.; Miyakoshi, R.; Yokozawa, T. *Macromolecules* 2004, *37*, 1169.
4. Peng, Q. M.S. Thesis, Queen's University, ON, March 2010.

Christy Cheung is a transferring student from Edmonds Community College. She will continue her undergraduate study in Biochemistry at the University of Washington. Her goal is to become a surgeon.

Optimization of Stacked Inverted Top-Emitting Organic Light-Emitting Diodes

KENDALL DAVIS, Xavier University of Louisiana
Keith Knauer, Ehsan Najafabadi, and Bernard Kippelen, Georgia Institute of Technology

Introduction

Organic light-emitting diodes (OLEDs) are light sources that use a thin film of organic materials as the light-emitting component. OLEDs are very thin (with a total thickness on the order of hundreds of nanometers), bright (upwards of 10,000 cd/m^2), and have a wide viewing angle. They can also be deposited on flexible substrates, making them promising for future use in display technologies.

An OLED in the conventional architecture is displayed in Fig. 1. These OLEDs are formed from an electroluminescent organic thin film used as an emissive layer located between a bottom anode and a top cathode all on top of a substrate. Other layers, such as charge-transport and injection layers, are used to improve charge transport into the emissive layer. In order for electrons to be injected easily between materials, the lowest unoccupied molecular orbital (LUMO) levels of the materials need to roughly align (have the same energy). For hole transportation, it is the highest occupied molecular orbital (HOMO) levels that need to align. In this way, injection and transport layers are useful in acting as an energy step ladder for easier charge injection. Once charges have been transported into the emissive layer, they combine to form an exciton, which can then decay to produce a photon.

Most OLEDs are bottom-emitting, such that the emitted photons exit from the bottom through a transparent contact such as indium tin oxide. However, OLEDs can also be top-emitting such that the light is emitted through a semi-transparent top electrode.

In an inverted OLED, the positions of the electrodes are switched, with the anode on top and the cathode on bottom. The inverted OLED architecture is more conveniently

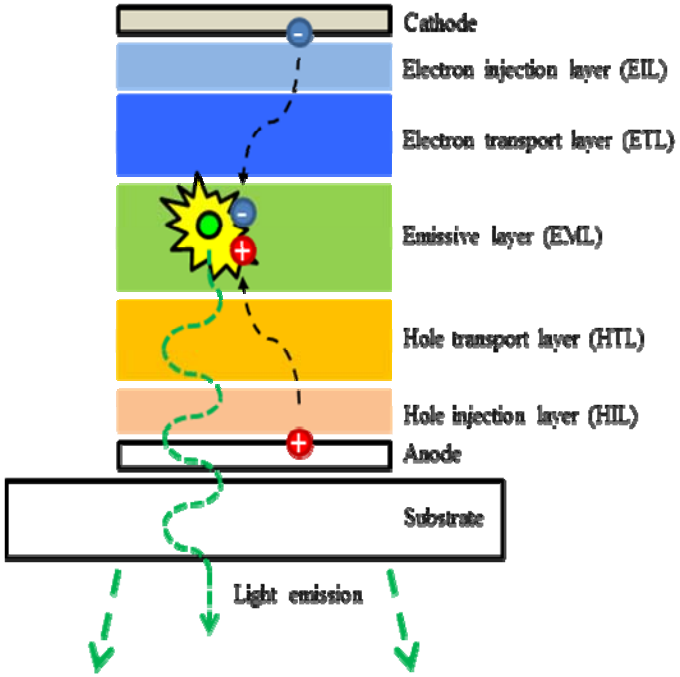

Figure 1 Diagram of a conventional OLED, Image by Farhan Kamili

incorporated into active-matrix displays[1] which use superior n-type driving technology. An active-matrix cross-section is shown in Fig. 2 with a bottom-emitting and a top-emitting OLED. Top-emitting OLEDs provide several advantages.

First they can be deposited on opaque substrates, such as their driving circuitry, allowing the pixel aperture ratio to be maximized. This allows for higher total display brightness at a lower driving current, increasing the lifetime of the devices. Also, they do not require an inflexible, brittle indium tin oxide contact allowing for displays and lighting panels with flexible form factors.

Objectives

Despite their advantages, comparatively little investigation into inverted top-emitting OLEDs has been conducted, and in what literature is available on the topic, inverted top-emitting OLEDs show

inferior performance in comparison to many conventional OLEDs. Here, inverted top-emitting OLEDs are investigated in order to improve their performance in the areas of efficiency (external, power, and current) and lifetime. Specifically, attempts to fabricate a stacked top-emitting inverted OLED have been conducted.

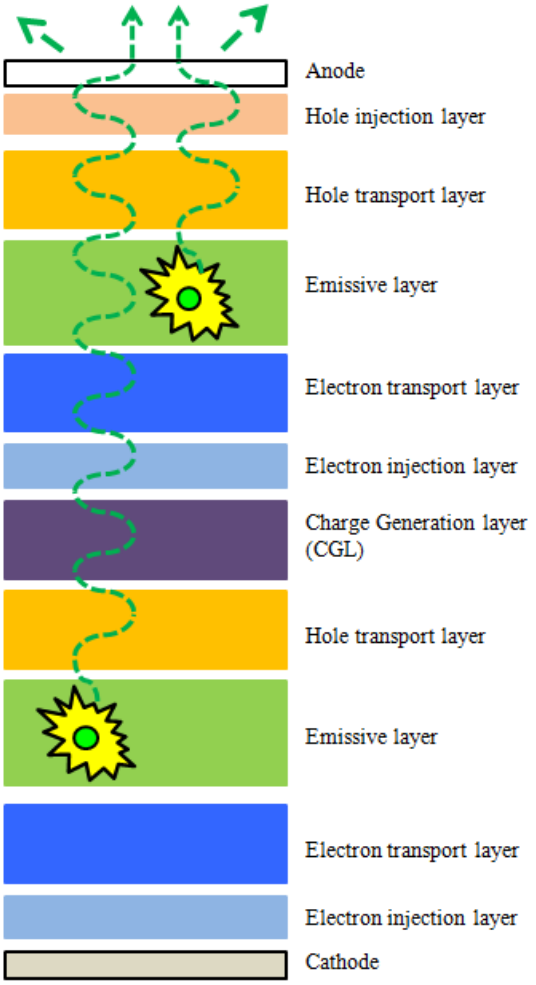

Figure 2. Diagram of a stacked inverted top-emitting OLED

Stacked (or tandem) OLEDs are devices in which a series of emissive layers are stacked on top of one another with a charge generating layer in between. This allows more light to be produced at lower current densities, resulting in longer lifetimes and possibly improved power efficiency. At present, there are no reports of stacked top-emitting inverted OLEDs, so this research focused on producing and optimizing an efficient device of this architecture. A structure of a stacked inverted top-emitting OLED is displayed in Figure 3.

Experimental Methods

The OLEDs under study were developed through vacuum thermal evaporation (EvoVac, Armstrong Engineering Inc). The substrates were 1 in × 1 in glass squares cut from 3 in × 1 in microslides (VWR international). The substrates were cleaned in detergent water, distilled water, acetone, and isopropanol by ultrasonication for 20 min each and blown dry with nitrogen gas. The substrates were then treated by exposure to oxygen plasma for 2 min before being spincoated with polyethylene dioxythiophene-polystyrene sulfonate (PEDOT:PSS, Clevios P VP AI 4083). The PEDOT:PSS was dispensed through a 0.45 µm polyvinylidine fluoride filter and spincoated for 1 min at 5,000 rpm. The substrates were then heated to 140 °C to cross-link the PEDOT:PSS. Further handling of the substrates took place in a nitrogen-filled glovebox (O_2 <0.1 ppm, H_2O < 3.0 ppm). The substrates were then loaded into the EvoVac for the thermal deposition of the metal and organic layers at less than 3 x 10^{-7} torr and at a rate of 1-2 Å/s. Layer thickness is controlled during evaporation and can be checked using spectroscopic ellipsometry. After deposition, the OLEDs were characterized using a sourcemeter (Keithley 2400), calibrated photodiode (FDS 100 from Thorlabs, Inc.), and spectrometer (Ocean Optics USB4000).

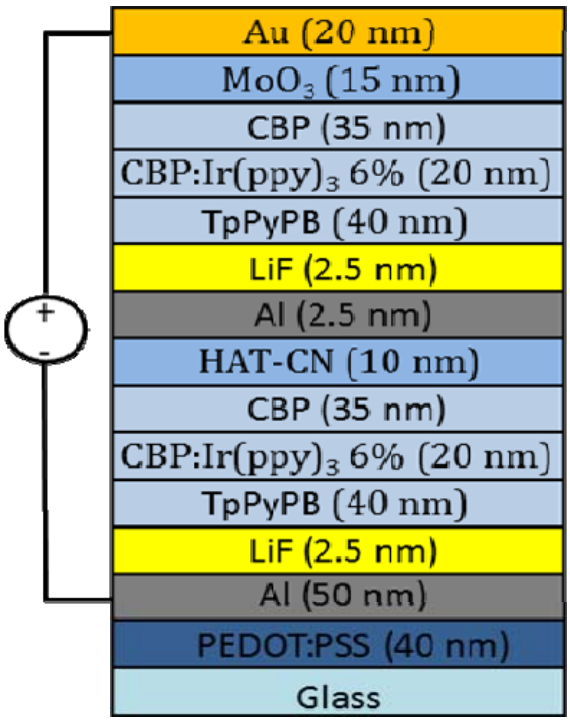

Figure 3. Detailed structure of a stacked inverted top-emitting OLED

Results

Figure 3 displays the structure of a stacked OLED. This structure was based on a previous inverted top-emitting device structure[2] that was modified to become a stacked OLED with 1,4,5,8,9,11-hexaazatriphenylenehexacarbonitrile (HAT-CN), as the charge-generation layer (CGL). Aluminum(Al)/lithium fluoride(LiF) was used as a bilayer cathode, 1,3,5-tri(p-pyrid-3-yl-phenyl)benzene(TpPyPB) was used as an electron-transport layer, 4,4'-bis(N-carbazolyl)-1,1'-biphenyl (CBP) doped with 6 vol.% tris(2-phenylpyridine)iridium(III)Ir(ppy)$_3$ as an emissive layer, CBP as a hole-transport layer (HTL), HAT-CN as CGL, molybdenum trioxide (MoO_3) as a hole-injection layer, and gold (Au) as an anode. The results of this experiment are shown in Figs. 4 and 5.

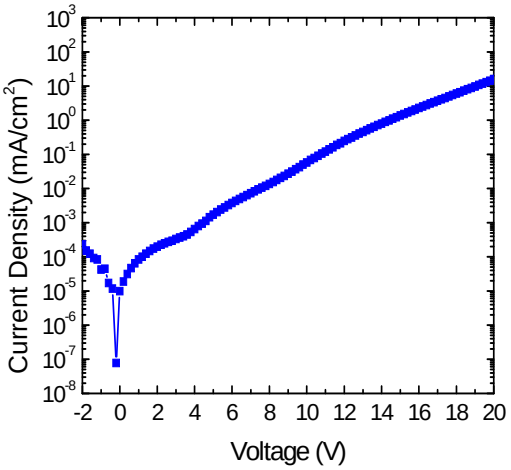

Figure 4. Current density versus voltage of stacked devices with CBP as the HTL.

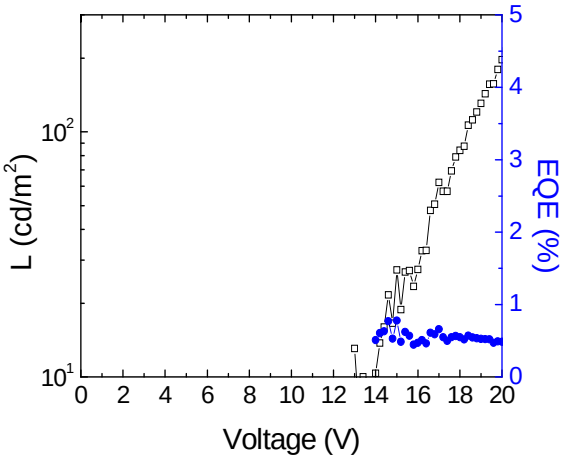

Figure 5. Luminance and external quantum efficiency versus voltage of stacked devices with CBP as the HTL.

In the following experiment the HTL was switched from CBP to N,N'-Di-[(1-naphthyl)-N,N'-diphenyl]-(1,10-biphenyl)-4,40-diamine (α–NPD). The thickness of the aluminum interlayer was also varied, with some devices having an Al interlayer thickness of 2.5 nm and others having an Al interlayer thickness of 1 nm. The results of both cases are shown in Figs. 6 and 7. The current efficacy at 1,000 cd/m^2 was 27.8 cd/A for the 2.5 nm Al interlayer devices, and 16.1 cd/A for the 1.0 nm Al devices.

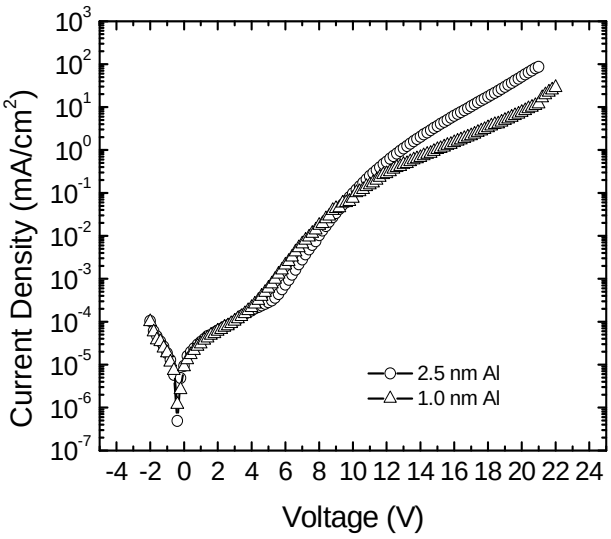

Figure 6. Current density versus voltage of devices with α-NPD HTL

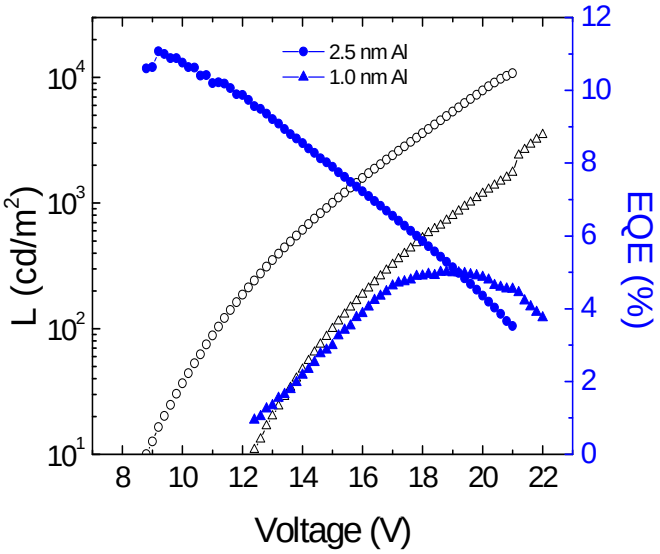

Keeping the 2.5 nm thick Al interlayer, we next varied the thickness of the LiF interlayer. The LiF thicknesses used were 0.5 nm, 1.0 nm, and 2.5 nm

thick. Also, devices with no LiF in the interlayer were fabricated. The current efficacy at 1,000 cd/m^2 was 31.3 cd/A for the 0.5 nm LiF interlayer devices, 38.0 cd/A for the 1.0 nm devices, and 32.2 cd/A for the devices with no LiF in the interlayer.

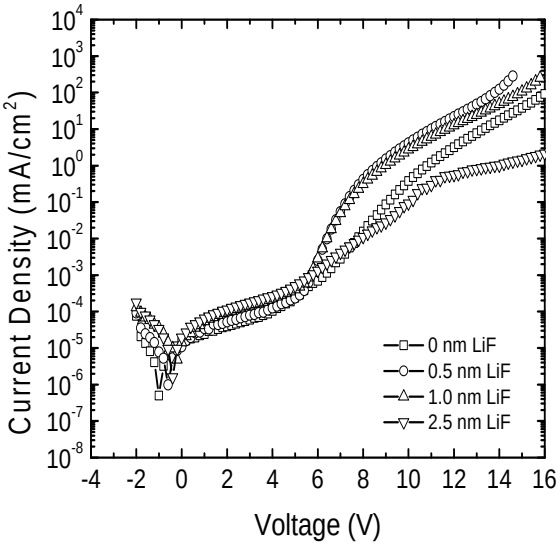

Figure 8. Current density versus voltage of LiF interlayer variation devices

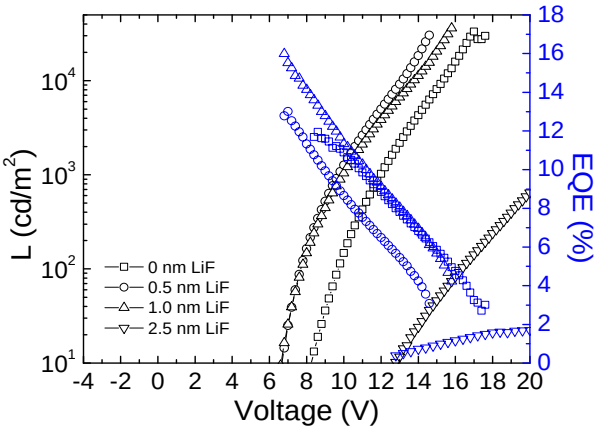

Figure 9. Luminance and EQE versus voltage of LiF interlayer variation devices

Discussion and Conclusions

The change from a CBP HTL to an α-NPD HTL dramatically increased the performance of the devices. A notable improvement can be noticed in luminance, external quantum efficiency (EQE), turn-on voltage (defined as the voltage at a luminance of 10 cd/m^2) and current efficacy for both the 2.5 nm and 1.0 nm Al interlayer devices. This enhancement can be explained by the energy level alignment between the charge generation layer (HAT-CN) and the hole-transportation layer[3]. This is shown in Fig. 10. The energy gap between the LUMO level of HAT-CN and the HOMO level of α-NPD is smaller than the gap between the LUMO levels of HAT-CN and CBP. Decreasing the size of this gap likely increases the quantity of charges generated at the CGL-HTL junction. It is also clear the 2.5 nm Al interlayer outperformed the 1.0 nm Al devices.

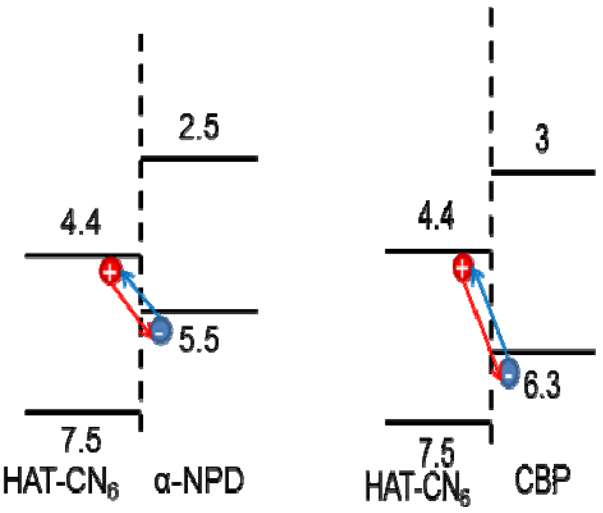

Figure 10. Energy level alignment of the CGL-HTL junctions

In our third experiment the performance of the devices were further improved. Devices with 1.0 nm of LiF in the interlayer showed the best performance, showing a moderate improvement over previous devices. It is probable that at 2.5 nm of LiF, the LiF layer became too insulating, preventing efficient charge transportation. Conversely, removing the LiF interlayer also seemed to decrease performance, pointing towards the importance of the reaction at the Al/LiF junction and suggesting that the ideal thickness is somewhere between 0 nm to 2.5 nm.

A double stacked device should ideally have double the current efficacy of a single OLED of the same architecture. In previous experiments conducted in lab, with top-emitting inverted OLEDs in which α-NPD was used as a HTL in single devices, the resulting current efficacy at 1,000 cd/m^2 was 33.7 cd/A . The current efficacy obtained from our best devices at the same luminance was 38.0 cd/A, which falls short of the ideal result. However, progress has been made in demonstrating an efficient inverted stacked OLED.

References

1. J.-S. Yoo, S.-H. Jung, Y.-C. Kim, S.-C. Byun, J.-M. Kim, N.-B. Choi, S.-Y. Yoon, C.-D. Kim, Y.-K. Hwang, and I.-J. Chung, “Highly Flexible AM-OLED Display With Integrated Gate Driver Using Amorphous Silicon TFT on Ultrathin Metal Foil,” J. Disp. Tech. **6**, 565–570 (2010)

2. E. Najafabadi, K. A. Knauer, W. Haske, C. Fuentes-Hernandez, B. Kippelen, “Highly efficient inverted top-emitting green phosphorescent organic lightemitting diodes on glass and flexible substrates” Appl. Phys. Lett. 101, 023304 (2012); doi: 10.1063/1.4736573

3. T. Chiba, Y. Pu, R. Miyazaki, K Nakayama, H Sasabe, J Kido, “Ultra-high efficiency by multiple emission from stacked organic light-emitting devices” Organic Electronics 12 (2011) 710–715

Acknowledgments

Funds for this research were provided by the Center on Materials and Devices for Information Technology Research (CMDITR), and the NSF Science and Technology Center No. DMR 0120967

KENDALL DAVIS is a junior at Xavier University of Louisiana, where he is a dual Physics and Electrical Engineering major.

Characterizing and Controlling the Polarization of an OP-VECSEL

KATHERINE WILLIAMS-DUHAMEL,University of Massachusetts Amherst
Chris Hessenius, Michal Lukowski, Dr. Mahmoud Fallahi, University of Arizona

Introduction

The purpose of this research project was to build upon the recent discovery that the light emitted by an optically-pumped vertical external cavity surface emitting laser (OP-VECSEL) is linearly polarized. The OP-VECSEL is a type of surface-emitting laser, meaning the radiation beam propagates through the surface normal of the semiconductor chip as oppose to along the edge of the chip. An OP-VECSEL consists of a semiconductor quantum well gain region, a Distributed Bragg Reflector (DBR) used as one mirror, an external cavity mirror and another semiconductor laser as the pump source. The VESCEL differs from the VCSEL (vertical-cavity surface-emitting laser) in that one of the DBR mirrors of the optical resonator is removed and replaced with a curved external cavity mirror. Also, the VCSEL is electrically pumped. A schematic diagram of the OP-VECSEL is shown below in Figure. 1.

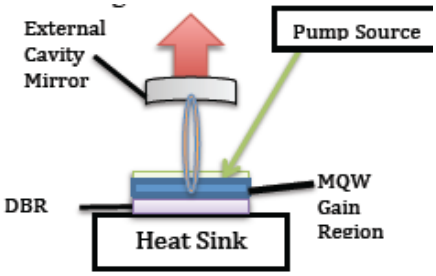

Figure 1. A schematic diagram of the OPS-VECSEL.

A picture of the actual OP-VECSEL setup is shown in Figure. 2.

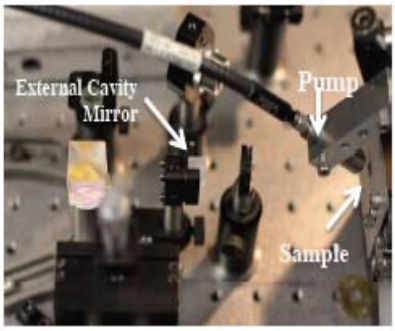

Figure 2. The experimental set-up of the OP-VECSEL.

In comparison, a diagram of the VCSEL cavity is shown in Figure. 3.

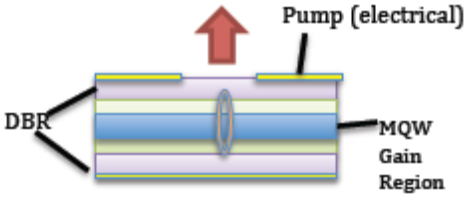

Figure 3. A schematic diagram of the VCSEL cavity.

The gain region consists of multiple quantum wells made of semiconductor material that determines the operating wavelength. The layer structure of the VECSEL chip can be seen in Figure. 4.

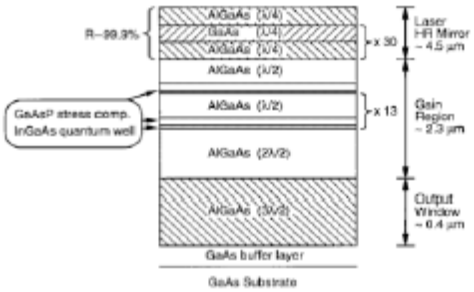

Figure 4. The structure of the semiconductor MQW VECSEL chip.

The sample used for this project was designed to operate around λ~ 980 nm. The OP-VECSEL is unique in that the laser beam, through pumping and cavity design, can be made circular and near-diffraction limited while also being capable of producing high output power1. Edge-emitting semiconductor lasers emit an elliptically shaped beam, which diverges faster and is harder to control than the Gaussian beam (TEM00) of the surface-emitting lasers. The external cavity mirror means the size of the pump spot can be controlled which allows for power scaling. Also, it allows for access to high power intra-cavity radiation to generate new

wavelengths and narrow line widths. The applications of OP-VECSELs include optical fiberand free-space communications, optical storage, etc.

It is often advantageous to have high power, high brightness linearly polarized laser output. Furthermore, there are many situations where control over linearly polarized light is key. It is particularly important in OP-VECSELs to be able to control the polarization because although the laser beam is linearly polarized, the polarization is not locked in (can be S- or P- polarized depending on many factors). For this research project, I demonstrated a method of switching the polarization, and thus locking it, using a curved mirror to reflect the polarized light back into the laser cavity through the external mirror. Two different cavity set-ups were used to switch the polarization of the laser output. The second one was used to minimalize the power losses.

Experimental Methods

The research was carried out using an OP-VECSEL operating at λ~ 980 nm, the Optical Spectrum Analyzer (OSA), a power meter, a current driver and the CCD (camera). A 45 W diode laser pump was the power source for the VECSEL and the VECSEL chip was cooled to 15°C during every experiment. The pump spot size was 250 microns and a 10 cm ROC 94% OC was used. The cavity length corresponding to the given pump size and output mirror was calculated to be 9 cm using Matlab and mode-matching equations (see Eq. 1, Eq. 2, and Eq. 3).

$$w(z) = w_o\sqrt{1+(\frac{z}{z_R})^2}$$

spect to the distance along the axis of propagation (z-axis).

$$z_R = \frac{\pi w_o^{\,2}}{\lambda}$$

wavelength and beam waist.

$$R(z) = z[1+(\frac{z_R}{z})^2]$$

Equation 3. The radius of the beam with respect to the Rayleigh range and the distance along the z-axis.

The first step was to take the free lasing spectra and corresponding output powers of the sample starting at the lasing threshold, determined to be 3.9 W, and then at a net pump power of 4.9 W, 6.2 W, 7.4 W, 8.6 W, and 9.9 W. All of the spectra are taken using the OSA and the powers are measured using the power meter. The next step was to use a polarizing beam splitter to separate the light into S-polarized and P-polarized and determine the polarization of the laser light (See Figure. 5 and Figure. 6). The beam splitter was placed 6.5 cm away from the output mirror and the lasing spectra and corresponding powers were taken for both the P-polarized and Spolarized light at the same currents as before.

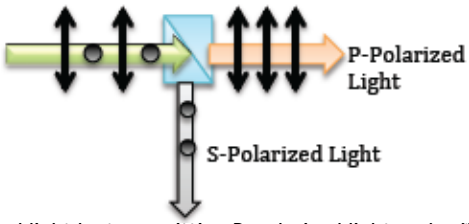

Figure nearly polarized light by transmitting P-polarized light and reflecting S-polarized light. The dots represent S-polarized light and the arrows represent P-polarized.

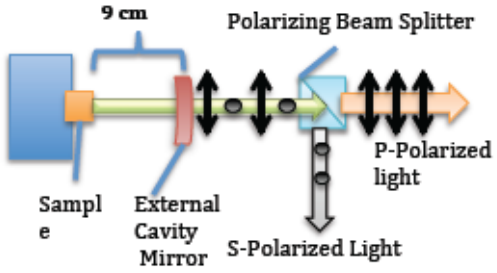

Figu eam splitter to separate S-polarized and P-polarized light.

Then, a curved mirror with around 45% reflectivity was used to switch the polarization. In this case, the sample was emitting mainly P-polarized light which meant the mirror was used to reflect the small amount of S-polarized light back in and switch the polarization of the output beam to S-polarized. The mirror was placed 3.5 cm away from the beam splitter as shown in Figure 7.

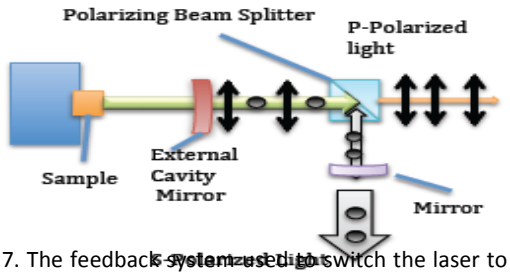

Figure 7. The feedback system used to switch the laser to S-polarized. An additional curved mirror reflects back S-polarized light.

A curved mirror was used for focusing the diverging beam back on the sample. The spectra and corresponding powers of both the S-polarized and P-polarized light at 4.9 W, 6.2 W, 7.4 W, 8.6 W, and 9.9 W.

For the second part of the research, the laser set-up had to be changed to a v-cavity like the one in Figure 8.

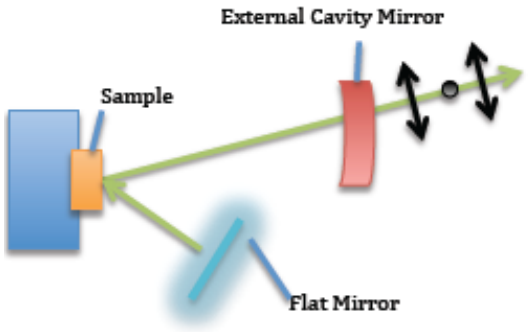

Figure 8. The V-cavity set-up results in light passing through the sample twice.

The output coupler was the same as before. In this set-up, the distance between the sample and the output coupler was 7.5 cm and the distance between the sample and the flat mirror was 1.5 cm. These distances were calculated the same way as the cavity length in the first set-up was calculated (using Matlab; see Eq. 1, Eq. 2, and Eq. 3). A polarizing beam splitter was placed in front of the flat mirror and an additional mirror with a 10 cm ROC was used to reflect the S-polarized light back into the laser (see Figure. 9) and switch the polarization.

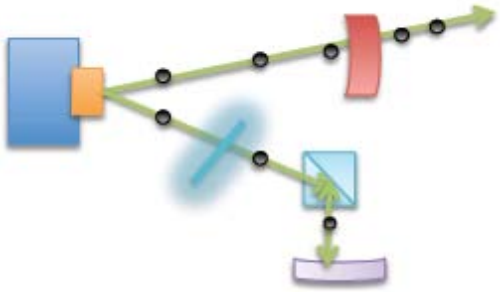

Figure 9. The feedback system in the V-cavity set-up. A high reflectivity curved mirror switches the laser to S-polarized.

The lasing spectra and powers of the output beam with and without the feedback system were taken at the same current values as before. A linear polarizer was used to confirm the initial polarization of the output beam, without the feedback, was P-polarized and then to confirm the polarization with the feedback had switched to S.

Results and Discussion

The free lasing output power graph (Figure. 10) shows that the laser was emitting as much as 2.4 watts of power, thus demonstrating the high output power of OP-VECSELs. The free lasing spectrum (Figure 11) shows the lasing wavelength was around 980 nm, as was expected, and the spectrum was good with a single peak corresponding to the wavelength at which gains exceed loss.

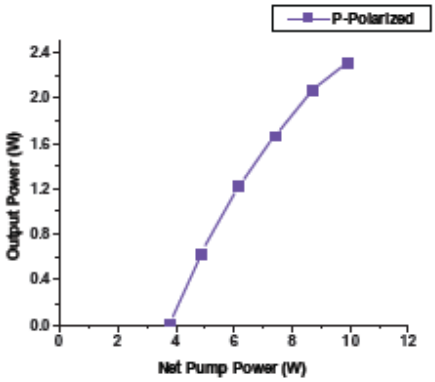

Figure 10. The free lasing total output power with respect to the net pump power. The laser is P-polarized.

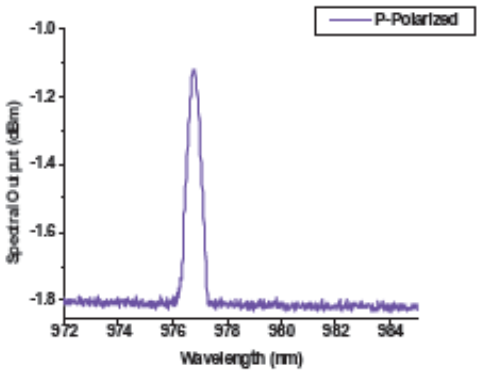

Figure 11. A sample free lasing spectrum showing spectral output (dBm) with respect to wavelength (nm).

The results for the linear cavity set-up confirmed the laser was linearly polarized. The output power graph of Sand P-polarized light (Figure. 12), which was measured using the polarizing beam splitter, shows the light was almost completely P-polarized. The spectra of P-polarized (Figure. 13) and S-polarized (Figure. 14) light show a slight shift in the wavelength. The small peak corresponding to S-polarized light further

demonstrates most of the output power was P-polarized.

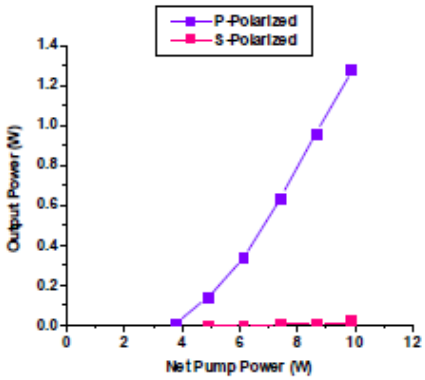

Figure 12. The output power of P- and S-polarized light with respect to the net pump power.

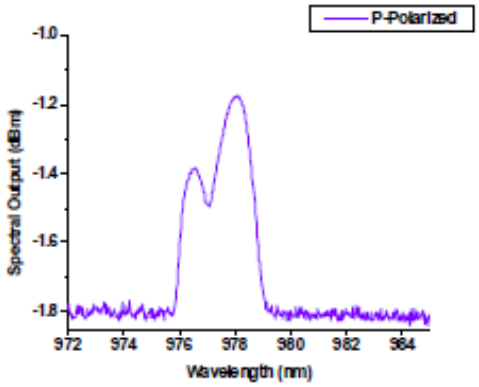

Figure 13. The last spectrum of P- polarized light.

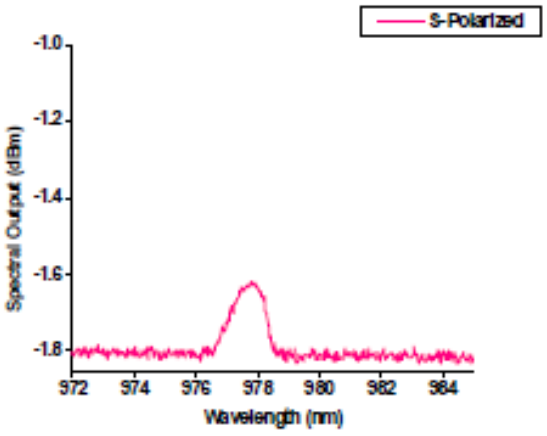

Figure 14. The lasing spectrum of S-polarized light.

The results of the feedback system in the linear cavity set-up show the polarization was successfully switched from P- to S-polarized. The output power graph (Figure. 15) shows that using the curved mirror to reflect back the S-polarized light resulted in the P-polarized output power decreasing to almost zero and the S-polarized output power increasing to around 0.6 W.

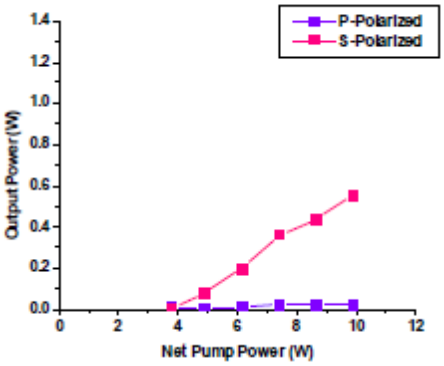

Figure 15. The output power for P-polarized and S-polarized light using a curved mirror to switch the polarization.

Therefore, although the polarization was successfully switched, there was a decrease in the total power due to the reflectivity of the curved mirror (~45%) and the power loss resulting from the output beam having to travel through an additional mirror. Also, the lasing spectra of the S-polarized (Figure. 16) and P-polarized light (Figure. 17) after the polarization had been switched show that compared to the spectra without the feedback system, there are a lot of additional small peaks. These spectra affects were expected because of the addition of another mirror in the output beam.

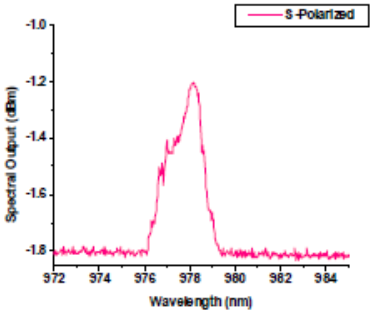

Figure 16. The lasing spectrum of S-polarized light using a curved mirror to switch the polarization.

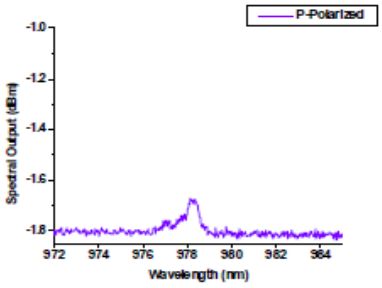

Figure 17. The lasing spectrum of P-polarized light using a curved mirror to switch the polarization.

The second part of the experiment was to use a V-cavity to switch the polarization. The results from the V-cavity without the feedback
system show the laser continued to emit P-Polarized light around 980 nm, as expected (See Figure. 18 and Figure. 19).

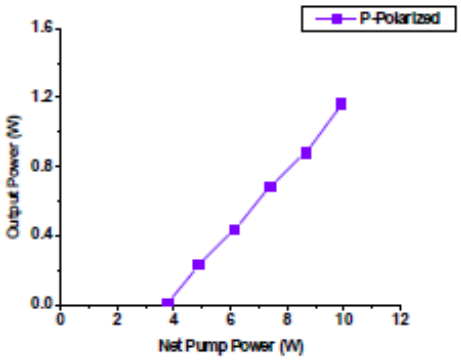

Figure 18. The total output power without the feedback (P-polarized) in the V-cavity.

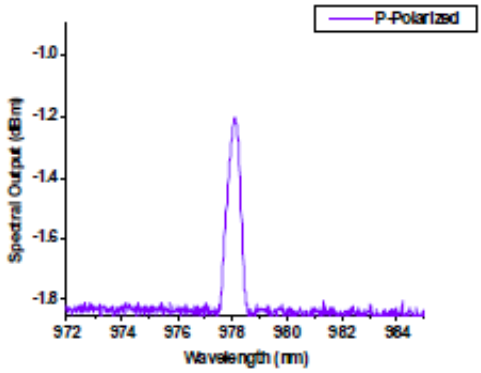

Figure 19. The lasing spectrum without the feedback in the V-cavity (P-polarized).

The addition of a curved mirror to the V-cavity successfully switched the polarization to S-polarized. The output powers (Figure. 20) and spectrum (Figure. 21) with the feedback were almost the same as the results without the feedback.

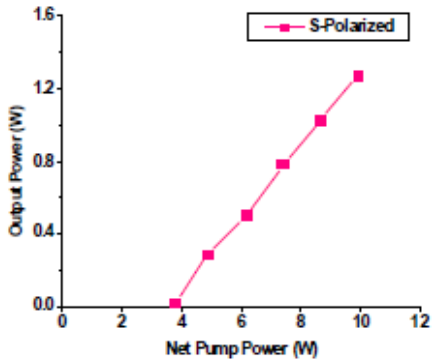

Figure 20. The total output power with the feedback (S-polarized) in the V-cavity.

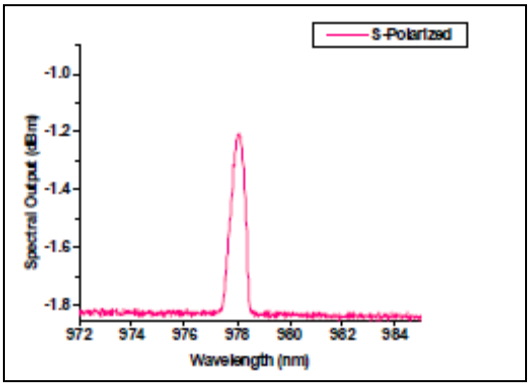

Figure 21. The lasing spectrum with the feedback in the V-cavity (S-polarized).

Therefore, in the case of the V-cavity, the polarization was switched without the power losses and spectrum effects that were seen in the linear cavity. The spectrum of the S-polarized light was almost the same as the spectrum of the P-polarized light. This was expected because in the case of the V-cavity, the mirror that was used to switch the polarization was not placed in the output beam. This meant there were not power loss and spectrum effects resulting from the output beam traveling through an additional mirror. Also, a higher reflectivity mirror (~85%) could be used since the transmitted light did not have to be measured in the case of the Vcavity
(the output beam was not emerging from the mirror).

Conclusions

OP-VECSELs are a specific type of high-power semiconductor lasers that emit Gaussian shaped beams. There are so many different laser applications in which the radiation must be linearly polarized and in which control over the polarization is critical for function. As a result, this research project was aimed at studying the polarization of a OPVECSEL and looking at a method of switching the polarization. In the first
part of my experiment, the polarizing beam splitter in a linear cavity set-up confirmed the linear polarization, which was P-polarized in this case. In the second part of the experiment, a curved mirror was used to reflect S-polarized light back on the sample switching the polarization from P- to S-polarized. In this linear cavity set-up, the addition of acurved mirror in the output beam resulted in a decrease in the total power and additional small peaks in the spectra. In the second part of the experiment, a different type of cavity was used to examine the polarization. The polarizing beam splitter was used again to

confirm the laser remained Ppolarized after changing to a V-cavity. Then, a high-reflectivity curved mirror was used to reflect back the S-polarized light and switch the laser's polarization. Although in both cases the polarization was switched, using a V-cavity eliminated power losses and spectra effects.

References

1. Fallahi, M.; Fan, L. *IEEE Photonic. Tech. L.* 2008, pp. 1-3.

2. Kuznestov, M.; Sprague, H.; Morradian, A. *IEE Photonic. Tech. L.* 1997, *9*, pp. 1063-1065.

3. Hessenius, C.; Terry. N.; Fallahi, M.; Moloney, J.; Bedford, R.; *Optics Letters*, pp. 3060-3062.

4. Siegman, A.; *Lasers,* 1st ed.; University Science Books: 1996.

5. Kuznetscov, M.; *Semiconductor Disk Lasers. Physics and Technology;* WILEY-VCH Verlag GmbH & Co. KGaA: Weinheim, 2010.

6. Fallahi, M.; Moloney, J.; Fan, L.; *Proc. Of SPIE*, 2006, 6127, pp. 61270C-1- 61270C-9.

7. Kaneda, Y.; Yarborough, J. *Optics Letters,* 2008, 33, pp. 1705-1707.

Acknowledgements

Funds for this research were provided by the Center on Materials and Devices for Information and Technology Research (CMDITR), and the NSF Science and Technology Center No. DMR 0120967. I would also like to acknowledge the graduate student mentors Chris Hessenius and Michal Lukowski, faculty mentor Mahmoud Fallahi, program coordinators Kimberly Sierra Cajas and Trin Riojas, and REU assistant Amanda Anderson.

KATHERINE WILLIAMS-DUHAMEL is a senior at the University of Massachusetts Amherst studying Chemistry. Her goal is to graduate and hopefully continue her education in the sciences through either a PhD program or a MS program.

Encapsulation and Durability Study of Organic Electrochromic Devices

RALPH ILUNGA, Massachusetts Institute of Technology
Hyungchul Kim, Dr. Samuel Graham, Georgia Institute of Technology

Introduction

Electrochromic devices (ECDs) are devices that change color reversibly to accommodate the transmission, absorption, or reflection of light when a potential difference is applied. ECDs have limitless applications; by controlling the amount of light and heat that enters a space, ECDs provide energy efficient alternatives to current heating, cooling, and lighting methods. For example, ECDs can be used to modulate the shade of the windows in aircraft, buildings, rear-view mirrors, or various other display applications. A problem with ECDs is the competitive redox reactions, between the polymers inside the devices and the water vapor and oxygen in the atmosphere, that limit device lifetimes. Therefore, the packaging of ECDs must be so as to minimize the permeation of water vapor and oxygen.

1

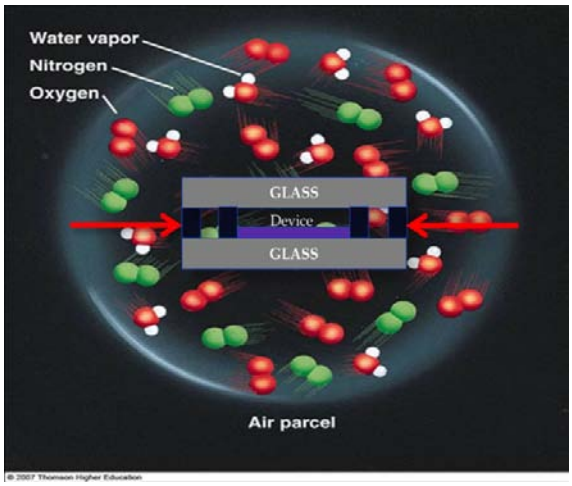

Figure 1. The figure above shows gas particles from the atmosphere permeating through the sealing barrier of an ECD.

The Graham Group and Reynolds Research Group have previously shown that packaging that utilizes rigid glass substrates (the substrates are coated with Indium Tin Oxide), with ADCO PVS 101 sealant, and a thin aluminum oxide overcoat is high performing. The electrochromic polymer (ECP) used in the previous study was magenta colored. This research project compares the performance of 3M VHB tape to the ADCO sealant, and the

properties of a black ECP to the magenta ECP. This study is significant because there are few existing reliability studies on organic electrochromic devices, and different colored polymers have different properties. Since there might be applications where greater flexibility is desired, this project will also study flexible glass and plastic substrates while using the rigid glass substrate as a benchmark.

Experimental Methods

Figure 2. The glove box in the Reynolds lab that was used in the fabrication of a number of the devices.

Before any experiments can be performed, the devices first need to be fabricated. In the Reynolds lab, ECP and MCCP (minimal color changing polymer) is sprayed onto two different substrates that will become joined together with sealant/adhesive. Once sprayed to the proper absorbance, the substrates are transferred to a glove box (or inert atmosphere) where the sealant/adhesive will be applied to the inner and outer areas of the ECP substrate. The correct

amount of gel electrolyte is then added to the inner area.

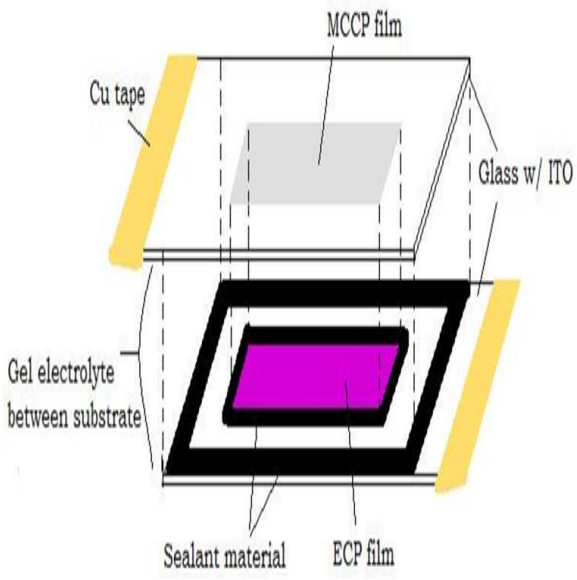

In the case of the ADCO seal, the sealant needs to be degassed by heating it on a hot plate in a glove box at 110°C for at least twelve hours. The ADCO seal also needs to be heated for five to ten minutes at 110°C before and after the MCCP substrate is applied to the ECP substrate. If the gel electrolyte spills over the ADCO seal, then the sealing performance of the ADCO seal will be greatly reduced.

After the devices have been sealed in a glove box, copper is wrapped around the electrodes, and the devices are numbered by etching with a diamond tipped pen.

The first round of fabrication involved thirty devices: fifteen devices with magenta ECP and another fifteen with black ECP. In each subset of fifteen devices, six were sealed with the ADCO sealant and the other six were sealed with 3M tape. The three left over were extras that were kept in case of errors.

There were three exposure or testing conditions:

1. In the humidity chamber in the Graham lab at 80% relative humidity and 50°C.
2. On a lab bench at normal atmospheric conditions (humidity and temperature measured.)
3. On the roof of the J. Erskine Love Manufacturing Building (humidity and temperature measured.)

Rigid Glass Substrate	**Magenta ECP**		**Black ECP**	
	ADCO Sealant	**3M Tape**	**ADCO Sealant**	**3M Tape**
Humidity Chamber	2 ECDs	2 ECDs	2 ECDs	2 ECDs
Love Building Roof	2 ECDs	2 ECDs	2 ECDs	2 ECDs
Lab Bench	2 ECDs	2 ECDs	2 ECDs	2 ECDs

Table 1. A table of all devices made (extra devices made are not included) for the first round of testing.

Two ADCO devices and two 3M devices from each subset were placed in each exposure condition. The current and transmittance of the devices were monitored twice a week by switching the devices for fifty cycles, while measuring conductance and transmittance with a portable USB potentiostat and a fiber optic spectrophotometer (StellarNet) that was connected to a laptop computer.

The second round of fabrication involved four magenta devices sealed with the ADCO seal and placed on a lab bench. Two devices would have a flexible glass substrate and the other two would have a PET plastic substrate.

Magenta ECP, ADCO Sealant		
Lab Bench	**Flexible Glass**	**PET Plastic**
	2 ECDs	2 ECDs

Table 2. A table of all devices made (extra devices are not included) for the second round of testing.

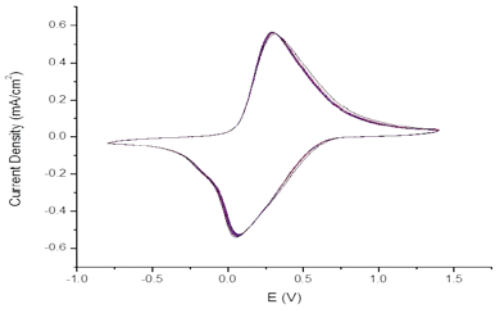

Figure 3. Successful break-in of 3M magenta ECD. The figure shows every ten scans starting from the fifth scan up until the seventy fifth scan.

Results and Discussion

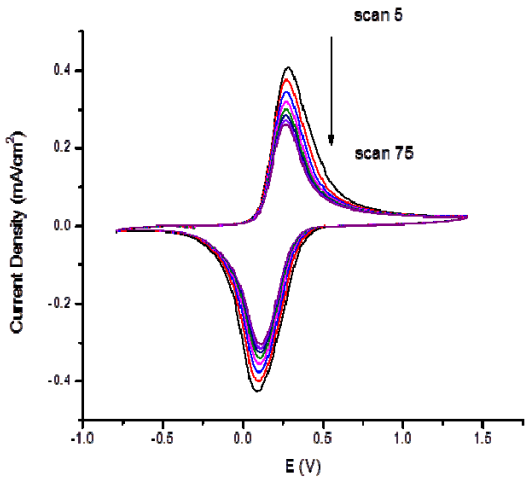

Figure 4. Unsuccessful break-in of ADCO magenta ECD. The figure shows every ten scans starting from the fifth scan up until the seventy fifth scan.

Before the devices could be experimented on, they first needed to be "broken in" to optimize the device contrast by inducing electrolyte ion intercalation. The break-in procedure was done through cyclic voltammetry (CV). The devices sealed with 3M managed to break-in successfully; Figure 3 shows how the current density of the 3M device increases and stabilizes with increasing CV scans. The devices sealed with the ADCO seal did not break-in as expected; Figure 4 shows how the current density of the magenta ADCO device decreases with increasing CV scans – an undesirable result. Due to the unexpected and undesirable performance of the devices sealed with the ADCO seal, a further study on the cause of the unwanted results needed to be completed before the research project could proceed.

One theory proposed is that the presence, or lack thereof, of oxygen or moisture could affect device performance on break-in. The presence of oxygen could allow for easier polymer oxidation, leading to faster device breaking. The presence of moisture could allow for further ion dissociation, which would assist in increasing the ionic conductivity of the gel electrolyte, leading also to faster device break-in. However, these results are contrary to previously observed results in the Reynolds group and in the previously referred to published work. To test this theory, three ADCO magenta ECDs were made: one device was made in the glove box and used electrolyte from the glove box (no oxygen or moisture present), another device was made on the lab bench and used electrolyte made on the lab bench (moisture present and oxygen present), and the last device was made on the lab bench but used electrolyte from the glove box (minimal moisture present, but oxygen present.)

Another possible source of error could have come from side reactions of materials possibly leached from the ADCO sealant material into the gel electrolyte. To test this, an electrochemistry experiment was completed where some ADCO seal was placed within gel electrolyte and tested periodically by CV cycling.

Conclusions

So far, the tests done for both of these theories do not show anything conclusive, but the tests are still ongoing and more theories about the cause of the improper behavior of the ADCO ECDs are still being considered.

Once the ADCO ECDs start breaking-in properly again, this study can continue as planned.

References

1. Image of Air Parcel. http://geospatial.gsu.edu. (Accessed July 25, 2012.)

Acknowledgments

Funds for this research were provided by the Center on Materials and Devices for Information Technology Research (CMDITR), and the NSF Science and Technology Center No. DMR 0120967. I would also like to thank Dr. Samuel Graham, Dr. Aubrey Dyer, Dr. Eric Shen, Dr. Keith Oden, Hyungchul Kim, Malvina Kowalik, and all other contributors.

RALPH ILUMGA is a rising junior at the Massachusetts Institute of Technology. Upon graduation, he plans to pursue a masters and a PhD.

Characterization of Organic Electro-Optic Chromophores

DAVID LEVONIAN, Massachusetts Institute of Technology
Delwin Elder, Larry Dalton, University of Washington

Introduction

Demand for internet bandwidth has been exponentially increasing since the 1990's and shows no sign of slowing. Almost all internet traffic flows through fiber-optic networks at some point during its journey. Fiber optic networks, which transmit their signal as light confined in a glass fiber by total internal reflection, offer fast, long-distance communication.

To transmit a signal over fiber optics, a laser is amplitude modulated and fed into the fiber. Dips and peaks in amplitude are picked up by a photodiode at the other end of the fiber and interpreted as 1's or 0's. Techniques for modulating the signal have seen many improvements and iterations.

The current technology for modulator employs the Pockels effect to create constructive and destructive interference in light. The Pockels effect is the change in the refractive index of a material when a electric field is applied. Materials that exhibit the Pockels effect are referred to as electro optic materials. In a Mach-Zehnder modulator, light is split and travels down two paths filled with elctro optic material. When an electric field is applied in one of the paths, the index of refraction in one path changes, phase shifting the light with respect to the other path. The two light beams are then added back together. Adjusting the applied voltage controls the phase angle and allows the light in the modulator to constructively or destructively interfere.

The current state of the art in electro optic materials is lithium niobate. When electric field is applied to lithium niobate, the crystal lattice stretches, changing the index of refraction.

Recently, organic chromophores have been explored as an alternative electro optic material.

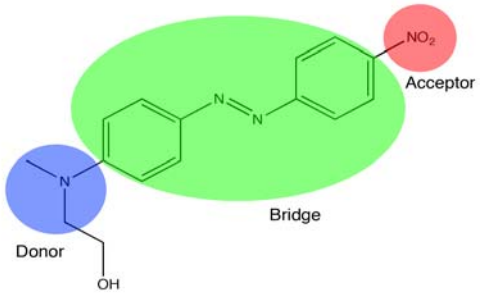

Figure 1. Standard organic chromophore structure, with nitrogen electron donor, conjugated pi bond bridge and electron acceptor.

Organic chromophores consist of an eletron donor and an electron acceptor connected by a 'bridge' of conjugated pi bonds. When an electric field is applied, electrons shift from the LUMO to the HOMO, altering the materials refractive index. Because the electro optic effect in organic chromophores is due to the movement of electrons rather than shifts in molecular position, organic electro optic materials change refractive index in response to applied field much faster than lithium niobate. This quicker response time allows devices constructed with them to transmit more data.

Although organic chromophores have the potential to perform better than lithium niobate, several hurdles must be overcome before they can be used in commercial devices. The most formidable hurdle is order. The majority of organic chromophores are amorphous solids rather than crystals. In amorphous form, their electro optic effect is weak, as individual molecules are oriented isotropically.

In order to align the molecules, an electric field must be applied across the material. The electric field then acts on the permanent dipoles of the molecules, ordering them. Unfortunately, if chromophores are to be used in optical devices, there are limits on the strength of electric fields that can be applied. Therefore, research into chromophores that highly align under weak electric fields is valuable.

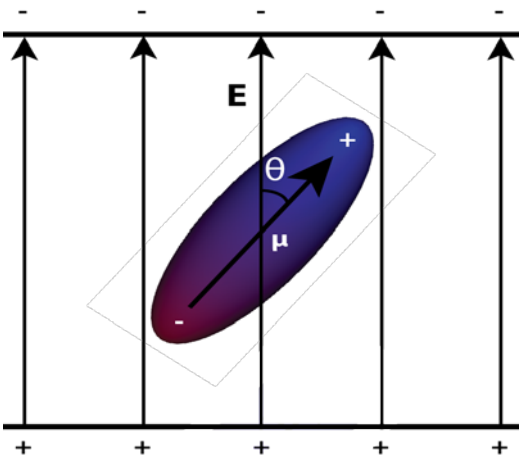

Figure 2. Schematic of poling. The permanent dipoles in the chromophores are rotated by electric field

One barrier to the alignment of chromophores is the molecules' own electric field. Since organic chromophores have a permanent dipole moment, it is energetically favorable for them to anti-align head to tail with each other. The recently synthesized chromophore, DLD-166 attempts to solve this problem with the addition of coumarin chains to the side of the usual donor-bridge-acceptor structure.

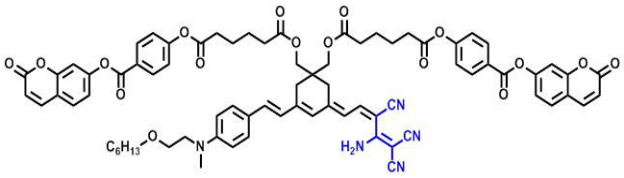

Figure 3. The structure of DLD-166 (top) and YLD-124 (bottom)

The purpose of the coumarin side chains is two-fold: to keep the individual chromophores separated in order to weaken their dipole interactions and to confine the chromophores in to planes via coumarin-coumarin interactions.

Experimental Methods

In order to measure the electro optic properties of an organic chromophore, the material must first be poled. To this end, the chromophore is incorporated into a device that allows for easy optical measurements and application of high electric field to the material.

First, a glass slide half covered with a precoated layer of conductive indium tin oxide is sonicated in acetone and IPA to insure a clean surface. The device is then spin coated with a layer of titanium oxide sol-gel. Then, the slide is placed in a tube furnace to produce a thin, uniform layer of TiO2 that forms an insulating barrier.

The chromophore is dissolved in a suitable solvent (trichloroethane in the case of DLD-166) and spin-coated onto the device. The device is then placed in a vacuum furnace overnight to remove solvent from the layer.

Finally, gold is sputtered onto the device through a mask, which produces a dumbbell shaped pattern of gold on the surface that straddles the edge of the ITO covering.

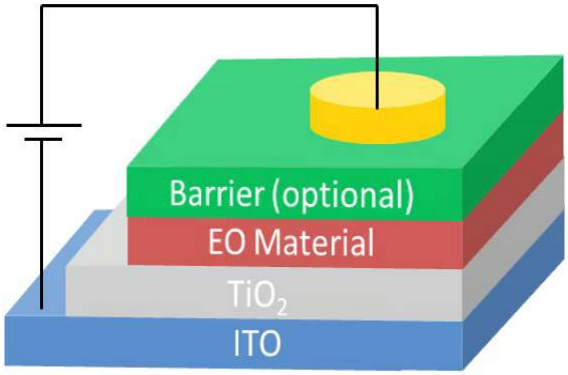

Figure 4. Poling device structure.

The end result of the process is a layer of chromohpore roughly one micron thick and a layer of TiO2 one hundred nanometers thick sandwiched between two conductors. By using silver paste to connect wires to the ITO and gold surfaces, one can apply voltage across the chromophore layer. Furthermore, the TiO2 layer has a very high resistance to electrical breakdown with low leakage current up to over 100 V.

Because the distance between the poling electrodes is so small, relatively small voltages can produce large electric fields in the chromophore. If the chromophore is heated to its glass transition temperature while electic field is applied, poling will occur.

Since the ITO and glass are transparent, in situ measurement of the poling progress is possible with the Teng Man method. In the Teng Man method a sinusoidal electric signal is applied

between the gold and ITO electrodes. Simultaneously, a laser is shown through the sample from the underside, passing through the chromophore layer and bouncing off the gold electrode.

The laser beam passes through a Soleil-Babinet compensator, which preferentially phase shifts light that is polarized in the plane of the sample. By measuring the intensity of the laser with a photodiode and comparing its shifts in intensity with respect to the input voltage, one can determine the r_{33} of the material, or the change in refractive index with respect to the applied electric field. Since this technique does not require direct contact with the sample, it can be used while the sample is being poled, allowing the process to be measured while it is in process.

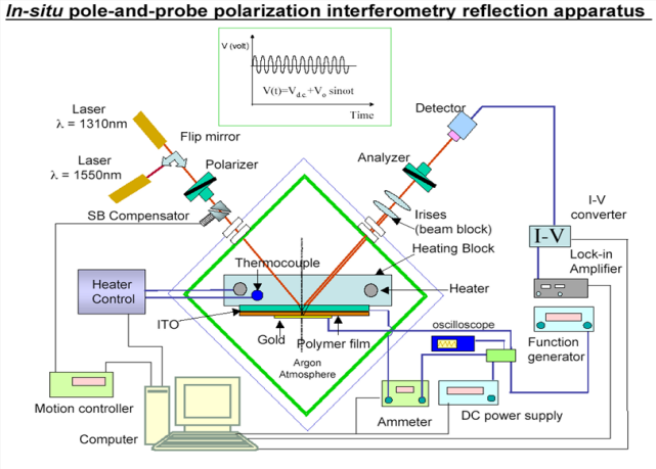

Figure 5. In-situ Teng Man measurement of poling.

The Teng Man method, while convenient, has potential inaccuracy because it assumes that the electro optic layer is perfectly transparent. The Attenuated Total Reflectance (ATR) method overcomes these inaccuracies, by probing the electrooptic properties of the sample with an evanescent rather than a propagating wave. ATR is used after the sample has finished poling to more accurately measure the r_{33} of the sample.

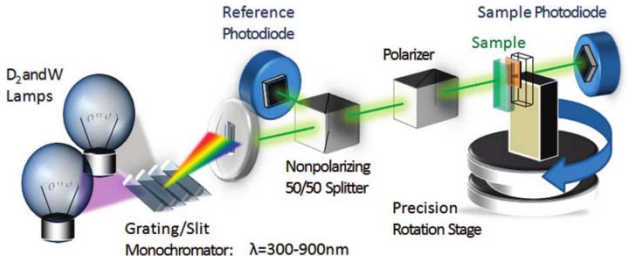

Figure 6. Variable-Angle Polarization Referenced Absorption Spectroscopy

Once the samples r_{33} has been determined via ATR, variable-angle polarization referenced absorbtion spectroscopy (VAPRAS) is used to determine the average order of the film of chromophores. The VAPRAS measures the attenuation of different polarizations as they pass through the sample at different angles of incidence. At the same time a variable angle spectroscopic ellipsometer (VASE) can be used to solve for the complex refractive index of every layer of the film. By combining these two data sets, one can measure the average $\cos^3\theta$, where θ is the angle between the chromophores' dipole moments and the direction of the poling field.

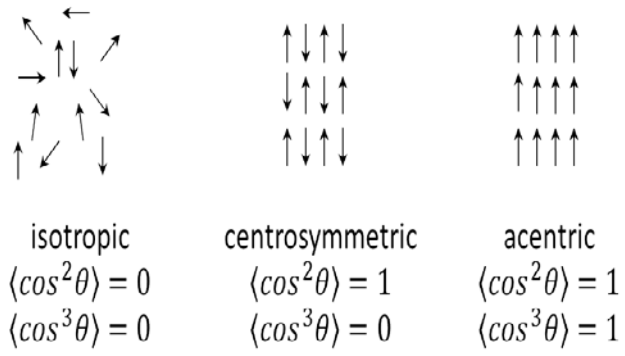

Figure 7. Order parameters in the amorphous chromophore film.

Results and Discussion

UV-Vis spectroscopy of DLD-166 revealed that its peak wavelength was much longer than similar chromophores, likely due to its weaker electron accepter.

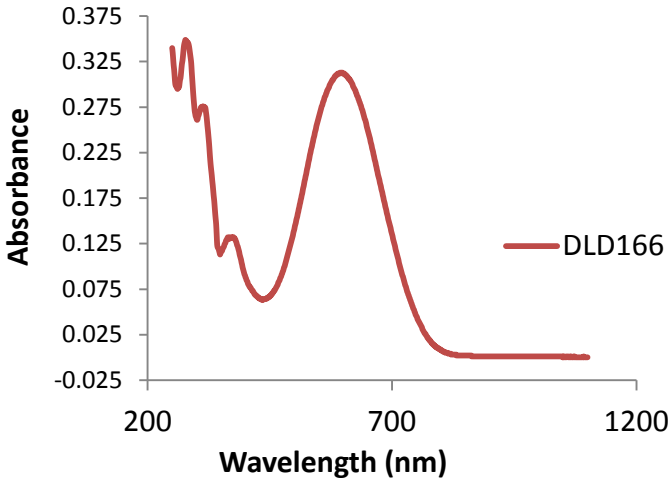

Figure 8. UV-Vis of DLD-166 in $CHCl_3$

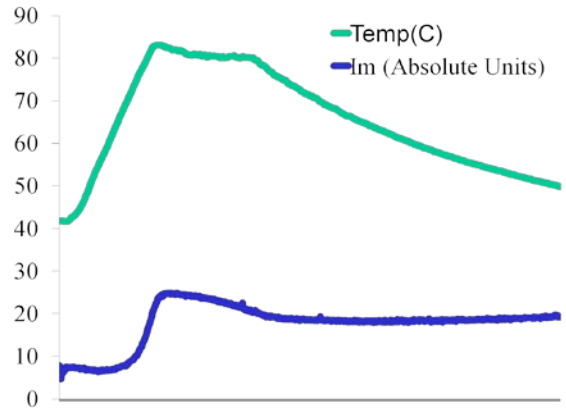

Figure 9. Typical data from in-situ poling measurement

The measured r_{33} for DLD-166 averaged 31.6 pm\V with an average poling efficiency of 0.63. The T_G of DLD-166 was determined to be 79.1°C through differential scanning calorimetry. After ATR the samples were stripped of their gold electrodes with an iodine solution and prepared for VAPRAS.

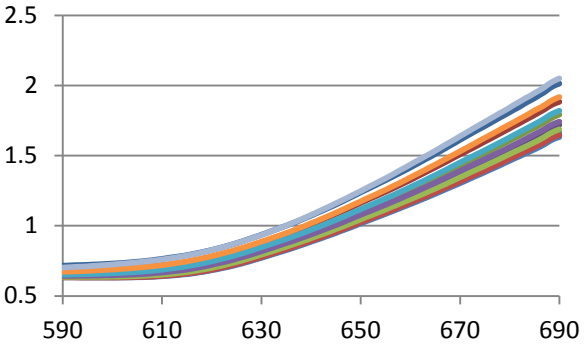

Figure 10. VAPRAS data from one sample of DLD-166

The average $\langle\cos^2\theta\rangle$ coefficient of the poled samples determined to be 0.11 by the Graf method followed by iterative Jones Matrix method. The average $\langle\cos^2\theta\rangle$ for YLD-124 after poling is only 0.035.

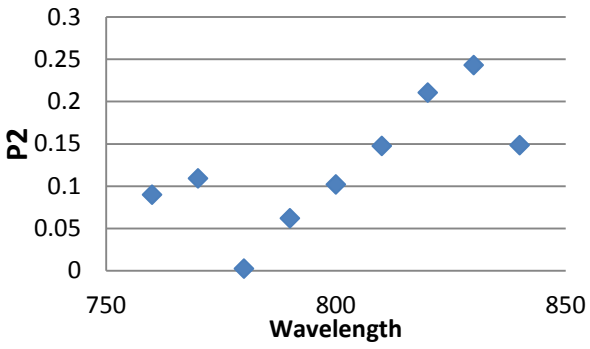

Figure 11. Average DLD-166 P2 measurement for each wavelength measured by VAPRAS

Conclusions

Coumarin side chains can significantly increase the order in poled organic electrooptic films. This has the potential to boost the electrooptic performance of such molecules.

However, the electron receptor on DLD-166 is much weaker than previously tested chromophores, notably YLD-124, which means that its overall electrooptic properties are weaker. Adding a stronger electron acceptor will be the goal of future synthetic work.

References

1. Park, Dong Hun; Lee, Chi; Herman, Warren. *Optical Society of America.* 2006, *14*, 8866-8884.

2. Dalton, Larry; Benight, Stephanie. *Polymers.* 2011, *3*, 1325-1351.

3. Michelotti, F.; Toussaere, R.; Levenson, J.; Liang, J.; Zyss, E. *J. Appl. Phys,.* 1996, 80, 1773-1778.

4. Sullivan, P. A.; Dalton, L. R. Acc. Chem. Res. 2010, 43, 10-18.

5. Dalton, L. R.; Sullivan, P. A.; Bale, D. H. Chem. Rev. 2010, 110, 25-55.

6. Benight, S. J.; Johnson, L. E.; Barnes, R.; Olbricht, B. C.; Bale, D. H.; Reid, Ph. J.; Eichinger, B. E.; Dalton, L. R.; Sullivan, P. A. J. Phys. Chem. B 2010, 114, 11949-11956.

7. Olbricht, B. C.; Sullivan, P. A.; Dennis, P. C.; Hurst, J. T.; Johnson, L. E.; Benight, S. J.; Davies, J. A.; Chen, A.; Eichinger, B. E.; Reid, P. J.; Dalton, L. R.; Robinson, B. H. J. Phys. Chem. B 2011, 115, 231-241

8. Figi,Harry; Bale, Denise; Szep, Attila; Dalton, Larry; Chen, Antao. J Opt. Soc. Am. B. 2011, 28, 2291-2301.

Acknowledgments

Funds for this research were provided by the Center on Materials and Devices for Information Technology Research (CMDITR), and the NSF Science and Technology Center (No. DMR 0120967),

NSF Research Experiences for Undergraduates Program Hooked on Photonics (No. CHE 0851730), and Multi-Scale Theory Guided Development of Transformative Polymeric and Dendritic Electroactive Materials. (Grant No. DMR-0905686).

Many thanks to Dr. Antao Chen for use of his lab for fabrication and measurement of samples.

DAVID LEVONIAN is currently finishing his senior year at MIT. He hopes to do graduate work in photonics.

Inorganic-Organic Hybrid Bulk Heterojunction Solar Cells

BRITTANI C. LOVE, Shepherd University
Adam Colbert, David S. Ginger, University of Washington

Introduction

Semiconducting colloidal quantum dots (QD) are of interest as light absorbers for low-cost solar cells because their band gaps are size-tunable due to the quantum confinement effect.[1-3] This property enables broadband light absorption into the near-infrared to better match the solar spectrum. We synthesized hybrid photovoltaics based on type-II bulk heterojunctions between conjugated polymers and inorganic QDs to investigate the performance of these devices.

Type II bulk heterojunctions (BHJ) are made by blending a charge donor material and charge acceptor material. The blend is deposited as a thin film for the active layer of a photovoltaic device. The donor-acceptor blend is spun-cast as a thin film and will then phase segregate and form separate domains throughout the film. As light is absorbed, an exciton—a coulombically bound electron/hole pair—is formed in either component of the blend. Ideally, excitons on the donor can efficiently transfer electrons to the acceptor and excitons on the acceptor can transfer positive charge (holes) to the donor. The charges then separate, electrons travel through the acceptor and holes through the donor to be collected at the anode and cathode. Donor-acceptor charge transfer is the fundamental process that allows a BHJ to extract current from incident light. In figure 1, we schematically depict the charge generation process in a BHJ.

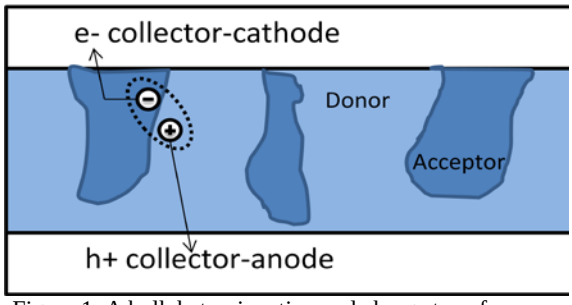

Figure 1. A bulk heterojunction and charge transfer.

In this study, the polymer P3HT (poly-3(hexylthiophene)) was blended with lead sulfide (PbS) QDs to create a BHJ film for photovoltaic devices. In this blend, the P3HT is the donor material and transports holes. PbS is the acceptor material and transports electrons.

Bismuth sulfide (Bi_2S_3) nanocrystals are also of interest for BHJ devices as an acceptor material because of their low cost and low toxicity relative to Pb chalcogenides. Bi_2S_3 has been studied in bilayer device structures with P3HT[4], but this is, we believe, the first study of Bi_2S_3 nanocrystals in a bulk heterojunction with P3HT and another donor polymer, PCPDTBT. In Figure 2, we show the energy levels of materials used in this study relative to vacuum.

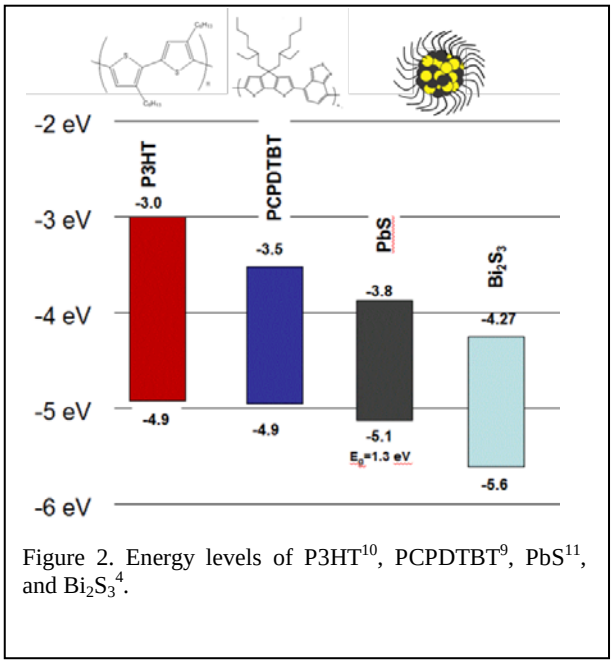

Figure 2. Energy levels of P3HT[10], PCPDTBT[9], PbS[11], and Bi_2S_3[4].

Ligands are molecules that form complexes with metal compounds. Ligands allow the synthesis of colloidal quantum dots by providing solubility and controlling the shape of the nanocrystal. The ligand shell coating the particles aids in preventing aggregation. Oleic acid ligands cap PbS quantum dots following synthesis, but act as insulators and do not facilitate charge transfer. Oleic acid ligands are generally exchanged for shorter ligands on quantum dots for charge and energy transfer studies. In this study, we focus on the effects of the ligand capping PbS QDs on charge transfer and device performance

in BHJ solar cells with the polymer P3HT. In Figure 3, we show the chemical structure of each ligand used in this study. Note that the cetyltrimethylammonium bromide ligand will only attach Br^- to the surface of the QD.

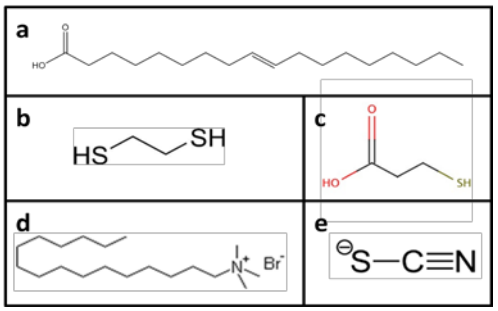

Figure 3. Ligands a) Oleic Acid b) Ethanedithiol (EDT) c) Mercaptapropanoic Acid (MPA) d) Cetyltrimethylammonium Bromide e) Ammoinium Thiocyante

Previous studies have determined that thiol ligands can help passivate surface traps in quantum dots and help diminish recombination effects to device performace.[5] Another study has shown success using cetyltrimethylammonium bromide (CTAB) ligand treatments in quantum dot solar cells.[6] In this study, we exchange oleic acid ligands on the surface of PbS QDs with various thiol ligands and CTAB and characterize the functionality of BHJs with P3HT.

To interrogate the charge generation mechanism in our nanocrystals polymer blends we use photoinduced absorption spectroscopy (PIA). PIA is a pump-probe technique capable of measuring long lived excited states, such as structurally relaxed photogenerated charge carriers, called polarons. We excite the sample with a pump beam (frequency modulated at 200 Hz), while we scan the wavelength of a second light source we call the probe beam. A lock-in amplifier is used to detect very small (ppm) changes in the amount of transmitted probe light (dT). This value is normalized to the steady-state transmission (T) of the probe beam. A monochromater is used to block any light from the pump beam and the final dT/T values are corrected for photoluminescence. The lock-in amplifier is set with scattered pump light so that the X-channel is positive and in-phase. Negative dT/T values correspond to the induced absorption in the excited state, whereas positive dT/T values correspond to the absorbance of the material in the ground state. Knowing what the polaron absorption spectrum looks like, we can use PIA to determine if photoinduced charge transfer yields long lived charged species in our BHJ films.[7,8] Figure 4 shows a schematic of the PIA instrumentation.

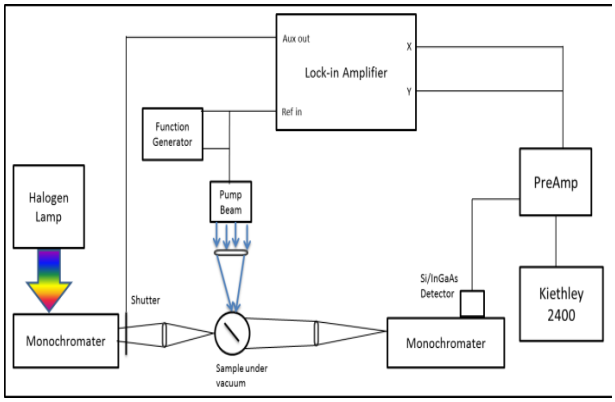

Figure 4. Photoinduced Absorption Spectroscopy

Devices are characterized by making several measurements to compare how well the device turns photons into electrical current. External Quantum Efficiency (EQE) compares the electoral current output by the device to the photon flux incident on the device.

$$EQE = \left(\frac{Photocurrent}{charge\ of\ one\ electron}\right)\left(\frac{energy\ of\ one\ photon}{total\ power\ of\ photons}\right) \quad (1)$$

Devices under illumination are also characterized by the following parameters: short circuit voltage, J_{sc}, open circuit voltage, V_{oc}, fill factor, FF, and power conversion efficiency, η. The J_{sc} is the maximum current of a device with no applied bias. V_{oc} is the difference in potential at the external contacts when no current is flowing. We tabulate $J_{sc,}$ $V_{oc,}$ and FF by measuring the current through the device as a function of applied bias. The FF is the maximum output power (J×V) of the device divided by the V_{oc} and J_{sc}.

$$FF = \frac{\overline{Max(JV)}}{V_{oc}J_{sc}} \quad (2)$$

Finally, the power conversion efficiency is a comparison of this calculated maximum power with the simulated power of the sun.

$$\eta\ (\%) = \frac{J_{sc}*FF*V_{oc}}{1\frac{kW}{m^2}} \quad (3)$$

Where 1kW/m^2 is the integrated A.M. 1.5G solar radiance.

Experimental Methods

PbS and Bi_2S_3 nanocrystals were synthesized using an air-free Schlenk line, hot injection method. Figure 5 shows a typical air-free, hot injection set up for synthesis on a Schlenk line.

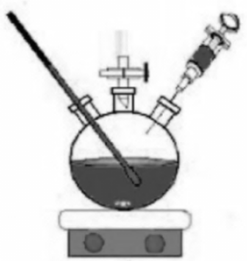

Figure 5. Hot injection synthesis

In the PbS synthesis, 450mg of PbO, 14g 1-Octadecene, and 1.2g of Oleic acid were added to a 3-neck flask and purged of O_2 and H_2O by heating to 100°C and purging with a vacuum over 60 minutes. The reaction flask was prepared by adding 4g 1-Octadecene (ODE) and 210µL of Hexamethyldisiloxane (HMDS) to another 3-neck flask and pulling vacuum for 5 minutes to remove O_2 and H_2O. The sulfur precursor was rapidly injected into the lead-oleate flask at predetermined temperature to create the desired size of dots—typically about 160 °C. The reaction mixture was cooled in a water bath then isolated and cleaned via subsequent precipitations in acetone and methanol. The final product was dried on an N_2 line and dissolved in chlorobenzene in a N_2 glove box.

The reagents used in the Bi_2S_3 synthesis were 1.005g Bismuth Acetate, 4g Oleic Acid, and 4g ODE in the reaction flask. The sulfur precursor was prepared using 4g ODE and 125µL of HMDS. After rapid injection at 170°C, the reaction is immediately cooled to 100°C and left to stir for one hour. The product is then isolated and cleaned using a 1:1 ratio cold toluene and anhydrous methanol. The final nanocrystals were suspended in chlorobenzene and blended with polymers.

Polymers were dissolved in chlorobenzene in an N_2 glove box and left to stir at 45°C for 4-6 hours. Both the PbS and polymer were filtered with .2µm and .45µm PTFE filters before combining in a 9:1 w/w PbS:P3HT blend.

Films were made by spin coating at 2000rpm for 1 minute onto cleaned glass/ITO substrates. Ligand treatments were all carried out during spin-coating by soaking the film in ligand solution twice for 1-2 minutes and washing with methanol. The ligands were all dissolved in Methanol and had the following concentration: EDT, 10mM; CTAB, 10mg/mL; MPA, 1mM; SCN, 10 mg/mL.

Top electrodes are made of a thin layer of MoO_3 and Ag which are evaporated onto the surface of the device. Figure 6 depicts the structure of our BHJ devices.

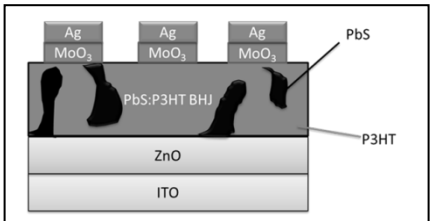

Figure 6. Device Structure

PIA spectroscopy was used to characterize the films using a 455nm LED pump beam and continuous wave probe beam from a tungsten-filament lamp scanning from 550-1750nm. External quantum efficiency measurements were made under illumination from a tungsten lamp followed by a double grating monochromator.

Results and Discussion

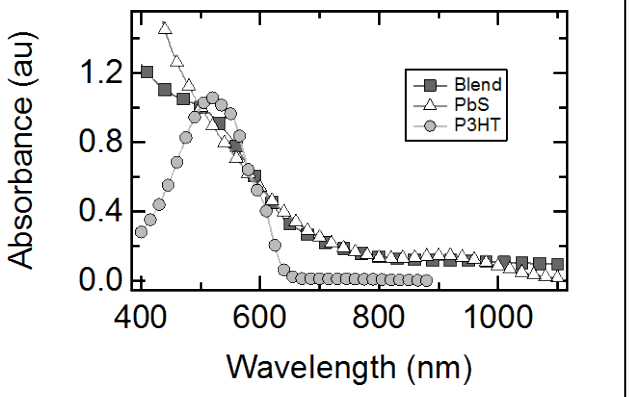

Figure 7. Absorbance Spectra of PbS, P3HT, and blend normalized to 500nm.

In figure 7 we show that the P3HT (circles) absorbs strongly in the visible region and does not absorb into the NIR. The PbS (triangles) absorbs well into the NIR region, with a quantum dot band gap of 1.3eV as indicated by the absorbance peak near 900nm. The blend of P3HT and PbS (squares) clearly shows a strongly absorbing region in the visible region from both the P3HT and PbS. The blend also absorbs into the NIR region, following the absorbance curve of the PbS.

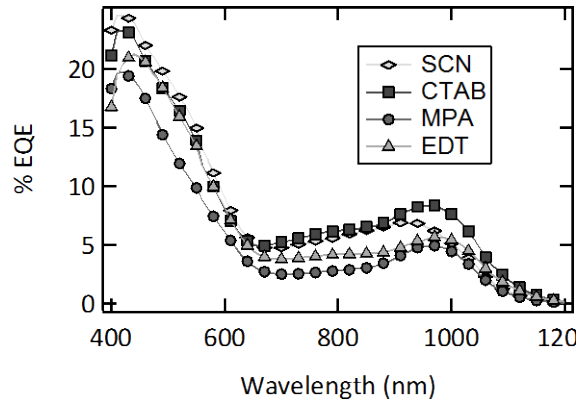

Figure 8. Device EQEs.

In figure 8, we show the external quantum efficiency of the P3HT:PbS devices. The EQEs are all very similar, but the SCN (diamonds) and CTAB (squares) ligand treated devices have a slightly higher EQE than the other devices. We observe a slightly lower response from the PbS in the EDT (triangles) treated device relative to the polymer, while we obtain the lowest overall EQE from the MPA (circles) treated blend.

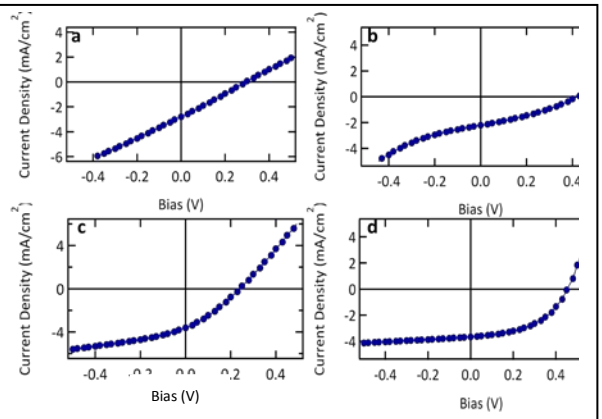

Figure 9. I-V curves under illumination of white light from a Xenon-Arc lamp of PbS:P3HT BHJ film with different ligands: a) EDT b) MPA c) CTAB d) SCN

In Figure 9, the light I-V curves of the PbS:P3HT devices show that SCN ligand treated devices yield the best performance due to the enhancements in both the value of the FF and the value of the V_{oc} with no loss in the J_{sc}.

	NH_4SCN	CTAB	MPA	EDT
V_{oc}	0.453	0.238	0.410	0.291
J_{sc}	-3.67	-3.37	-2.37	-2.8
FF (%)	48.0	30.3	32.1	26.1
η (%)	0.796	0.24	0.311	0.213

Table 1. Device characterization measurements.

We have tabulated these device performance metrics in Table 1. Overall, we observe SCN to be the best ligand treatment based on the JV behavior of these devices. The calculated FF for the SCN ligand treatment is 48%, while the other materials are 10% and 20% below the FF of SCN. The power conversion efficiency for these SCN treated dots is 0.8%, much higher than the others with values of about 0.2% each.

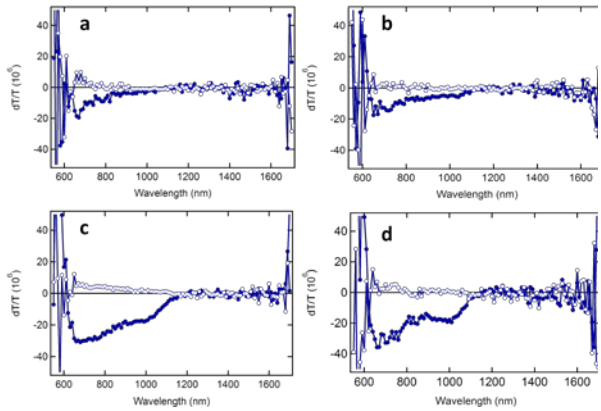

Figure 10. PIA spectra of PbS:P3HT BHJ film with different ligands: a) EDT b) MPA c) CTAB d) SCN

To further characterize the differences among ligand treatments for PbS polymer blends we present PIA data in Figure 10 showing polaron signal (long lived photogenerated excited states) in the SCN and CTAB ligand blends near 1000nm. This NIR PIA feature indicates that the P3HT has undergone charge transfer to the PbS, resulting in long-lived P3HT polarons. There is no polaron signal in the EDT and MPA blends, which suggests that either 1) photoinduced charge transfer has not taken place, or 2) charge transfer has occurred, but that the polaron lifetime is very

short and the charged species recombine too quickly to be measured using our instrumentation. Additional work focused on measuring photoluminescence excitation spectra and PIA polaron lifetimes to distinguish between these two possible scenarios are presently under way.

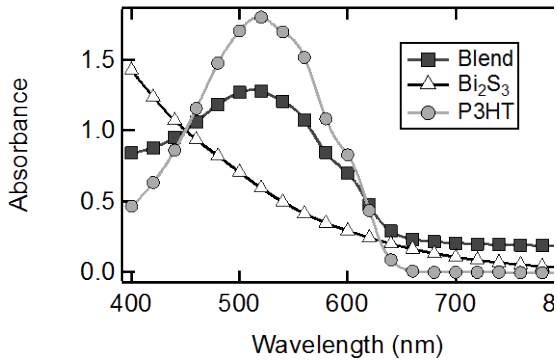

Figure 11. Absorbance spectra of neat P3HT, neat Bi_2S_3, and the blend of P3HT and Bi_2S_3 normalized to 450nm.

In Figure 11 we show that Bi_2S_3 (triangles) absorbs further into the red/NIR region than P3HT (circles). The blend of Bi_2S_3 and P3HT (squares) adopts the absorption features of both Bi_2S_3 and P3HT and absorbs further in red/NIR than P3HT alone.

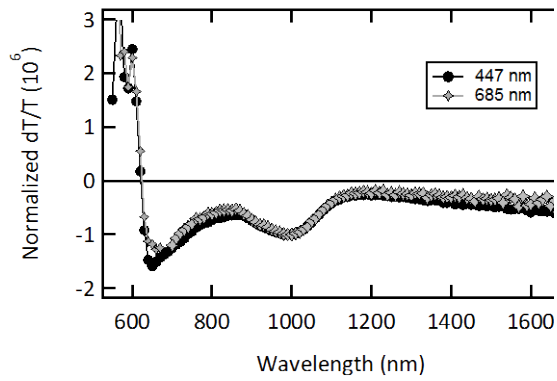

Figure 12. PIA spectra of Bi_2S_3:P3HT BHJ selectively excited at 447nm and 685nm.

To determine whether the nanocrystals in Bi_2S_3:P3HT BHJ are able to undergo photoinduced hole transfer to the polymer we collected a PIA spectrum by selectively exciting the nanocrystals at 685 nm and compared it to that obtain upon excitation at 447 nm, where both components are excited. In Figure 12 we observe that the resulting spectra exhibit nearly identical features for 447nm and 685nm pump wavelengths. The excited state absorptions at these wavelengths have an almost identical trace.

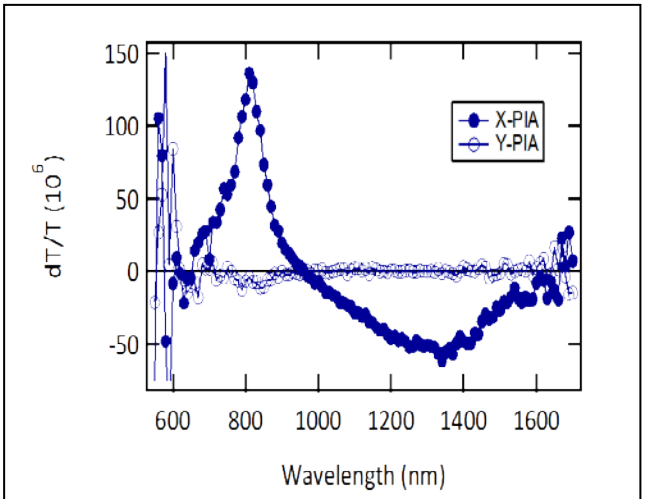

Figure 13. PIA Spectrum of Bi_2S_3:PCPDTBT blend.

The PIA scan of the Bi_2S_3:PCPDTBT blend in Figure 13 shows a polaron generation signal near 1300nm, suggesting that charge transfer occurs between the nanocrystals and the polymer in this blend as well. The peak near 800nm is due to the bleach of the absorption of the materials in the blend before charge transfer occurs and the polaron is generated.

Conclusions

The EQE for each PbS:P3HT device is very similar, although the NH_4SCN device leads to a higher FF and V_{oc}. This could be because it is a very electronegative thiol ligand. The electronegativity could be making it easier for charge to generate at the surface of QDs and for charge transfer to occur. The EQE curves also show contributions for both PbS and P3HT by comparison to absorbance spectra. The PIA signal near 1000nm is evidence of polaron generation in the film. The PIA spectra of PbS:P3HT indicate that CTAB and NH_4SCN ligands help sustain long-lived photoinduced charges. Very little polaron signal is observed in the PIA of MPA-treated and EDT-treated blends. This lack of signal suggests that charge generation between the polymer and nanocrystals in the MPA and EDT treated samples appears to be relatively inefficient or leads to charges with relatively fast recombination dynamics. This could be because the polaron lifetimes are too short for

accurate detection with PIA, or that Forster Resonance Energy Transfer is the mechanism in these devices instead of charge transfer. Future directions of this work will include a photoluminescence excitation study of the P3HT:PbS blends with different ligands to determine whether it functions as a BHJ or a FRET-sensitized Schottky diode. In the absence of the FRET-sensitized process, slower recombination dynamics could possibly explain the enhancements in V_{oc}, FF, and overall device performance observed for the SCN treated P3HT:PbS devices.

The PIA Spectra for Bi_2S_3 shows evidence for charge transfer in blends with both P3HT and PCPDTBT. The blend of P3HT with Bi_2S_3 nanocrystals shows evidence of hole transfer when selectively exciting the Bi_2S_3 component because polaron generation occurs. We believe this means that the charge is still being carried somehow from the Bi_2S_3 to the polymer.

These results suggest that Bi_2S_3 is a compelling material for organic/inorganic hybrid solar cells and device fabrication is presently underway to test this hypothesis.

References

1. Choi, Joshua J.; Lim, Yee-Fun; Santiago-Berrios, M; Oh, M; Hyun, Byung-Ryool; Malliaras, G; Sun, L; Bartnik, A; Goedhart, A; Abruna, H; Wise, F; Hanrath, T. *Nano Lett.*, 2009, 9 (11), 3749-3755

2. Tang, Jiang; Sargent, Edward H. *Adv. Mater.* 2011, 23, 12-29.

3. Noone, Kevin M.; Ginger, David S.; *ACS Nano.,* 2009 3 (2), 261-265

4. Konstantatos et. al. *Adv Energy Mater*. 2011, 1, 1029-1035.

5. Sargent et. al. *ACS Nano*, 2008, 2 (11), 2356-2362

6. Sargent et. al. *Nat. Mater.,* 2011, 765-771

7. Noone, K.M; Anderson, N.C; Horwitz, N.E; Munro, A.M; Kulkarni, A.P; Ginger , D.S. *ACS Nano* 2009, 10, 1345-1352

8. Noone, K.M; Strein, E; Anderson, N.C; Wu, PT; Jenekhe, S.A; Ginger, DS. *Nano Letters* 2010, 2635-2639

9. Heeger et. al. *Sensors* 2010, 10, 6488-6496

10. Liang, C.W.; Su, W.F.; Wang, L. *Appl. Phys. Lett.*, 2010, 95, 133303

11. Sargent et. al. *Nature Photonics*, 2011, 5, 480-484

Acknowledgments

Funds for this research were provided by the Center on Materials and Devices for Information Technology Research (CMDITR), and the NSF Science and Technology Center No. DMR 0120967.

I would like to acknowledge the Hooked on Photonics REU program, CMDITR, and the members of the Ginger lab for their endless help and support especially my mentor, Adam Colbert, labmates Eric Janke and Stephen Hsieh, and Postdoc tutor, Cody Schlenker.

BRITTANI LOVE is a senior chemistry major at Shepherd University in Shepherdstown, WV. She plans to pursue a PhD in physical chemistry.

Determining Charge Transfer Resistance for Organic Photovoltaic Applications

LAURA MURPHY, Pacific Lutheran University
Delvin Tadytin, Brian Zacher, Jeremy Gantz, Dr. Neal Armstrong, University of Arizona

Introduction

Organic photovoltaic cells (OPVs) are a potential solution to the global energy crisis due to their potential for low-cost, efficient production and their unique properties, including light weight and flexibility.[1] The mechanism of charge generation and transport in organic photovoltaic devices has been outlined by Steven Forrest.[2]

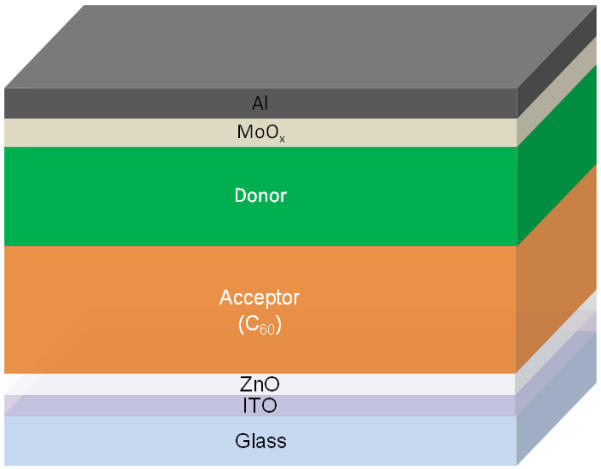

Figure 1. Structure of a bulk heterojunction organic solar cell. Layers include an ITO transparent conducting electrode, a transparent ZnO electron-selective layer, an electron donor/acceptor bulk heterojunction, a MoO_x hole-selective layer, and an Al electrode.

First, a photon is absorbed in the active layer, generating an exciton. Next, the exciton diffuses towards the donor/acceptor interface. At that interface, the exciton dissociates into free charge carriers. Finally, these charge carriers are collected at the electrodes. The internal quantum efficiency is the product of the absorption (η_A), exciton diffusion (η_{ED}), charge transfer (η_{CT}), and charge collection (η_{CC}) efficiencies, as shown in Equation 1.

$$\eta_{IQE} = \eta_A \eta_{ED} \eta_{CT} \eta_{CC}$$

Equation 1.

As a result, if one of these efficiencies is low, the internal quantum efficiency is limited. As the charge collection efficiency is less than 100%, optimizing the charge collection efficiency is an active area of research. This research investigates factors affecting the charge collection resistance, a process taking place at the C_{60}/ZnO interface of inverted OPVs.

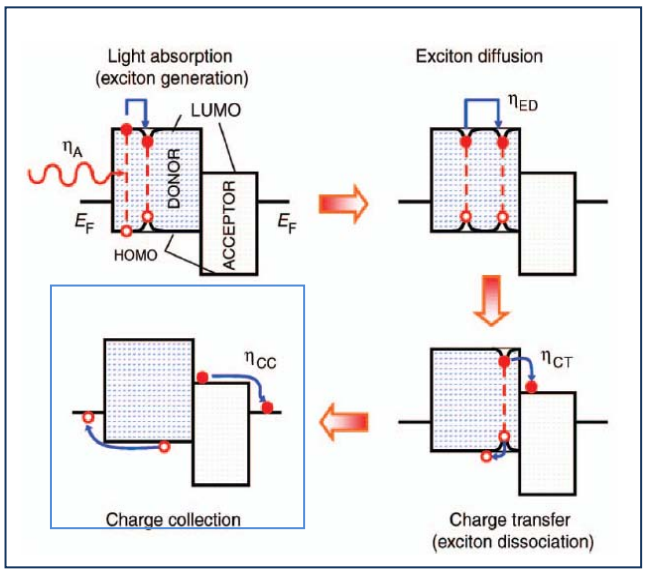

Figure 2. Charge generation and transport mechanism in organic photovoltaics.[2]

As shown in Figure 3, below, several processes affect the internal quantum efficiency. These processes include exciton generation, charge transfer and diffusion, charge trapping, and recombination.

Resistance, caused by charge trapping and recombination, decreases the corresponding efficiency, thus decreasing the overall internal quantum efficiency.

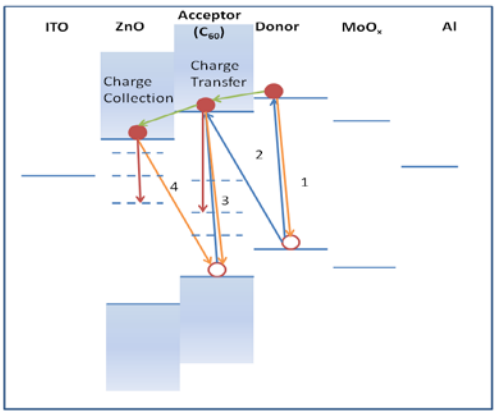

Figure 3. Energetics diagram of an inverted OPV. Blue arrows indicate exciton generation, green arrows represent charge transfer and collection, orange arrows demonstrate recombination, and red arrows indicate charge trapping.

Voltage is the product of current and resistance (Equation 2).

$$\boldsymbol{V = I \times R}$$

Equation 2.

This equation demonstrates that, as resistance increases, current decreases. Furthermore, the power generated by an OPV is the product of the current and the voltage (Equation 3).

$$P = I \times V$$

Equation 3.

As current decreases, power decreases. Thus, an increase in resistance to charge collection decreases the power output of the OPV, as shown in Figure 4.

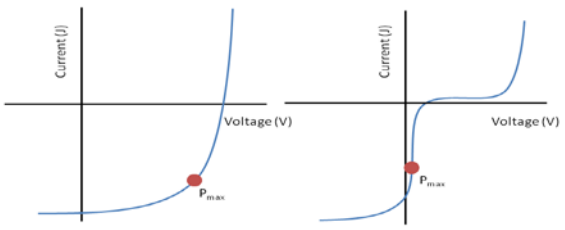

Figure 4. JV curves demonstrating the effect of resistance on the power output of an OPV. The power is the area under the curve. Maximum power is achieved when current and voltage are of the greatest magnitude.

Thus, events such as charge trapping and recombination that increase resistance decrease the power output of OPVs. A study of resistance to each charge generation and transport process is therefore essential to understanding the factors that affect resistance and power output. Such an understanding will enable optimization of solar cell efficiencies. This study focuses on charge collection resistance at the ZnO/C_{60} interface. To facilitate this investigation, an electron-only device, shown in Figure 5, has been devised.

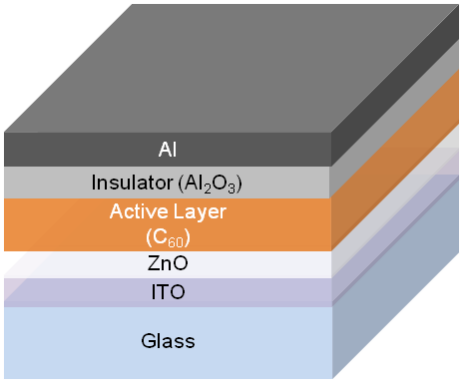

Figure 5. Electron-only device architecture.

This electron-only device consists of six different layers, including a transparent glass substrate coated with a transparent indium tin oxide (ITO) conducting electrode, which serves as the bottom contact. A hole-selective zinc oxide (ZnO) layer above the ITO collects charges into the electrode. Above the ZnO layer is a C_{60} layer, frequently used as an electron acceptor in bulk heterojunction OPVs. On the top of the device, the blocking Al_2O_3 layer prevents charge transport into the low work function aluminum electrode. This device can be described using a resistor-capacitor (RC) circuit analogy, in which the C_{60}/ZnO region demonstrates resistor-like behavior, and the Al/Al_2O_3/C_{60} region will demonstrate capacitor-like behavior, storing up charge on either side of the Al_2O_3 blocking layer (Figure 6).

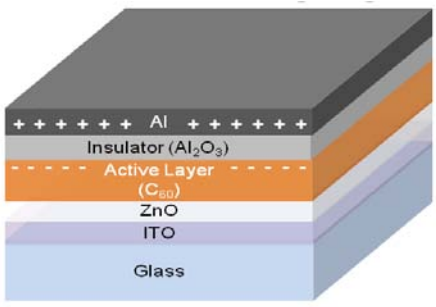

Figure 6. Capacitor-like behavior of Al/Al_2O_3/C_{60} region of electron-only device. Upon pulsing the device with a square wave, charge is stored up on either side of the Al_2O_3 blocking layer.

This electron-only device structure and function can be modeled using an equivalent RC circuit, as shown in Figure 7. The capacitor-like region of the device, shown on the right-hand side of the circuit, will have a capacitance that can be determined using theoretical or experimental calculations.

$$C = \frac{\epsilon_R \epsilon_o A}{d}$$

Equation 4.

Equation 4, above, relates the capacitance of a thin film to its dielectric constant (ϵ_R), area (A), thickness (d), and the vacuum permittivity $\left(\epsilon_o = 8.854 \times 10^{12}\ \frac{F}{m}\right)$.

The resistor-like region of the circuit can be modeled as two resistors in series, the bulk resistance, or resistance to charge transport through the C_{60} active layer, and the charge collection resistance at the C_{60}/ZnO interface (Figure 7).

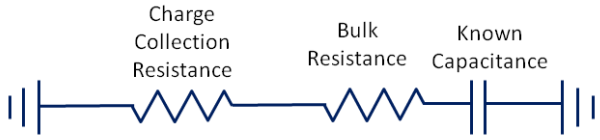

Figure 7. Equivalent circuit for the electron-only device. From left to right: ground; charge collection resistance; bulk resistance; capacitance; and ground.

To determine the total resistance of the device, the capacitor can then be charged up by pulsing the device with a square wave (Figure 8). The voltage will be measured over time using an oscilloscope measuring through channels before and after R_1.

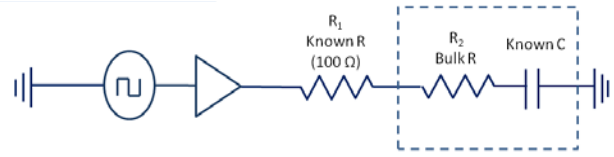

Figure 8. RC time constant testing. First in series is a function generator that will pulse the device with a square wave, then a buffer to amplify the current, a resistor with a known resistance, and the device, represented by the boxed region. The circuit will be grounded on either side.

In this experiment, the device will be pulsed with a square wave, injecting electrons into the ITO layer. These electrons will collect at the C_{60}/Al_2O_3 interface, storing up charge across the insulating layer (Figure 6). Charging up the capacitor will yield voltage versus time data that can be modeled by an equation of the form:

$$V = e^{-\frac{t}{RC}}$$

Equation 1.

From the resulting voltage versus time plot, similar to that shown below, the RC time constant (τ), or time that it takes for the capacitor to charge to 63.2% of its maximum voltage, can be determined.

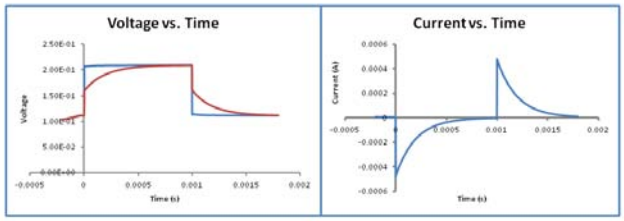

Figure 9. Voltage vs. time data from RC time constant testing on a circuit board.

For example, in Figure 9, a voltage versus time plot (left) from a circuit board is converted to a current vs. time plot (right) by dividing the difference between the voltages before and after the first resistor by its resistance. The resulting current vs. time plot can then be fit with an exponential regression equation, as shown in Figure 10.

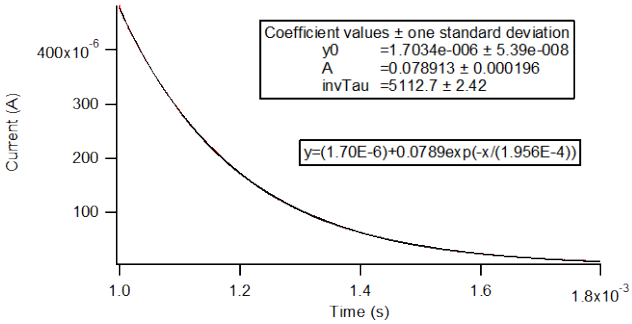

Figure 10. RC time constant determination. The current vs. time data (red) was fit with the the exponential regression equation (black)

$$y = (1.70 \times 10^{-6}) + 0.0789e^{\left(-\frac{x}{1.956 \times 10^{-4}}\right)}.$$

From the exponential regression equation for the current vs. time data, the RC time constant was determined to be $RC = 1.956 \times 10^{-4}$, where R was

100 Ω.

$$RC = 1.956 \times 10^{-4} = (100\ \Omega)C$$
$$R = 96\ \Omega$$

The actual resistance was 100 Ω. This example calculation demonstrates how resistance can be calculated for a device with known capacitance.

The total resistance for each device can then be plotted against the device's active layer thickness (Figure 11). The data can then be fitted with a mathematical model and extrapolated back to zero active layer thickness to determine the charge collection resistance.

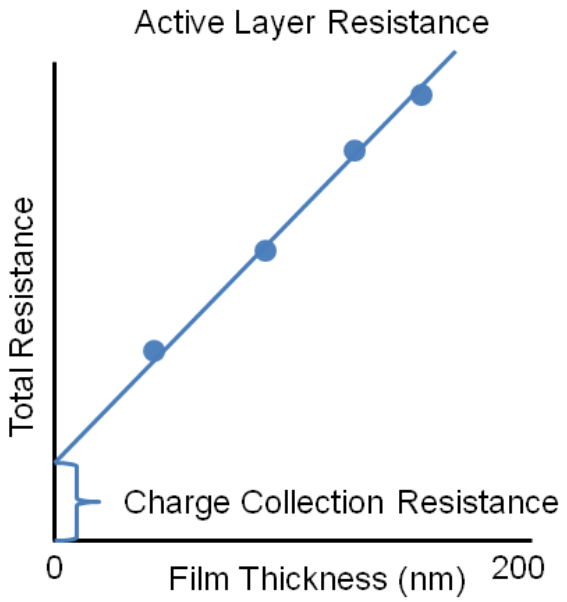

Figure 11. Charge collection resistance determination. In this example graph, resistance is plotted against C_{60} film thickness. The y-intercept of the mathematical model is the charge collection resistance.

This method for determining charge collection resistance at the OPV-relevant C_{60}/ZnO interface is investigated herein.

Experimental Methods

Film Thickness Determination- The thickness of four C_{60} active layers of varying deposition time and the Al_2O_3 dielectric layer were calibrated using atomic force microscopy (AFM) measurements with the Agilent AFM with a long-range scanner in tapping mode.

Substrate Preparation- Glass coated with indium tin oxide (ITO) was ordered from Thin Films Devices. This substrate was cut into one-inch squares and the ITO coating was washed using detergent and solvent. A strip of ITO 0.47 in. wide was masked off with parafilm, and the remaining ITO was etched off in aqua regia (one part nitric acid and three parts hydrochloric acid) for one minute per substrate. The substrates were then washed again using the detergent and solvent method.

Sol-gel Deposition of ZnO- The ZnO precursor for sol-gel deposition was prepared as described by Ohyama, Kozuka, and Yoko.[3] Briefly, 5.438 mmol (0.6768 g) of anhydrous zinc acetate were dissolved in a mixture of 0.235 mL ethanolamine and 3 mL of 2-methoxyethanol. Another 2.3 mL of 2-methoxyethanol were added, and the mixture was heated at 60˚C while stirring at 800 rpm for 30 minutes. The ZnO was then deposited on the etched ITO/glass substrate by spin-coating 200 µL at 2000 rpm for 1 minute with the top and the bottom of the ITO strip masked off. The ZnO film was annealed at 350˚C for 30 minutes.

Active Layer Deposition- The C_{60} active layer was deposited over the same 0.47 in. strip as the ITO using thermal deposition between 350˚C and 450˚ C with a current-controlled heat source. The C_{60} was deposited at a rate between 5 and 6, as monitored by a quartz crystal monitor (QCM). Four such devices were made, with active layer thicknesses of 4.825, 12.068, 18.120, and 24.140, as measured by the QCM.

Blocking Layer Deposition- A 100 nm thick Al_2O_3 blocking layer was deposited using electron beam deposition.

Aluminum Deposition- Aluminum was deposited using thermal deposition from a current-controlled heat source. The device was masked to form six aluminum patches, making six cells. Each cell had dimensions of 0.1406 in. by 0.31493 in.

Current-Voltage (JV) Testing- A device with a C_{60} active layer 200 nm thick over an oxygen plasma-treated ZnO layer was subjected to a voltage gradient from -1 V to 1 V at an increment of 0.005 V with a dwell time of 5 ms. Current was monitored vs. voltage to determine whether the Al_2O_3 layer was blocking.

Al_2O_3 Capacitance Determination- The Al_2O_3 capacitance was determined by pulsing an ITO/Al_2O_3/Al device with a square wave and calculating the RC time constant from the current vs. time data (Brian Zacher, unpublished work).

Results and Discussion

Film thicknesses determined using AFM were plotted against the instrument response. This data was fitted with the linear regression equation $y = 8.73X + 0.46$ with an R^2 value of 0.9995. This

accurate calibration enables determination of film thicknesses around 40 nm to 200 nm based on instrument response during depositon.

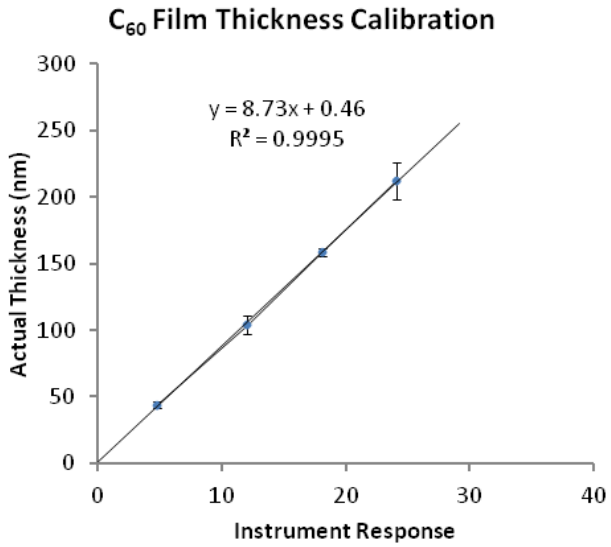

Figure 12. Active layer thickness calibration. Film thicknesses determined by AFM measurements are plotted against instrument response as measured by the QCM during deposition. The equation $\boldsymbol{y = 8.73X + 0.46}$ fits the data with an R^2 value of 0.9995.

Using AFM measurements, the Al_2O_3 thin film was determined to be 100±10 nm thick. Based on this thickness, the Al_2O_3 capacitance was calculated theoretically to be 13.3±0.1 nF as shown below:

$$C = \frac{\epsilon_R \epsilon_o A}{d}$$

Equation 5.

where ε_R is the dielectric constant (9), area A is the area of the cell, d is the thickness of the Al_2O_3 film (100±10 nm), and

$\epsilon_o = 8.854 \times 10^{12} \frac{F}{m}$ is the vacuum permittivity.

$$C = \frac{9\left(8.854 \times 10^{12} \frac{F}{m}\right)(1.72348 \times 10^{-5})}{1.033042 \times 10^{-7}\, m}$$

Equation 6.

$$C = 13.3 \pm 0.1\ nF$$

Equation 7.

Additionally, the Al_2O_3 capacitance was determined experimentally by pulsing an ITO/Al_2O_3/Al device with a square wave and calculating the RC time constant from the current vs. time data shown in Figure 13.

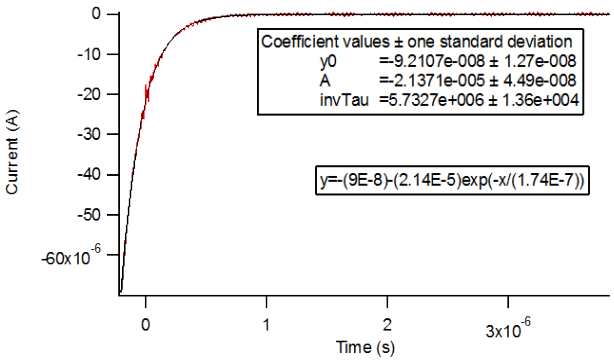

Figure 13. Current vs. time curve (red) for ITO/Al_2O_3/Al device with exponential fit (black)

$$y = -(9 \times 10^{-8}) - (2.1 \times 10^{-6})e^{\left(-\frac{x}{1.74 \times 10^{-7}}\right)}.$$

From the exponential term of this equation, the RC time constant is:

$$RC = 1.74438 \times 10^{-7} = (1000\ \Omega)C$$

Equation 8.

and the capacitance is:

$$C = 0.2\ nF$$

Equation 9.

The discrepancy between the theoretically and experimentally calculated capacitance values could be due to defects in the Al_2O_3 film and over-estimating the cell area. These experiments should be repeated to verify results. Furthermore, thinner films should be used to create better capacitors because capacitance is inversely proportional to film thickness. Additionally, these calculations should be repeated for any other blocking layers tested.

Results of current/ voltage (JV) testing are shown in Figures 14 and 15. Figure 14 shows the JV curve for an attempted electron-only device. The large current densities at both negative and positive voltage biases demonstrate that the device is not a capacitor, but rather a resistor. Thus, this device cannot be charged up and used for RC time constant testing to determine total resistance. Figure 15 shows a plot the JV curve for a blocking electrode for comparison (Jeremy Gantz, unpublished work). Note that current is nearly zero at both negative and positive voltage biases. This indicates that the Al_2O_3 layer is blocking and that second device is a capacitor. Such a device can be used in RC time constant testing to determine interface resistance.

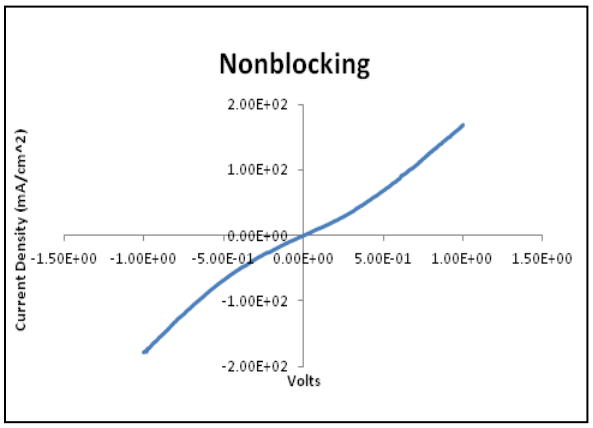

Figure 14. JV curve of device. The device has high current density at both negative and positive voltage biases.

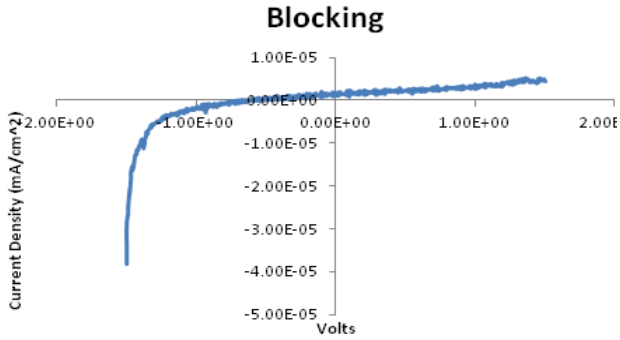

Figure 15. JV curve of blocking electrode. The device has approximately zero current density at both negative and positive voltage biases.

The shorting observed in the intended electron-only device can be explained by a variety of mechanisms. To determine whether tall surface features in the ZnO layer were could be causing shorting, AFM was used to obtain a surface profile. Figure 16, below, shows topographical and height profiles of the ZnO thin film.

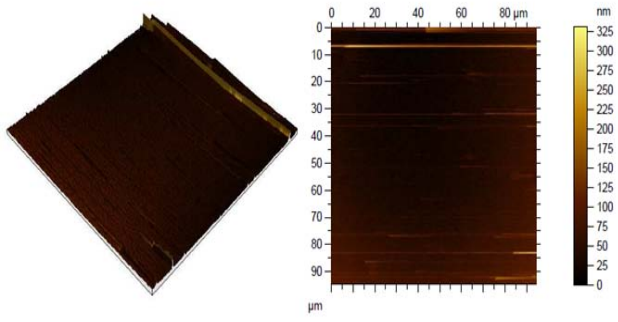

Figure 16. Topographical and height profiles of ZnO surface based on AFM measurements.

As shown in Figure 16, a couple of surface profile features taller than 300 nm appear in the profile. However, one such feature appears along an entire scan line. This could be because the cantilever picked up debris or a ZnO particulate from the surface of the film and dragged it along the remainder of the scan line.

Table 1. Height parameters of ZnO surface from AFM measurement. Sq= root mean square (standard deviation of surface feature heights). Ssk=skewness. Sz= peak height (distance from top of tallest feature to bottom of pit).

Sq	28.5	nm
Ssk	2.16	
Sku	13.2	
Sp	283	nm
Sv	49.0	nm
Sz	332	nm
Sa	20.9	nm

The table above includes a variety of height parameters for the ZnO thin film surface analysis obtained using AFM. Of particular interest are the root mean square (Sq), or the standard deviation of the height of the profile features (28.5 nm), and the maximum profile height, or the distance from the maximum peak to the pit (332 nm). Additionally, the positive skewness (Ssk) indicates that the surface is composed primarily of projections above the plane of the surface. These height parameters indicate that there are tall surface features on the ZnO thin film, which may cause shorting in the device by penetrating through the C_{60}, Al_2O_3, and Al layers. Since the ZnO thin films are so non-uniform, additional surface profile studies should be conducted using more AFM scans to more accurately pinpoint the height outliers.

On the ZnO thin film, tall peaks (hundreds of nanometers) may not be covered by subsequently deposited layers, causing shorting. If uniform ZnO films and functioning electron-only devices cannot be obtained using the sol-gel ZnO deposition method, then sputtering should be used to apply a more even ZnO film.

Additionally, the amount of C_{60} lost from the surface during electron-beam deposition of the Al_2O_3 should be analyzed. Absorbance of the device could be compared to that of a C_{60} thin film of the same thickness, with a ZnO/ITO/Glass substrate as a blank,

to qualitatively study the effects of electron beam deposition on the C_{60} thin film.

Furthermore, different dielectrics, such as SiO_2, SiN, or GaO may be deposited via electron beam deposition at lower temperatures, causing less damage to the active layer. Such dielectrics should be substituted into the proposed electron-only device and tested using JV testing for blocking capability.

Additionally, this experiment should be repeated using these same methods to verify the results. Once the results have been verified or refuted, the electron-only device preparation methods can be optimized. Then, the effects of a variety of ZnO surface treatments, such as light soaking, plasma treatments, and doping ZnO, on charge collection resistance can be tested. For example, devices can be exposed to ultraviolet radiation at 375 nm from a light-emitting diode (LED) for 15 minutes under nitrogen atmosphere as a light-soaking treatment. Also, 15 minute ZnO oxygen plasma treatments can be applied before C_{60} deposition. Then, by fitting the total resistance versus C_{60} film thickness data with a mathematical model and extrapolating back to zero film thickness, the charge collection resistance can be determined for each device. The effects of each surface treatment on charge collection resistance can then be compared, as shown in Figure 17. Oxygen plasma treatments and light soaking are expecting to decrease charge collection resistance.

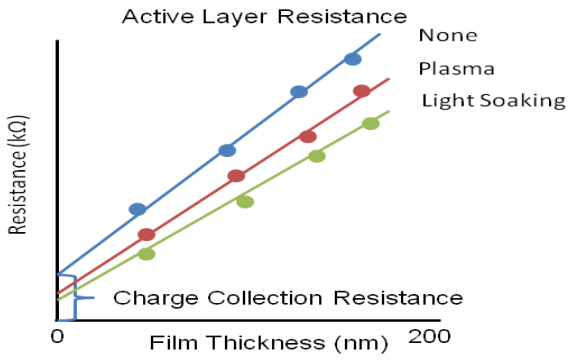

Figure 17. Determination of charge collection resistance at ZnO/C_{60} interface for various surface treatments.

Conclusions

In conclusion, this investigation calibrated C_{60} and Al_2O_3 film thicknesses for future determination of the charge collection resistance at the OPV-relevant ZnO/C_{60} interface. Additionally, the capacitance of the 100±10 nm Al_2O_3 layer was calculated theoretically to be 13.3±0.1 nF and experimentally to be 0.2 nF. This test should be repeated for more accurate capacitance determination. JV testing demonstrated that the Al_2O_3 layer was not blocking, and AFM data indicated that tall ZnO surface features may be causing shorting in the device. Future work will include repeating these experiments, optimizing the electron-only device for this research, and testing the effects of various ZnO surface treatments on the charge collection resistance.

References

1. Hoppe, H.; Sariciftci, N. S. *J. Mater. Res.* 2004, 19, 1924-1945.

2. Forrest, S. R. *Mater. Res. Bull.* 2005, *30*, 28-32.

3. Ohyama, M.; Kozuka, H.; Yoko, T. *Thin Solid Films.* 1997, *306*, 78-85.

Acknowledgments

Funds for this research were provided by the Center on Materials and Devices for Information Technology Research (CMDITR), and the NSF Science and Technology Center No. DMR 0120967.

Additional thanks to program coordinators Kimberly Sierra-Cajas, Trin Riojas, and Amanda Anderson, as well as Lessa and Keck facility managers Paul Lee and Dr. Brooke Beam.

Laura Murphy is a chemistry and physics undergraduate student at Pacific Lutheran University. She plans to earn a PhD in analytical chemistry and pursue a career in industry researching and designing photovoltaic devices.

Amino Acids and Pesticides in the Synthesis of Crystalline Optical Materials

VIKTORIA V. PAKHNYUK, University of Washington
Delwin L. Elder, Werner Kaminsky, University of Washington

Introduction

In pursuing the goal to derive optical properties using the vast pool of X-ray structures for the design of materials with large electro-optic effects, we continued previous undergraduate research into the synthesis of new chiral compounds and characterization of their optical properties. From studying a series of closely structurally related materials we tracked how changes in composition affected the associated optical properties. These new compounds are products of simple amino acids and aryl isothiocyanates (ITC). The chirality of the amino acids ensures the creation of products that are non-centrosymmetric, a required characteristic for non-linear optical behavior.

Previously, we observed that crystallization of the product involved dimerization through selected hydrogen bonding between the nitrogen of the ITC and the sulfur of a next neighbor and vice versa. Determining the chiral hand of the molecules with X-rays is possible when heavy atoms, here sulfur, are present in the products' structures.

Observations within this series of compounds may be used to design related compounds with large non-linear optical properties for applications such as telecommunications.

Experimental Methods

ITCs with varying withdrawing groups such as NO_2, OCH_3, and Cl, have been crystallized successfully before with chiral reagents including (S)-2-butanol and (S)-α-methylbenzylamine [1].

Here, we reacted racemic and enantiopure amino acids alanine and valine with ITCs, which have a nitro group in the para- position, to form products shown in Scheme 1.

After product reaction and purification, Electrospray Ionization Mass Spectrometry (ESI/MS) and Nuclear Magnetic Resonance (NMR) was used to determine if the desired product was formed.

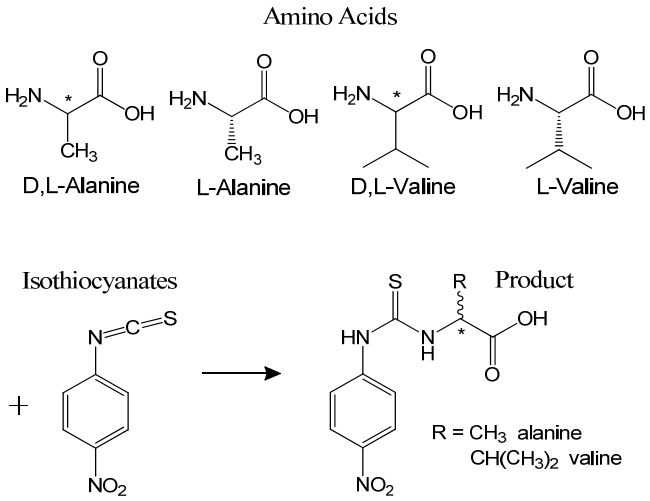

Scheme 1. Schematic of experimental reactions of enantiopure and racemic alanine and valine with 4-nitrophenyl isothiocyanate

Following recrystallization, a single crystal was provided for X-ray diffraction, where the scattering of an x-ray beam in different orientations is used to find the positions of atoms in the sample. Calculations of refractive indices, optical rotation, and other non-linear optical properties were done on the basis of these structures.

Reaction 1 Procedure

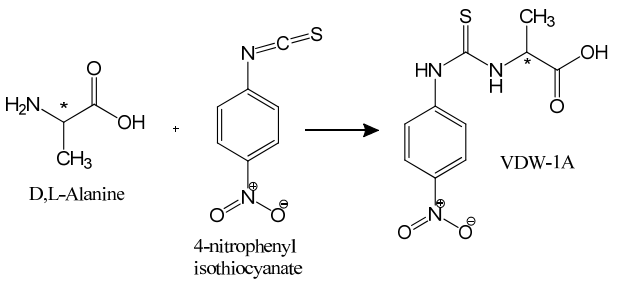

Scheme 2. Reactions of racemic alanine with 4-nitrophenyl isothiocyanate

First, 0.506g (0.00568 mol) of D,L-alanine and 0.404g (0.00280 mol) of 4-nitrophenyl ITC were

weighed, and then added to a solvent of 15mL methanol, 15mL deionized (DI) water, and 25mL tetrahydrofuran (THF), in which the solids were partially soluble. To dissolve the starting materials, 0.300g (0.00750 mol) of sodium hydroxide was added [2,3]. The reagents dissolved while the base was stirred into solution, turning the liquid from a cloudy light yellow to orange to a clear red color. The mixture was stirred overnight at room temperature.

Thin-layer chromatography was done the following day (1:1:1 methanol: ethyl acetate: hexane) in comparison to the starting materials. A ninhydrin stain was used to color the amino acid for visibility. TLC showed the reaction was complete and the liquid was neutralized to pH 7 with hydrochloric acid. The solution turned from bright red to orange to yellow with the addition of acid. This mixture was placed on the rotary evaporator to remove the volatile solvents (30°C water bath), which resulted in precipitation to a cloudy yellow mixture. The remaining aqueous solution was acidified to pH 2 with hydrochloric acid, and extractions were performed with 3x40mL rinses of ethyl acetate. The organic layer was dried with anhydrous magnesium sulfate and filtered through a glass frit funnel. The solvent was removed with rotary evaporation (rotavap). The dried unpurified product resembled a thick yellow oil before cooling, and later solidified to an orange-yellow solid.

The product was purified with silica gel column chromatography eluted in 1:1:1 methanol: ethyl acetate: hexane (1.25” D, 12” L). The product was loaded onto the column in ethyl acetate. After TLC analysis of column fractions, the impure product in the initial test tubes was combined for purification on a second column which used 1:2:2 methanol: ethyl acetate: hexane as solvent (0.75” D, 12” L). Fractions with the pure product were combined and put on the rotavap in a weighed roundbottom flask. Afterward, the product was dried in the vacuum oven overnight at 70°C.

The dried, purified product was weighed and characterized. The product was fluffy, crispy and foam-like in an orange color. The product was split into 5x4mL vials and dissolved in 5 solvents (1:4 methanol: ethanol, 1:1 methanol: ethanol, 1:1 dichloromethane (DCM): methanol, acetonitrile, THF, and acetone) for crystallization with fast evaporation (uncapped at room temperature). Acetone and THF vials left a syrup-like substance and were left to crystallize slowly, while others produced a dried, powder-like substance.

Reaction 2 Procedure

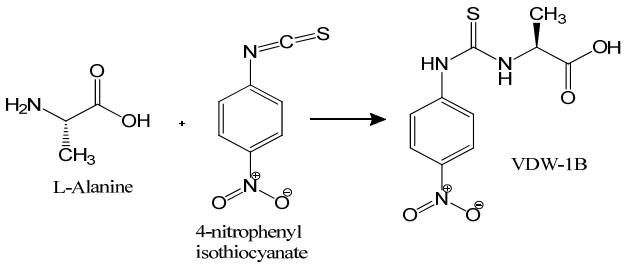

Scheme 3. Reactions of enantiopure alanine with 4-nitrophenyl isothiocyanate

Reaction 2 follows procedure 1 with 0.505g (0.00567 mol) L-alanine and 0.505g (0.00280 mol) 4-nitrophenyl ITC with a reaction solvent of 15mL DI water and 25mL THF. For solubility, 0.229g (0.00573 mol) of sodium hydroxide was added [2,3].

The silica gel column was run in 1:2:2 methanol: ethyl acetate: hexane (1.25” D, 12” L). Impure fractions were purified in a second column of the same solvent (0.75” D, 12” L). The product was run by gravity half-way through the column. The vacuum oven temperature was higher than desired at 100°C.

The dried, purified product was attempted for crystallization in 9 solvents (2:1 methanol: ethanol, 9:1 methanol: ethanol, 1:1 methanol: ethanol, 1:1 acetone: ethanol, 1:1 DCM: methanol, 2:1 methanol: THF, acetone, THF and acetonitrile) but fast evaporation did not produce a crystal-like product after drying. Recrystallization was repeated with slow evaporation, covering vials in parafilm with a needle-sized hole at room temperature, but similar results were achieved.

Reaction 3 Procedure

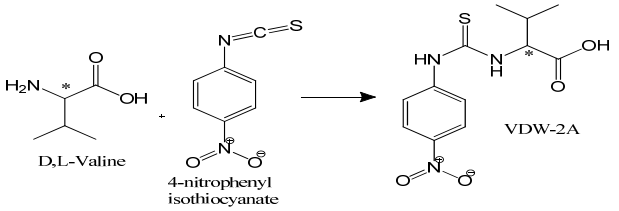

Scheme 4. Reactions of racemic valanine with 4-nitrophenyl isothiocyanate

Reaction 3 follows procedure 1 with 0.565g (0.00482 mol) D,L-valine and 0.433g (0.00240 mol) 4-nitrophenyl ITC in 15mL DI water, 25mL THF and 0.192g (0.00482 mol) sodium hydroxide [2,3]. This mixture stirred overnight in a reflux setup with an oil bath of 75-80°C under low nitrogen pressure.

In an attempt to increase separation, silica gel column chromatography was done by the dry loading method (~10mL silica gel added to drying product) and was prepared in 1:1 ethyl acetate: hexane. The column was run by increasing the methanol content by 5% for every 200mL added to the column. The vacuum oven temperature was 60°C.

Crystallization was attempted in 5 solvents (THF, 1:1 DCM: methanol, acetone, methanol, 3:2 acetonitrile: THF). Methanol and 1:1 DCM: methanol left rigid crystals and were recrystallized with slow evaporation. 1:1 DCM: methanol x-ray characterization showed the making of a new successful product.

Reaction 4 Procedure

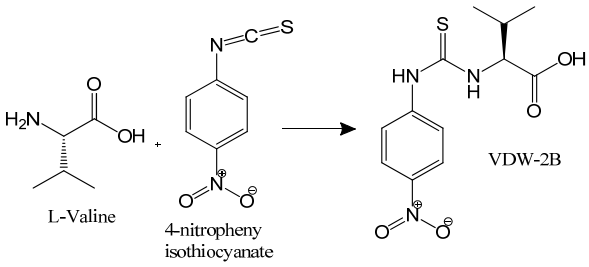

Scheme 5: Reactions of enantiopure alanine with 4-nitrophenyl isothiocyanate

Reaction 4 follows procedure 3 with 0.565g (0.00482 mol) L-valine and 0.428g (0.00238 mol) 4-nitrophenyl ITC in 15mL DI water, 25mL THF and 0.229g (0.005873 mol) sodium hydroxide [2,3].

Column chromatography was run in 1:2:2 methanol: ethyl acetate: hexane solvent (1.25" D, 12" L) by gravity until product fractions were collected.

The product was left for crystallization in 5 solvents (acetonitrile, acetone, THF, methanol, 1:1 DCM: methanol). 1:1 DCM: methanol showed the most appropriate crystals, but not adequate for x-ray measurement. The sample was recrystallized in toluene, gradually decreasing temperature in a refrigerator, then freezer, then to dry ice in acetone at -30-40°C, but samples redissolved before x-ray measurement.

Results and Discussion

Characterization of the product was done using ESI/MS, NMR and x-ray diffraction. Mass spectroscopy (Figures 1 – 4) shows that both racemic and enantiopure alanine and valine reacted successfully into the desired product.

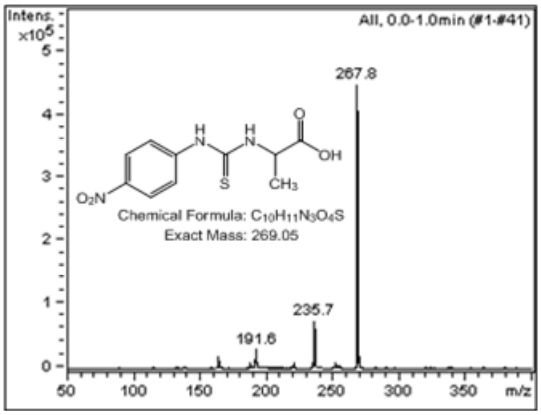

Figure 1. Mass Spectroscopy of VDW-1A

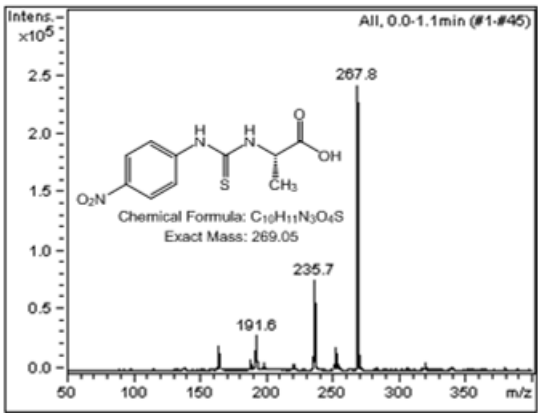

Figure 2. Mass Spectroscopy of VDW-1B

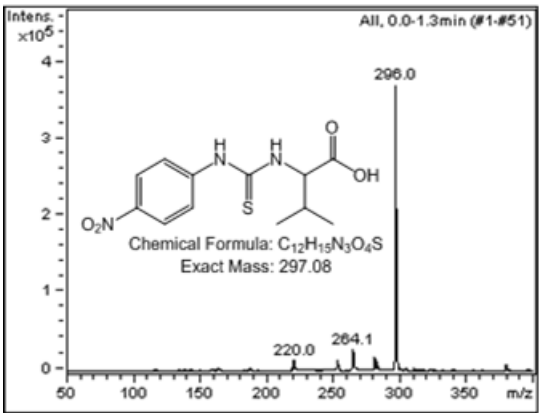

Figure 3. Mass Spectroscopy of VDW-2A

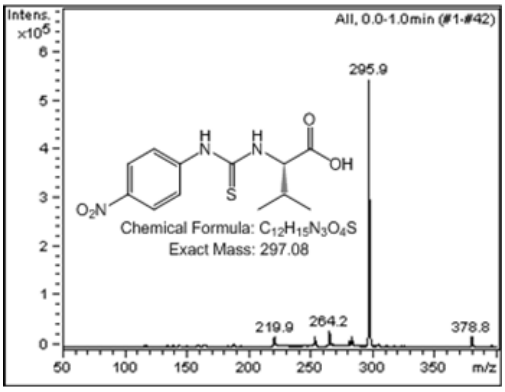

Figure 4. Mass Spectroscopy of VDW-2

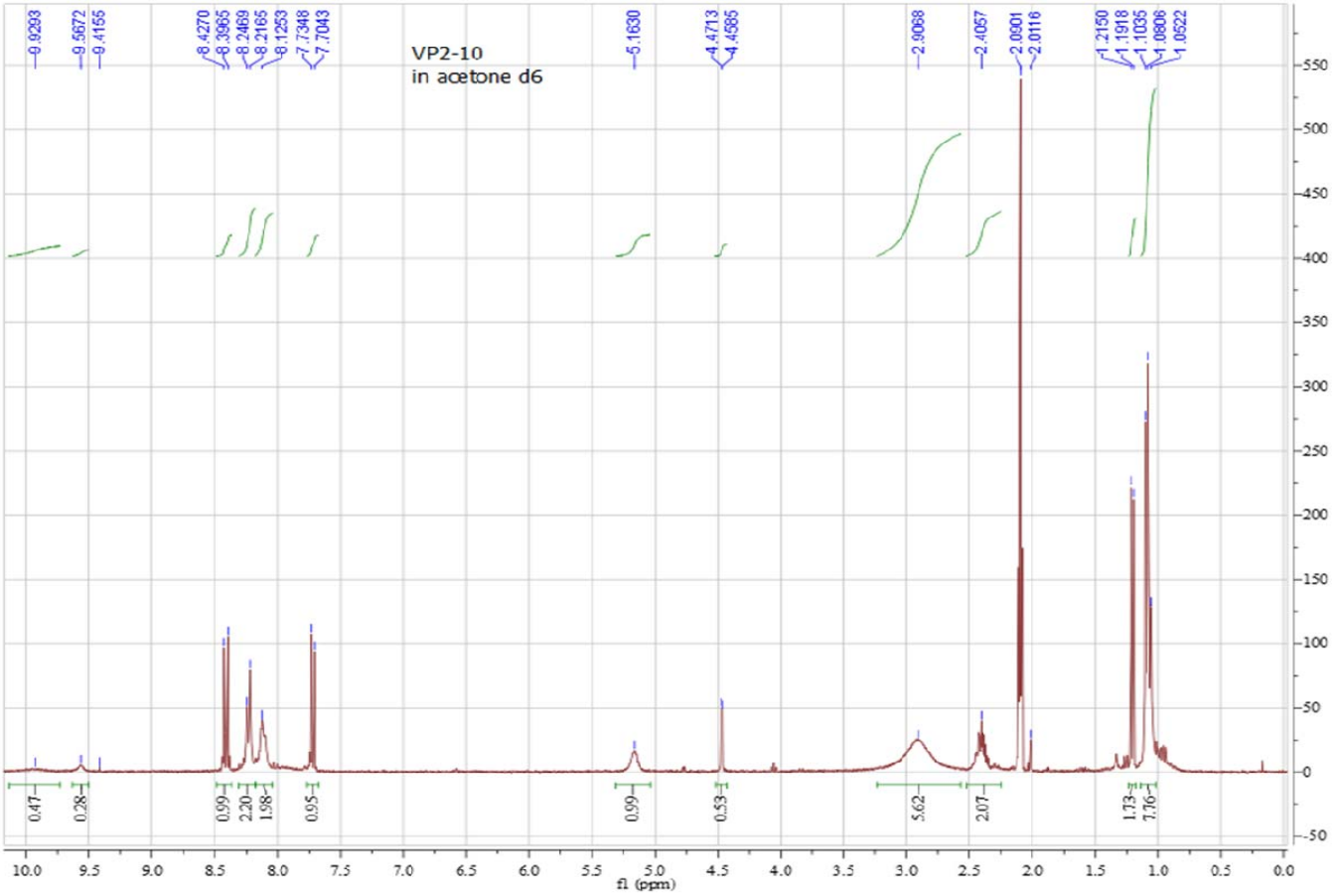

Figure 5. NMR spectrum of products from Scheme 4

Nuclear Magnetic Resonance and X-ray diffraction shows that side products were also present, which made NMR spectra difficult to decipher (Figure 5). X-ray diffraction was able to successfully measure a structure for the reaction of DL-valine and 4-nitrophneyl ITC (Figure 6).

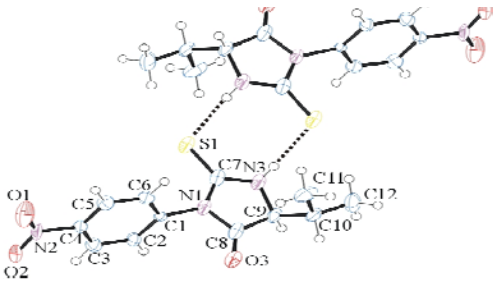

Figure 6. X-ray structure with intermolecular bonding of new DL-valine + 4-nitrophenyl ITC product (not VDW-2A)

The newly formed five-membered ring in the structure differs from the expected product and disagrees with mass spectroscopy. It is possible that the major product gradually dehydrated into this structure while contributing to NMR signals as impurity following the mechanism depicted in scheme 6.

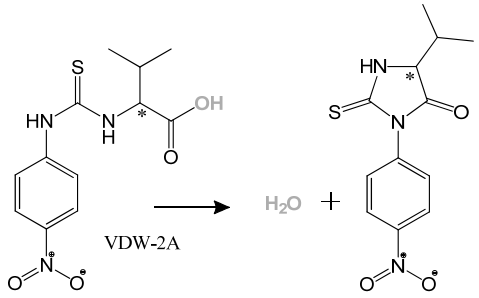

Scheme 6. Dehydration mechanism of VDW-2A

It should be mentioned that some enantiopure crystals formed during purification of VDW-2B directly in test tubes (Figure 7),

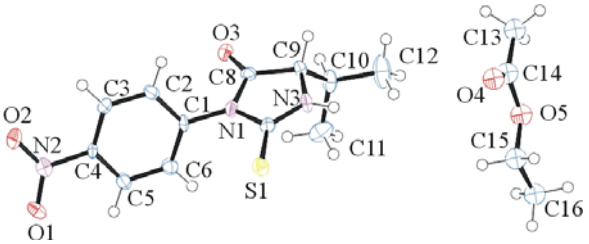

Figure 7. X-ray structure with intermolecular bonding of new L-valine + 4-nitrophenyl ITC product (not VDW-2B)

containing solvent which do not form the expected dimer and are thus structurally not closely related to the series of compounds under investigation.

The attempts for crystallization in other solvents and for other reactions did not result in crystals suitable for measurement.

Crystals of VDW-2A were twinned via a 180 degree rotation about the a-axis (Figure 8).

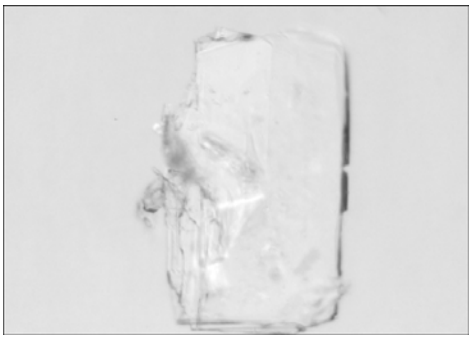

Figure 8. Twinning of crystals formed by reaction of 4-nitrophenyl ITC and DL-valine

Tensor calculations were made and electro-optic effects were predicted utilizing a dipole-dipole interaction model software which calculates refractive indices and optical rotation of linerar polarized light pasing the sample. In repeating these calculations with structures distorted through atom polarization in a hypothetical external electric field one can derive higher optical effects.

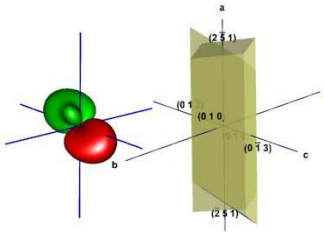

Figure 9. DL-valine + 4-nitrophenyl isothiocyanate. Representation surface of the quadratic electro-optic effect and crystal morphology

A Taylor expansion of the optical dielectric tensor (ε) as derived from our model shows how the difference of ε for structures with electric field applied to the structure without field is unfolded into different contributions.

$$\varepsilon(E) = \varepsilon_o + \frac{\partial \varepsilon}{\partial E}E + \frac{1}{2}\frac{\partial^2 \varepsilon}{\partial E^2}E^2 = \varepsilon_o + \frac{\partial \varepsilon}{\partial E}E + \frac{1}{2}\frac{\partial}{\partial E}\left(\frac{\partial \varepsilon}{\partial E}E\right)E$$

The following two graphs compare the theoretical electro-optic effect of the molecule in Figure 6 to a molecule formed previously with the reaction of 4-nitrophenyl ITC and (S)-α-methylbenzyl amine.

The property plotted is (ε(**E**)- ε(0)) / **E** with **E** in different directions, which results in a 3x3x3 matrix. The change of this electro-optic effect is plotted below as the electric field increases to high strengths (not realistically measureable in a laboratory). The linear slope of the plotted values relate to the third term in the Taylor expansion, the quadratic electro-optic effect, which is present in crystals of any symmetry.

The linear electro-optic effect (second term) does not exist for racemic molecules because of their symmetry, with values crossing the origin.

The values plotted in Figure 10 do not begin at zero because the linear electro-optic effect does exist in this chiral non-centrosymmetric material.

These graphs show that the new compound reacted from DL-valine shows slightly higher quadratic electo-optic features as the slopes are

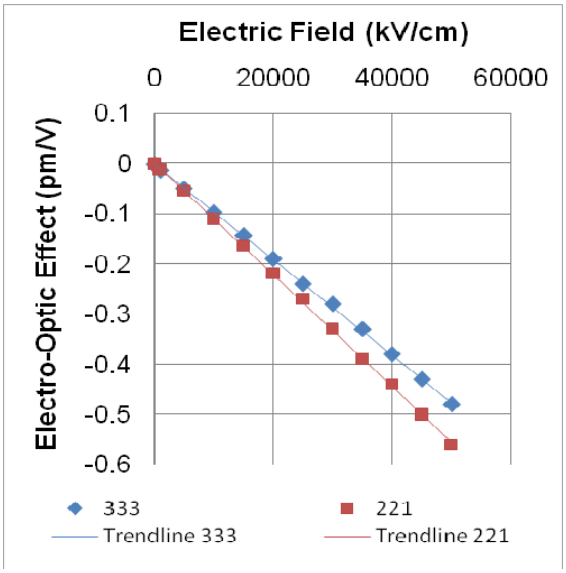

Figure 10: The change in electro-optic effect of racemic DL-valine + 4-nitrophenyl ITC in an increasing electric field

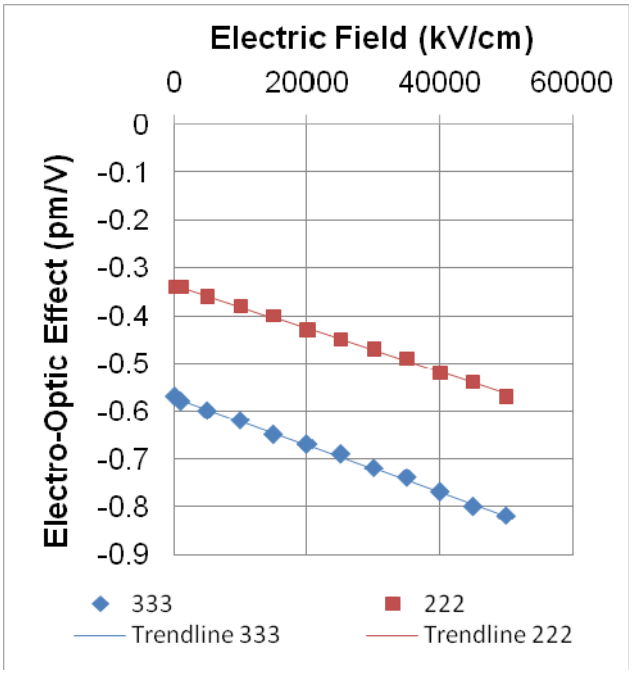

Figure 11: The change in electro-optic effect of S-α-methylbenzylamine + 4-nitrophenyl ITC in an increasing electric field

steeper. However, we yet have to test if there is a general correlation between the linear and quadratic electro-optic effects which would be very useful to find promising materials. We still hope to crystallize L-valine for calculating its linear electro-optic effect for this purpose.

Finally, Figure 12 below shows an experimental optical representation of refractive indices of VDW-2A, (010) face, which could serve to find calculation parameters to be explored in future work.

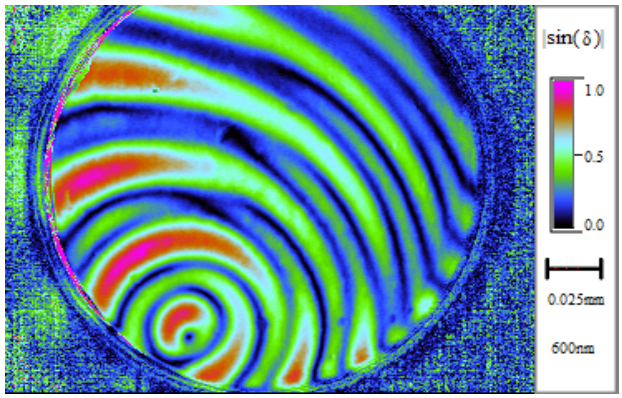

Figure 12: Microscopic conoscopic image of the product of DL-valine + 4-nitrophenyl ITC along (010), showing one of two optic axes of the compound.

Conclusions

We succeeded in adding a new series of synthesized compounds by replacing 2-butanol and α-methyl-benzylamine [2] with D,L-valine.

Further attempts will include finding solvent-free enantiopure crystals which exhibit non-linear optical properties due to the absence of inversion symmetry.

Recrystallization, X-ray structure determinations, and model calculations on enantiopure chiral compounds are still under way as well as a more thorough comparison of quadratic electro-optic properties with this compound family.

References

1. Kaminsky, W., Responte, D., Daranciang, D., Gallegos, J. B., Tran, B-C. N., Pham, T-A. (2010). Structure, Morphology and Optical Properties of Chiral N-(4-Xphenyl)-N-[1(S)-1-phenylethyl]thiourea, X= Cl, Br, and NO_2. *Molecules,* 15, 554-569.
2. Dydio, P., and C.Rubay , T. Gadzikwa , M. Lutz , J. Reek. (2011). "Cofactor"-controlled enantioselective catalysis. *Journal of the American Chemical Society,* 133, S32-S33.
3. Zhao-Bo, L., and L. Shu-Ping, X. Ai-Bao, X. Dan-Qian. (2010). The highly enantioselective Michael addition of ketones to nitrodienes catalyzed by the efficient organocatalyst system of purrolidinyl-thiomidazole and chiral thioureido acid. *Organic and Biomolecular Chemistry*, 8, 2505-2508.

Acknowledgments

Funds for this research were provided by the Center on Materials and Devices for Information Technology Research (CMDITR), and the NSF Science and Technology Center No. DMR 0120967. Special thanks to the Dalton Lab, Max Kaganyuk, and Dr. Sei-Hum Jang at the University of Washington.

Viktoria Pakhnyuk is pursuing a Bachelor of Science degree in Chemistry and considers graduate school to continue studying chemistry.

Hydrogel Photonic Crystals: Improving Organic Solar Cell Efficiencies through Tunable Up-conversion

CANDICE PORTER, The University of Arizona
Ji-Hwan Kang, Elsa Reichmanis Georgia Institute of Technology

Introduction

Since the mid 1950's the United States has been investigating harvesting energy from the sun in order to power the world through a clean, and renewable energy source. New technologies in organic solar cells have the potential to revolutionize the electronics world, being extremely light weight and flexible. But with this novel idea come its problems. The most prominent of these problems is that solar cells have a thermodynamic efficiency limitation. Currently, organic solar cells have an efficiency that tops out at about ten percent, which has been considered as a minimum point for its commercialization. However, this efficiency limit is a result of the fact that solar cells are limited to a specific range of photons that they can harvest due to the band gap that they possess. Many times light over the near infrared region in the electromagnetic spectrum is completely lost to a solar cell, and the energy that it contains cannot be harvested at all. Herein, the project aims to address this problem by synthesizing a hydrogel photonic crystal with a tunable optical band gap, and then through a technique called up-conversion it may be possible to harness inferior solar photons.

Hydrogels have been in use for many years in many different fields.[1] Hydrogels have many uses from medical applications, to cooking, to agriculture. A hydrogel is an amorphous solid that has the ability to hold water up to many times its weight. This is because of the way the hydrogel is composed. Long polymer chains trap water inside of the gel, holding in moisture. Because of this property hydrogels are used in commercial products such as diapers and contact lenses. Employing the hydrogel medium for a colloidal photonic crystal will allow optimization of its optical band gap by controlling the hydrogel volume with the pH of the environment. Depending on the swelling-deswelling properties of the hydrogel, different upconverted emission light can be generated and tuned effectively use of the inferior solar spectrum as an excitation source for TTA (triplet triplet annihilation) -upconversion.

Experimental Methods

Chemicals and Materials:

All chemicals were purchased from Aldrich and used as they were received. Reactions were done in a fume hood.

As shown in Figure 1, silica nanoparticles were first synthesized by a process set out by Stober[1]. This is a method in which alkyl silicates are hydrolyzed, and then condensation of silicic acid in an alcohol solution will take place.[2-3] Two solutions were prepared separately; solution A containing 72 mL ethanol, 9 mL deionized water, and 3.5 mL ammonium hydroxide and solution B containing 28 mL ethanol and Tetraethyl orthosilicate (TEOS). Both were stirred at 300rpm for 20 minutes and then combined and stirred for 2 hours at 300rpm.

The synthetic product was washed two times with pure ethanol to remove excess chemicals and byproducts. In between each wash, the ethanol/product mixture was centrifuged at 6000rpm for 20 minutes and the ethanol was decanted. For this particular synthesis, ammonium hydroxide was used as a catalyst. This is a morphological catalyst and works by providing the particles with a negative charge. Different reaction parameters were explored in order to perfect the size of the silica particles. TEOS concentration was altered along with the concentration of ammonium hydroxide. As more TEOS was added, the particles grew larger, leading to a change in the color of refracted light from green to red. With less TEOS, the synthesis yielded particles having blue-shifted optical bandgaps through smaller lattice constants.

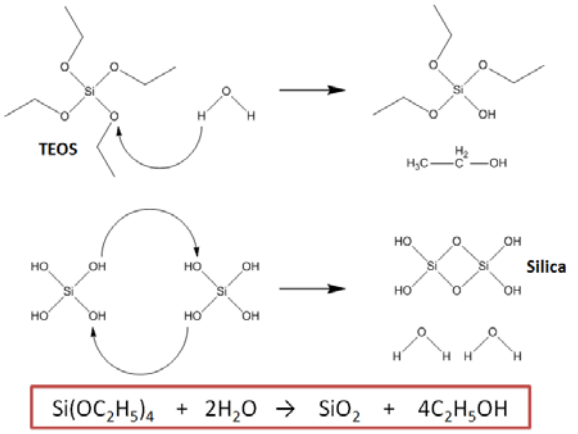

Figure 1. Synthetic pathway for the preparation of silica nanoparticles.

A seeded growth method was used in order to achieve high monodispersity of silica particles.[4] The sequential synthetic steps start by first growing silica seeds. For stabilization of small monodisperse silica particles, 0.06 grams *L*-arginine was used as a base catalyst for the hydrolysis. To slow TEOS release into the reaction, cyclohexane was added to form an immiscible organic layer on the aqueous phase and the mixture was heated to 60 °C under constant stirring at 300 rpm. TEOS was then added to the mixture which was then stirred at a constant temperature for 20 hours. Seeds were decanted from the organic layer and stored for use in further re-growth.

In the regrowth of the silica seeds for a desired size, the suspension of seeds from the first step was stirred while heating until the temperature reached 60 °C and TEOS was then added. In a typical regrowth reaction, 1ml of 25nm silica seeds was gently dispersed in aqueous solution containing 2.5mmol monomer. The reaction proceeded for 30 hours. To minimize secondary doublet formation, seeds were regrown this way twice until reaching a particle size of 120nm.[4]

After less than 100nm-sized regrown seeds were prepared, the particles were regrown via the Stober method described above, using different monomer concentrations to make the desired sized particles. The mixture was stirred at 340 rpm while TEOS was added at a rate of 0.5mL/hr. After the reaction was complete the silica nanoparticles were washed with 10 mL of ethanol, sonicated until they were evenly dispersed in the solution, and centrifuged at 6000 rpm for 40 minutes. Particles were washed twice using the procedure described earlier.

Characterization

Final products were characterized by scanning electron microscopy (SEM).

Results and Discussion

In comparison to seeded growth, direct synthesis by the Stober method yielded silica nanoparticles which appear to have low monodispersity. Figure 2 shows an SEM image of particles synthesized by the Stober method. As shown in the image, the particles are of two distinctly different sizes and are highly polydisperse.

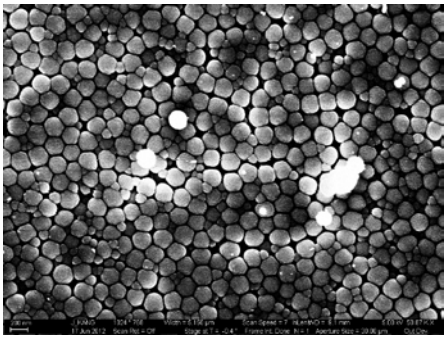

Figure 2. Silica nanoparticles synthesized by the standard Stober method.

Particles Synthesized by Seeded Growth:

Synthesis by seeded growth yielded very monodisperse small (<100nm) particles. SEM images obtained for each step in the synthesis described above can be seen in Figures 3, 4, and 5.

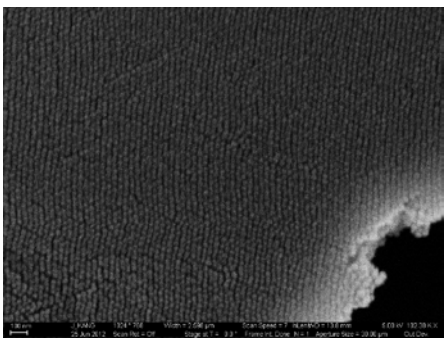

Figure 3. Silica nanoparticles obtained from the first step of the seeded growth method. Particle size is <30nm.

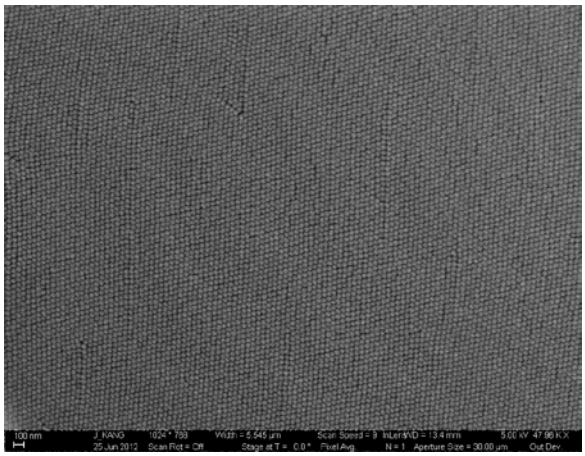

Figure 4. Silica nanoparticles obtained from regrowth. Particle size is <50nm.

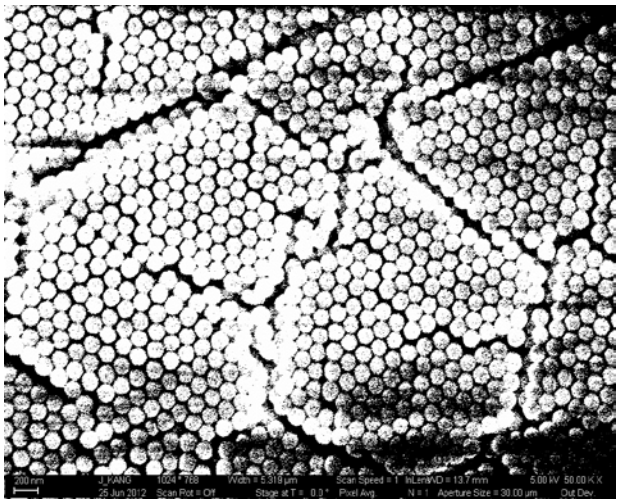

Figure 5. Silica particles after a sequence of two regrowth procedures and further regrown by the Stober method. Particle size is <200nm.

Exploration of Reaction Parameters:

For both the classical Stober synthetic method and the seeded growth process, different reaction parameters were investigated to determine the best conditions leading to controlled silica particle size. The first parameter explored was the effect of changing the TEOS concentration. Results showed that as the concentration of TEOS was increased, the nanoparticles grew in size. These results can be seen in Table1. Changing the concentration of ammonium hydroxide (the catalyst in the reaction) was also evaluated as a way to increase particle size. As more ammonium hydroxide was added, the particle size did indeed increase. However, increased ammonium hydroxide concentration also increases polydispersity, which might be undesirable for the intended application.

TEOS (mM)	NH_4OH (mM)	Color	Estimated diameter (nm)
3.7	10.9	Green	270
3.7	10.9	Green	265
4.8	10.9	Green	275
4.8	10.9	Red	325
1.3	10.9	Blue	220
4.9	10.9	Blue	215
2.2	10.9	Green	275
4.8	10.9	Red	345
2.2	9.3	blue	210
2.2	12.4	white	200
2.2	6.2	white	200
2.2	7.7	Blue	220

Table 1. Refractive color control dependent on concentration of monomer and catalysis for Stober method reaction.

The optical bandgaps of the silica particles were estimated by using Bragg's equation, (where Φ is equal to the volume fraction of the FCC crystal lattice (0.74), n_p is equal to the refractive index of air 1, and n_m is equal to the refactive index of silicon, 1.45) assuming that the particles were organized in a FCC crystal lattice;

$$\lambda = 2dn_{eff} = \left(\frac{8}{3}\right)^{1/2}\left(\frac{\pi}{3\sqrt{2\phi}}\right)^{1/3} D\left(n_p{}^2\phi + n_m{}^2\left(1-\phi\right)\right)^{1/2}$$

Future Work

The silica particles prepared and characterized above will be incorporated into the pH-sensitive 2-hydroxyethyl methacrylate (HEMA)-based hydrogel photonic crystal, which can be fabricated by photo-induced polymerization of the silica-dispersed resin. The hydrogel volume will be controlled through immersion in differing pH buffer solutions. As the pH of the buffer increases the hydrogel is expected to swell, and with a decrease in pH it will shrink in volume. Figure 6 shows a representation of silica nanoparticles before and after coating with a hydrogel.

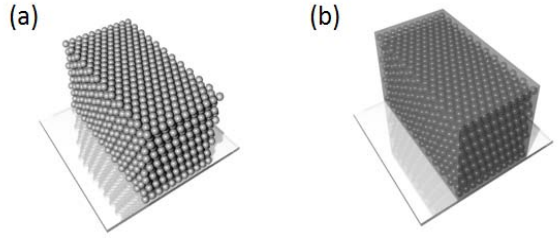

Figure 6. Schematic illustration of (a) silica nanoparticle film and (b) silica hydrogel composite.

By manipulating interspacing distance between particles in the face centered cubic (FCC) structure, the wavelength of light emitted from the structure can be tuned. This emitted light will then be utilized for TTA based up-conversion as shown in Figure 7, which is a process where one single photon with higher energy can be generated from two photons of lower energy. This process functions even using a non-coherent light source.

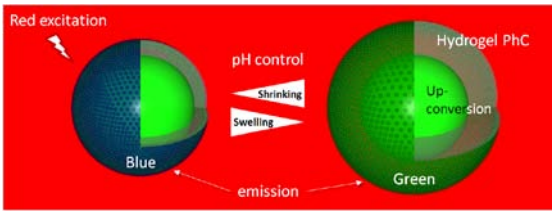

Figure 7. Schematic illustration of pH-sensitive upconverting hydrogel photonic crystals

In particular, TTA-upconversion can directly use sunlight as an excitation source. The constructively enhanced emission from photon upconversion via the shell layer of refracting mirror may improve the power conversion efficiency of a solar cell by exploiting readily available solar photons that would otherwise go unused.

Conclusions

Highly monodisperse silica particles were synthesized via a seeded growth process. Further work with hydrogel and TTA up-conversion will be explored in the future in order to harvest inferior solar photons.

References

1. Ajayaghosh, A., Praveen, V.K. & Vijayakumar, C., "Organogels as scaffolds for excitation energy transfer and light harvesting," *Chem Soc Rev* 37, 109-22(2008).

2. Stober, Werner, Arthur Fink, and Ernst Bohn, "Controlled Growth of Monodisperse Silica Spheres in the Micron Size Range," *Journal of Colloid and Interface Science* 26. (1968): 62-69.

3. Van Blaaderen, A, A, Van Geest, and A. Vrij., "Monodisperse Colloidal Silica Spheres from Tetraalkoxysilanes: Particle Formation and Growth Mechanism," *Journal of Colloid and Interface Science* 154.2 (1992): 481-501.

4. Hartlen, Kurtis D, Aristidis P. T., Athanasopoulos, Vladimir Kitaev, "Facile Preparation of Highly Monodisperse Small Silica Spheres (15 to >200 nm) Suitable for Colloidal Templating and Formation of Ordered Arrays," *Journal of American Chemical Society* (2008): 1714-1720.

Acknowledgements

Funds for this research were provided by the Center on Materials and Devices for Information Technology Research (CMDITR), and the NSF Science and Technology Center No. DMR 0120967.

C. Porter would like to thank J.-H. Kang, E. Reichmanis, and the rest of the Reichmanis group for their contributions to her project this summer.

C. Porter would also like to thank Jeanne Pemeberton and Lingzi Sang of the University of Arizona for their encouragement and inspiration that got her here in the first place.

CANDICE PORTER is a senior in Chemistry and plans to enter graduate school for Materials Science and Engineering. She would like to continue work on Photovoltaics and hopes to see a time where the world is powered by the sun.

Charge-Transfer Excitations in Zinc Dipyrrins (ZIPYs): A Theoretical Study

SHANNON RIVERA, University of Georgia
Christopher Sutton, Chad Risko, Jean-Luc Brédas, Georgia Institute of Technology

Introduction

Organic solar cells, where the active layer is made up of conjugated organic molecules and/or polymers, produce electricity through the photovoltaic effect[1] and are particularly intriguing because of the potential for low-cost and large-scale processing and device flexibility. While there are a number of potential applications for organic solar cells, the underlying physical mechanisms behind their function are still not fully understood.[1, 2]The current understanding can be described in five stages/processes: (i) absorption of photons and the formation of excitons, (ii) exciton diffusion to the acceptor-donor interface, (iii) separation of the excitons into free negative (electron) and positive (hole) charges, (iv) charge migration, and (v) collection of the charges at the respective electrodes.[2]

Herein we study a distinct class of materials, zinc dipyrrins(ZIPYs),that are of interest as one of the active components in organic solar cells (Figure 1).[3]Similar systems are known to have strong charge-transfer excitations, where one half of the molecule contains the electron (negative charge) and the other half contains the hole (positive charge) of the Coulombically-bound quasi-particle.[1, 2, 4-13]The aim of this project is to understand the photoexcitation process and properly describe the charge-transfer character of the excited first state. Conclusions concerning the substitution pattern about the Zn core and the influence on the electronic and optical properties will be drawn.

Pyrrin (PYs) and ACAC Ligands:

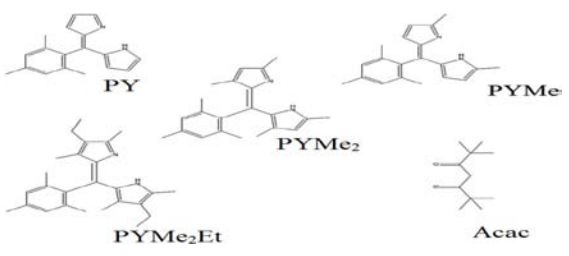

Zinc dipyrrins (ZIPYs):

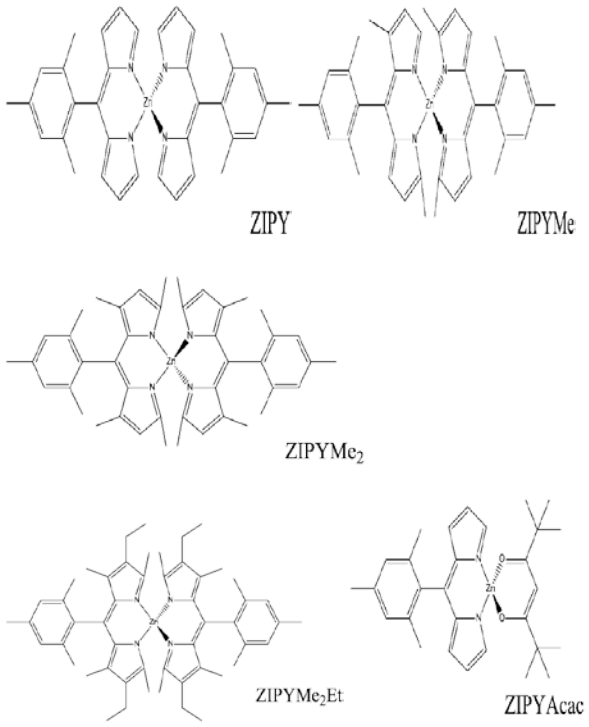

Figure 1. Structures of Pyrrins and Zinc Dipyrrins

Methodology

Density functional theory (DFT) will be the main method used in the study. The neutral states of PY ligands and full ZIPY molecules were optimized at theB3LYP/6-31G** level of theory,[14] which were used to examine the electronic structure, in particular, the frontier molecule orbitals, e.g., the highest-occupied molecular orbital (HOMO)and lowest-unoccupied molecular orbital (LUMO). The geometric structure will also be investigated as a function of the chemical substitution. The radical-cation and radical-anion states of the PYs and ZIPYs were optimized at the UB3LYP/6-31G** level of theory

to evaluate the molecular oxidative and reductive processes.[14]

Time-dependent DFT (TDDFT) was used to evaluate the excited states. However, descriptions of charge-transfer (CT) excited states are generally difficult with standard DFT functionals. Therefore, long-range corrected functionals will be employed also. Optimization of the long-range Coulomb cut-off parameter(ω) was performed to correct for the lack of proper long range decay of exchange in standard hybrid DFT functionals.[15] The optimization of the ω value was done for the CAM-B3LYP functional using the 6-31G** basis set by enforcing the DFT analogue of Koopman's theorem, whereby the difference between the ionization potential and HOMO eigenvalue is minimized.[16] Optimized-ω was CAM-B3LYP TDDFT calculations were performed with a solvent continuum model (methyl cyclohexane) to evaluate the photophysics of these molecules and to compare with the B3LYP description of the nature of the excitations. The data collected here will be used to provide further insight into available experimental data.[3]All calculations were carried out with the Gaussian 09 (Revision B.01) software suite. [17]

Results

To understand the first excitation of the ZIPY, we begin our investigation with the pyrrins molecules used as ligands in the ZIPY complexes. Beginning with the DFT optimizations of the ligands and the ZIPYs, (Figure. 2) the HOMO and LUMO plots of PY are representative of all the pyrrin ligands. It can be seen from the ligands that the MOs are localized on the nitrogen rings. It is expected that the HOMO and LUMO will be similar in the single molecule to that in ZIPY. This is shown in Figure 1, where the MOs of PY are very similar to the MOs of ZIPYAcac and ZIPY. This is also true for the rest of the pyrrin ligands and their respective Zn-complexes.

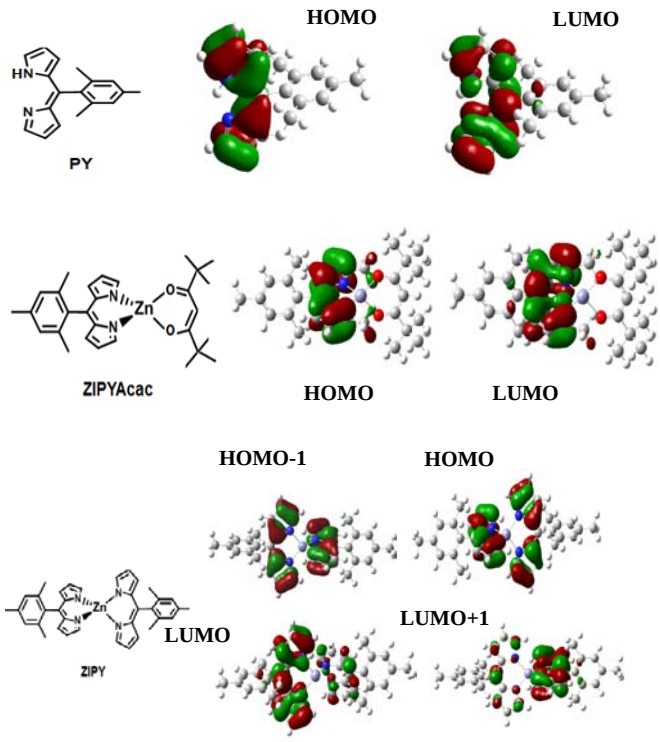

Figure 2. HOMO-LUMO plots of PY, ZIPYAcac, and ZIPY

ZIPYAcac was investigated because it contains only one pyrrin ligand. Importantly, a charge-transfer (CT) transition is not observed in this non-symmetrical molecule. As seen in Figure 2, the MOs of ZIPYAcac remain on the nitrogen rings of the pyrrin ligand. CT requires a transfer of MOs from one location to another on opposite sides of the molecule. This is also reconfirmed from the TDDFT of ZIPYAcac.

For ZIPY, the HOMO-1 and the LUMO+1 have also been included. Once again, the MOs are centered around the Zn and on the nitrogen rings, but the LUMO and LUMO+1 show signs of CT because they are localized on only one PY ligand. Because of this, it is expected that the LUMO and LUMO+1 will be involved in a CT. This can be seen from the TDDFT calculations.

The ionization potential (IP) for all the molecules is negative and the electron affinity (EA) is positive (Figure. 3), indicating that the ZIPYs will require substantial energy to

remove an electron though taking on an extra electron is a favorable process. In addition, it can be seen that as the electron-donating character of the substituent on the PY ligand increases, the IP becomes less negative (less energy is required to remove an electron), while the EA decreases but levels-off around 0.76eV for ZIPYMe$_2$ and ZIPYMe$_2$Et. These IP and EA results can be used to determine how the molecules could be used within an organic solar cell as either the accepter or donor material.

Molecule	AIP (eV)	AEA (eV)
ZIPYAcac	-6.29	0.80
ZIPY	-6.44	1.02
ZIPYMe	-6.16	0.91
ZIPYMe$_2$	-5.90	0.76
ZIPYMe$_2$Et	-5.68	0.77

Figure 3. Table of IP and EA of the ZIPYs

The first excitation of all the ZIPYs can be found in Figure 4. Included in the table are the MOs involved in the transition as well as the energy required for the transition and the oscillator strength (*f*) acquired from CAM-B3LYP TDDFT. It can be seen that the first excitation from ZIPYAcac is not a CT because the excitation does not involve the transfer of an electron from one side of the molecule to the other. The rest of the ZIPYs have CT-like character for the first excitation. It can be seen that as the degree of electron-donating character of the substituents increases, the energy of the transition decreases but levels-off at 2.96 eV.

Also, as the size of the molecules increases, the oscillator strength increases, but it levels-off. The oscillator strength indicates the probability of the excitation occurring; the higher, the more probable. It is expected that ZIPYMe2Et will follow the same trend even though the results have not be acquired.

Molecule	MOs	Energy (eV)	*f*
ZIPYAcac	HOMO → LUMO LUMO →HOMO	2.96	0.65
ZIPY	HOMO-1 → LUMO HOMO → LUMO+1	3.08	0.59
ZIPYMe	HOMO-1 → LUMO HOMO-1 → LUMO+1 HOMO → LUMO HOMO → LUMO+1	2.96	0.61
ZIPYMe$_2$	HOMO-1 → LUMO HOMO → LUMO+1	2.96	0.61
ZIPYMe$_2$Et	-	-	-

Figure 4. Table of the first excitation of the ZIPYs

Conclusion

As the larger electron-donating groups were added, the IP of the ZIPYs increased, and EA decreased. The EA levels-off around 0.76 eV as can be seen from ZIPYMe$_2$ andZIPYMe$_2$Et.

From the TDDFT calculations, it can be seen that as size increases, the energy of the transition decreases and the oscillator strength (*f*) increases; with little change seen after the first methyl group is added (ZIPYMe). The MOs involved in the transitions include HOMO-1, HOMO, LUMO, and LUMO+1. All of these data can be used to help understand how ZIPYs may be used in organic solar cells and provide an understanding of the process taking place in the molecule during the first excitation.

References

1. Brédas, J.-L., et al., *Molecular Understanding of Organic Solar Cells: The Challenges.* Accounts of Chemical Research, 2009. 42(11): p. 1691-1699.

2. Hains, A.W., et al., *Molecular Semiconductors in Organic Photovoltaic Cells.* Chemical Reviews, 2010. 110(11): p. 6689-6735.

3. Trinh, C.D., Saptaparna; Kirlikovali, Kent; Thompson, Mark E., *Symmetrical Breaking of ZIPYs (PowerPoint)*. 2012, University of Southern California. p. 1-37.

4. Grozema, F.C., et al., *QM/MM Study of the Role of the Solvent in the Formation of the Charge Separated Excited State in 9,9'-Bianthryl.* Journal of the American Chemical Society, 2005. 127(31): p. 11019-11028.

5. Filatov, M.A., et al., *π-Extended Dipyrrins Capable of Highly Fluorogenic Complexation with Metal Ions.* Journal of the American Chemical Society, 2010. 132(28): p. 9552-9554.

6. Sunahara, H., et al., *Design and Synthesis of a Library of BODIPY-Based Environmental Polarity Sensors Utilizing Photoinduced Electron-Transfer-Controlled Fluorescence ON/OFF Switching.* Journal of the American Chemical Society, 2007. 129(17): p. 5597-5604.

7. Sazanovich, I.V., et al., *Structural Control of the Excited-State Dynamics of Bis(dipyrrinato)zinc Complexes: Self - Assembling Chromophores for Light-Harvesting Architectures.* Journal of the American Chemical Society, 2004. 126(9): p. 2664-2665.

8. Qin, W., et al., *Photophysical Properties of Borondipyrromethene Analogues in Solution.* The Journal of Physical Chemistry A, 2005. 109(33): p. 7371-7384.

9. Piet, J.J., et al., *Symmetry Breaking in the Relaxed S1 Excited State of Bianthryl Derivatives in Weakly Polar Solvents.* Journal of the American Chemical Society, 2001. 123(22): p. 5337-5347.

10. Loudet, A. and K. Burgess, *BODIPY Dyes and Their Derivatives: Syntheses and Spectroscopic Properties.* Chemical Reviews, 2007. 107(11): p. 4891-4932.

11. Kobayashi, J., T. Kushida, and T. Kawashima, *Synthesis and Reversible Control of the Fluorescent Properties of a Divalent Tin Dipyrromethene.* Journal of the American Chemical Society, 2009. 131(31): p. 10836-10837.

12. Kee, H.L., et al., *Structural Control of the Photodynamics of –Dipyrrin Boron Complexes.* The Journal of Physical Chemistry B, 2005. 109(43): p. 20433-20443.

13. Asami, N., et al., *Two Different Charge Transfer States of Photoexcited 9,9'-Bianthryl in Polar and Nonpolar Solvents Characterized by Nanosecond Time-Resolved Near-IR Spectroscopy in the 4500−10 500 cm−1 Region.* The Journal of Physical Chemistry A, 2010. 114(22): p. 6351-6355.

14. Foresman, J.B.F., Æleen, *Exploring Chemistry with Electronic Structure Methods*. Second ed. 1996.

15. Baer, R., E. Livshits, and U. Salzner, *Tuned Range-Separated Hybrids in Density Functional Theory.* Annual Review of Physical Chemistry, 2010. 61(1): p. 85-109.

16. Yanai, T., D.P. Tew, and N.C. Handy, *A new hybrid exchange–correlation functional using the Coulomb-attenuating method (CAM-B3LYP).* Chemical Physics Letters, 2004. 393(1–3): p. 51-57.

Acknowledgements

I would like to thank Professor Jean-Luc Brédas for taking me on for this project, as well as my mentors Christopher Sutton and Chad Risko. Furthermore, I would like to thank the rest of the Brédas Research Group and the other REU students who aided me through the project. In addition, thanks goes to Professor Mark Thompson's research group at the University of Southern California. Lastly, thank you to NSF and CMDITR for funding my research project. No. CHE 0851730

SHANNON RIVERA a rising junior at the University of Georgia. Her current major is Chemistry, and her current intent is to continue her education to the graduate level.

Synthesis of Organic Core-shell Nanoparticles

KRISTA RUGAR, University of Arizona
John Tillotson, Luke Johnstone , Joseph W. Perry, Georgia Institute of Technology

Introduction

There is an increasing demand for organic fluorescent nanoparticles for use in organic light-emitting diodes (OLEDs), sensors[1], bioimaging[2] and three-dimensional fluorescence microscopy[3]. The fluorescence characteristics that are present in the solid-state of the dye are an important aspect for the construction of these nanoparticles.[1] The compound worked with in this study shows strong fluorescence in the solid-state. The majority of fluorescent dyes lack strong luminescence in their solid state. This is due to nonradiative self-quenching as a result of intermolecular interactions.[1] E,E-1,4-Bis[4'-(N,N-di-n-butylamino)styryl]-2,5-dimethoxybenzene [***1***] is known to show strong two-photon absorption and fluorescence in the solid state and in solution. Compounds with a large two-photon absorption cross section are beneficial for many functions due to the high localization and depth at which excitation can be generated.[3] Compound ***1*** contains two donor groups (D) and a weak acceptor group (A) with π bond bridges in the form of D-π-A-π-D. The π bond bridges in this compound can increase the quantity of intramolecular charge transfer and improve the strength of the two-photon absorption related to the charge transfer.[3] As an added benefit, two-photon absorption exhibits a very strong intensity dependence, which will permit for an enhanced spatial resolution in bioimaging applications.

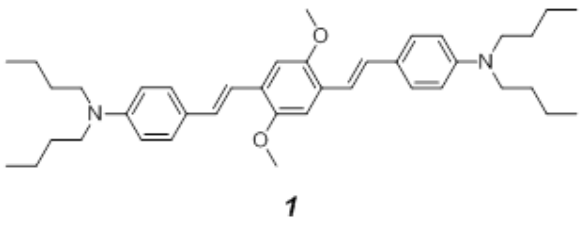

1

Figure 1. Molecular structure of compound *1*.

Compound ***1*** was synthesized and used to produce fluorescent nanoparticles. Silica was used to encapsulate the dye nanoparticles and produce the resulting core-shell particles. Silica encapsulation will protect the dye from the external environment and from reactions that would change its photophysical properties. The silica shell enables the core-shell particle to be functionalized. This would give the core-shell particle the properties needed to be used in targeting applications.

Experimental Methods

Materials

Absorption spectra were recorded on a Shimadzu UV-3101PC spectrophotometer and fluorescence emission spectra were measured on a Spex Fluorolog 2 1681 0.22m double spectrofluorimeter. ^{1}H NMR was recorded on Varian Mercury Vx400 MHz spectrometer in deuterated acetone with all chemical shifts referenced to the residual solvent signal. Dynamic light scattering (DLS) measurements were collected on a Wyatt DynaPro Plate Reader, and the results were analyzed using the included Wyatt Dynamics software. Particles were visualized using a JEOL100CX transmission electron microscope. Dionized water was adusted to pH 9 using ammonium hydroxide (28-30%, VWR). Particle synthesis solutions were filtered through either a 0.2µm Supor membrane filter (Life Sciences, St. Petersburg) or a 0.45µm nylon membrane filter (Whatman, Maidstone, UK) to remove large aggregates and large silica spheres.

Synthesis

Compound ***1*** was synthesized by an unpublished method in 72% yield. **^{1}H** NMR (400 MHz, acetone-d6): δ 7.38 (d, J=8.8 Hz, 4H; aromatic); 7.25 (d, J=16.4 Hz, 2H, alkene); 7.25 (s, 2H; aromatic); 7.14 (d, J=16.8, 2H; alkene); 6.7 (d, J=8.9 Hz, 4H; aromatic); 3.9 (s, 6H; OCH_3); 3.35 (t, J=7.6 Hz, 8H; $N(CH_2)_2$); 1.59 (p, J=7.7 Hz, 8H; CH_2); 1.38 (sx, J=7.5 Hz, 8H; CH_2) and 0.96 (t, J=7.4 Hz, 12H; CH_3). **UV-Vis:** λ_{max} = 428 nm.

Compound ***1*** was used to produce core-shell particles by simultaneous reprecipitation-encapsulation (Method A, Figure 2a) as described by Peng *et al*[4]. Compound ***1*** and octadecyl triethoxysilane (OD-TEOS) in a molar ratio 1:5 OD-TEOS:Dye were dissolved in tetrahydrofuran. The resulting solution (200 µL) was quickly added to 8 mL of pH 9 water, while under sonication. The solution remained under sonication for an additional fifteen minutes before filtering through a 0.2 micron Nylon membrane filter. The remaining THF was removed under reduced pressure. The solution was filtered again using a 0.2 micron Nylon membrane filter.

Core-shell particles were also produced by reprecipitation followed by encapsulation (Method B, Figure 2b). In method B, compound ***1*** was dissolved in THF (0.70 M) and 200 µL of this solution was quickly added to pH 9 water, while under sonication. The solution was left to sonicate for fifteen minutes to form nanoparticles. OD-TEOS was added to the solution under sonication in a ratio of 1:5 (OD-TEOS:Dye). Sonication continued for an additional fifteen minutes before the solution was filtered through a 0.45 micron Supor membrane filter. The remaining THF was removed under reduced pressure. The solution was again filtered through a 0.45 micron Supor membrane filter.

Results and Discussion

Concentration Dependence of Core-shell Particles

Utilizing method A, core-shell particles were prepared using different concentrations of OD-TEOS and compound ***1***. Dynamic light scattering (DLS) was used to measure the hydrodynamic radius and the percent standard deviation a function of silane/dye ratio. The ratio 2:15 (OD-TEOS:Dye) produced core-shell particles with the smallest percent standard deviation (Table 1).

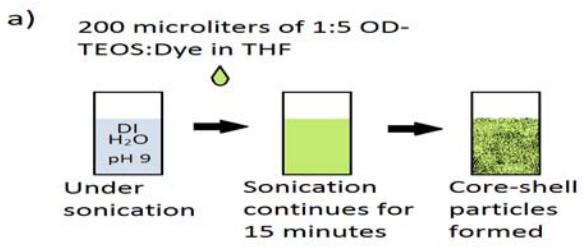

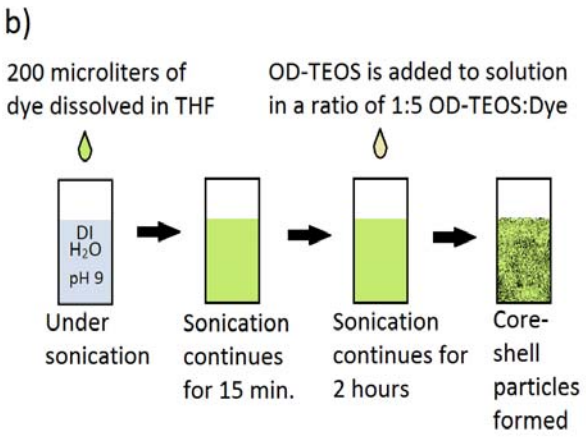

Figure 2. Diagrams of core-shell formation (a) method A and (b) method B.

Table 1. Dynamic light scattering data of concentration dependence of core-shell particles produced using method A. Core-shell particles are present in pH 9 water.

OD-TEOS:Dye	Hydrodynamic Radius (nm)	% Standard Deviation
1:1	94.1	25.2
2:5	65.2	38.1
1:5	34.1	6.5
2:15	36.6	4.7
1:10	33.2	10.6

Time Dependence

Time dependence experiments were conducted using the two solutions that showed the least percent standard deviation from the concentration variance experiment (Table 1). Particles were synthesized using a ratios 1:5 and 2:15 (OD-TEOS:Dye) with varying times of sonication, using method A. The times of sonication include: 5 minutes, 15 minutes, 30 minutes and 1 hour. The DLS data showed that the solution with 2:15 (OD-TEOS:Dye) produced the smallest percent standard deviation amongst all the samples, with the original fifteen minute sonication producing the most monodisperse sample (Table 2).

Table 2. Dynamic light scattering data of core-shell particles produced from time dependence experiment. Core-shell particles are in pH 9 water.

OD-TEOS:Dye	Time (min)	Hydrodynamic Radius (nm)	% Standard Deviation
1:5	5	34.6	14.5
	15	34.1	6.5
	30	43.5	22.6
	60	39.7	17.8
2:15	5	28.3	9.5
	15	36.6	4.7
	30	35.4	14.8
	60	30.9	9.3

Sonication vs Stir Bar

The type of mixing conducted during the experiment to produce core-shell particles was also varied. Instead of using sonication to mix the solvents, in method A, a stir bar was used. The experiment was conducted in the same manner as method A, with the exception of the sonication. The stir bar was placed on its fastest setting, 1600 rpm. DLS showed that these samples produced core-shell particles with a large percent standard deviation (Table 3). Sonication was used for the remaining experiments due to a large percent standard deviation measured from the samples produced using the stir bar.

Table 3. Dynamic light scattering data of method A composed of using a stir bar to mix the solution instead of sonication. Core-shell particles are present in pH 9 water.

OD-TEOS:Dye	Hydrodynamic Radius (nm)	% Standard Deviation
1:5	33.6	17.7
2:15	9.6	86.3

Properties of Non-coated and Core-shell Particles

Non-coated nanoparticles were synthesized to compare the absorbance between coated and non-coated nanoparticles. The absorbance spectra for silica coated particles and bare particles were compared to that of compound ***1*** (Figure 4). The core-shell and non-coated nanoparticles both exhibit a slight blue shift in comparison to compound ***1*** in toluene and appear to have a shoulder around 475 nm. DLS showed that the hydrodynamic radii of the two samples consist of similar size, although the core-shell particles show a larger polydispersity.

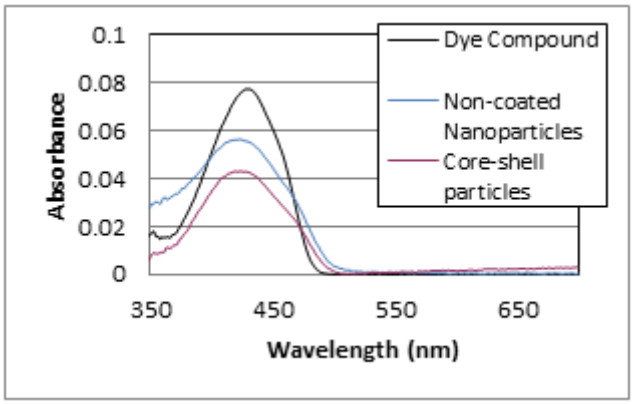

Figure 3. Ultra-violet visible spectrum of the absorbance present in the dye compound, non-coated nanoparticles and core-shell particles. Particles are present in pH 9 water.

Table 4. Dynamic light scattering data of non-coated nanoparticles and core-shell particles. Particles are present in pH 9 water.

	Hydrodynamic Radius (nm)	% Standard Deviation
Non-coated Nanoparticles	34.1	6.5
Core-shell Particles	33.3	10

Age Dependence of Core-shell Particles

Unreacted silane present in the solutions of core-shell particles would cause the shell to increase as time progresses. The aging effects of the core-shell particles were measured with the intent of observing changes in the hydrodynamic radius, percent standard deviation, absorbance and fluorescent emission of the core-shell particles. Samples were prepared using method A on different dates. The samples aged three weeks, one week and zero weeks when the data was collected. The DLS data showed that the sample with the lowest polydispersity was the oldest

sample followed by the sample synthesized most recently. Additional experiments need to be done with these core-shell particles to determine what is causing the difference between polydispersity amongst the samples.

The absorbance spectra show that all three samples have the same λ_{max} at 420 nm (Figure 4a); although the oldest sample has a slightly broader absorption than the other two samples. The fluorescence emission was measured using these three samples (Figure 4b). Week 0 and week 1 samples are consistent with each having a max intensity around 540 nm and a shoulder at a lower wavelength. The 3 week sample showed a max fluorescence intensity at 563 nm and does not portray the second peak at the lower wavelength. The concentration of the core-shell particles in these samples has yet to be determined making the analysis of the data inconsistent at this point.

Table 5. Dynamic light scattering data of aged varied samples using the original reprecipitation-encapsulation method with 2:15 (OD-TEOS:Dye). Particles are present in pH 9 water.

Age of Sample	Hydrodynamic Radius (nm)	% Standard Deviation
0 Weeks	26.9	13.4
1 Week	26.1	21.8
3 Weeks	34.5	5.3

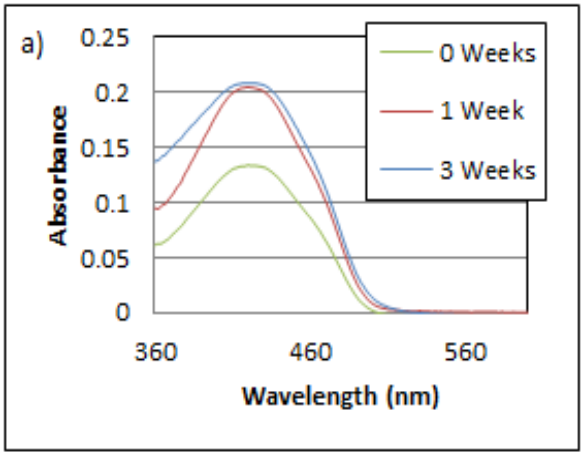

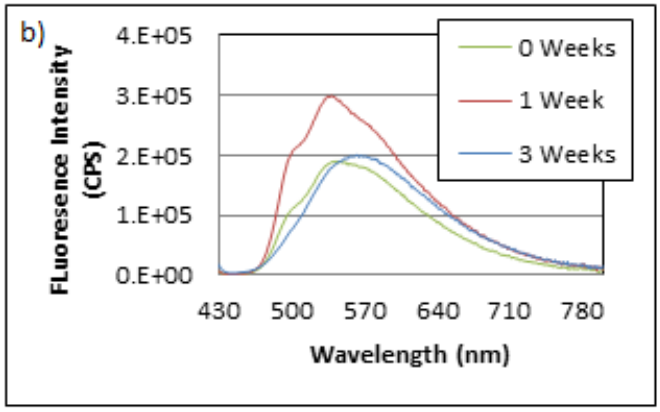

Figure 4. (a) UV-vis and (b) fluorescence spectra of aged varied samples using the original reprecipitation-encapsulation method with 2:15 (OD-TEOS:Dye). Samples present in pH 9 water.

Method A vs Method B

The photophysical properties of particles made by method A and method B were used to determine differences between the two methods. The absorbance of the core-shell particles produced from methods A and B were measured using UV-Vis (Figure 5a). A red shift is present in the core-shell particles produced from method B. The λ_{max} for method B is 431 nm while for method A is 420 nm. The absorbance spectrum for method A also displays a broader absorbance peak. The fluorescence spectrum was measured for each of the methods. The fluorescence spectra for both samples show the same general shape. Method A had an emission maximum at 542 nm while method B had an emission maximum at 528 nm. Once the concentration of core-shell particles are determined, the quantum efficiencies of the nanoparticles and the core-shell particles will determined.

DLS showed that method A produced particles with a hydrodynamic radius of 36.6nm with a relatively low percent standard deviation (Table 6). Method B produced much larger particles and consisted of a larger present standard deviation. This may be attributed to the presence of silica spheres which do not contain dye. The difference in size of the core-shell particles produced from the two different methods is also evident when images of the particles were captured using transmission electron microscopy (TEM) as seen in figure 6. The core-shell particles produced

from method B exhibit a uniform circular shape in comparison to method A core-shell particles. Method B produced much larger core-shell particles than did method A, although method B consists of a much larger size variance among its core-shell particles.

Table 6. Dynamic light scattering data of particles made by method A. Concentrations consist of 2:15 (OD-TEOS:Dye). Core-shell particles are present in pH 9 water.

Method	Hydrodynamic Radius (nm)	% Standard Diviation
Method A	36.6	4.7
Method B	54.7	18.3

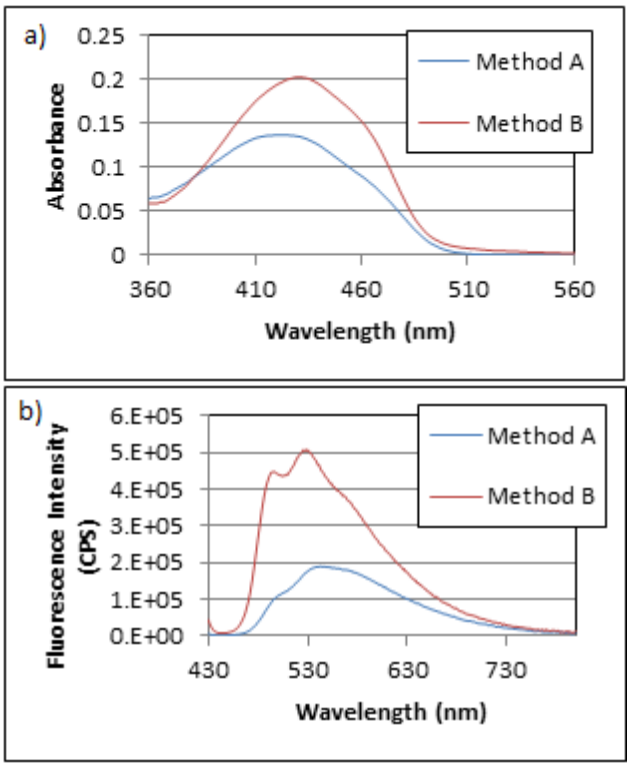

Figure 5. (a)Ultra violet visible and (b) fluorescence spectra comparing method A and method B. Core shell particles are present in pH 9 water.

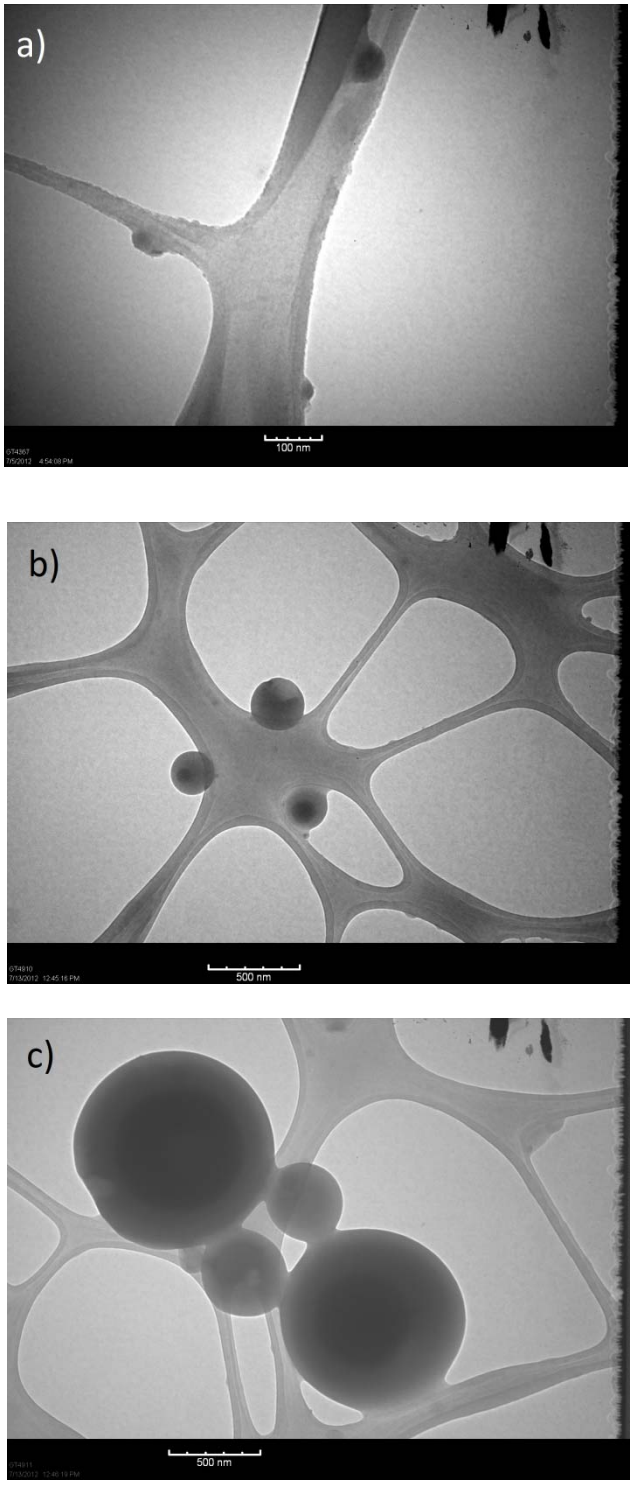

Figure 6. Transmission electron micrograph of the method A (a) and method B (b and c). Both samples consist of a silane: dye ratio of 2:15.

Conclusion

Core-shell particles were produced using two different methods. Different concentrations of the dye compound and silane were tested and the results show that the 2:15 (Octadecyl triethoxysilane:Dye) silane:dye ratio produced samples with the smallest variance in size amongst the core-shell particles. Method A produced particles with a small percent standard deviation in particle size. Method B produced core-shell particles with larger hydrodynamic radii and larger percent standard deviation. Micrographs of method A core-shell particles were hard to obtain using transmission electron microscopy (TEM). The micrographs that were captured are consistent to the dynamic light scattering data (DLS) in relation to the size of the core-shell particles. The core-shell particles produced by method B produced better images with TEM. These silica shells are visible and the particles have a circular shape present in the TEM images, although the core-shell particles are particularly large, some around 500 nm.

Addition research will be conducted on these core-shell particles. The methods used may be modified further in an effort to produce a monomodal sample of core-shell particles with the fluorescent capabilities of the dye compound used. Contrasting agents will be used to assist in visualization in TEM.

References

1. Yao, Hiroshi, Minami Yamashita, and Keisaku Kimura. "Organic Styryl Dye Nanoparticles: Synthesis and Unique Spectroscopic Properties." *Langmuir* 25.2 (2009): 1131-1134. Print.

2. Miyashita, Yousuke, Shinichi Horino, Hitoshi Kasai, Hidetoshi Oikawa, and Hachiro Nakanishi. "Preparation and Luminescence Properties of Organic Phosphorescent Nanoparticles." *Japanese Journal of Applied Physics* 51.025002 (2012): 1-5. Print.

3. Rumi, Mariacristina; Ehrlich, Jeffrey E.; Heikal, Ahmed A.; Perry, Joseph W.; Barlow, Stephen; Hu, Zhongying; McCord-Maughon, Dianne; Parker, Timothy C.; Röckel, Harald; Thayumanavan, Sankaran; Marder, Seth R.; Beljonne, David; and Brédas, Jean-Luc. "Structure−Property Relationships for Two-Photon Absorbing Chromophores: Bis-Donor Diphenylpolyene and Bis(styryl)benzene Derivatives." *Journal of the American Chemical Society* 122.39 (2000): 9500-9501. Print.

4. Peng, Hongshang; Wu, Changfeng; Jiang, Yunfei; Huang, Shihua; and McNeill, Jason. "Highly Luminescent Eu^{3+} Chelate Nanoparticles Prepared by a Reprecipitation−Encapsulation Method" *Langmuir* 23.4 (2007): 1591-1594. Print.

Acknowledgments

This research was made possible by the NSF Science and Technology Center on Materials and Devices for Information Technology Research No. DMR 0120967, NSF Research Experiences for Undergraduates Program Hooked on Photonics, 3M Corporation and 3M Summer Scholars Program. The authors would also like to thank Dr. Kathaperumal for his expertise in core-shell synthesis.

KRISTA M. RUGAR is currently in pursuit of a chemistry degree from the University of Arizona. Krista plans to participate in future research programs and internships prior to her graduation.

The Photophysics of DCM Dyed Potassium Hydrogen Phthalate Crystals

TAWNNI TAYLOR, Shepherd University
Erin Riley, Philip Reid, University of Washington

Introduction

Solar cells are the rising stars of science in the 21st century. However, chromophores within the solar cells decompose or lose their favorable photophysical properties quickly because of environmental factors, such as oxygen exposure or irreversible electron transfer with the host. To preserve device integrity, we must understand the photophysical interactions between the host and chromophore. This can be accomplished by engineering a controlled environment in which the guest-host alignment is well defined. 4-dicyanomethylene-2-methyl-6-4-dimethylaminostyryl-4-H-pyran (DCM) is a laser dye similar to chromophores used in solar cells. We used DCM to do tests because the chromophores in solar cells aren't fluorescent, which limits our ability to monitor excited state reactions, opposed to DCM, which is fluorescent. We are interested in understanding the interaction of DCM overgrown into crystals of potassium hydrogen phthalate (KAP). The crystal host aligns the molecules upon incorporation, and is oxygen impermeable, which provides an opportunity to understand the host's influence on DCM's photophysics without photo-oxidation at ensemble and single molecule levels.
Here we present the preliminary growth and ensemble characterization of DCM/ KAP crystals and compare them to solution phase experiments to determine how DCM is effected by solvent polarity, pH, and in the solid state.

Experimental Methods

Crystal Growth: Two methods of crystal growth were tested; slow cooling and evaporation of supersaturated solutions of KAP, but the slow cooling gave higher quality crystals. Slow cooling method is as follows: 14.3g of KAP was added to 75mL of nanopure water. DCM was dissolved in a minimal amount of ethanol and added to the solution. It was then heated until all the KAP had dissolved and cooled for a few minutes whereupon seed crystals were added. The container was sealed and fully submerged into a temperature controlled water bath. The water started at 47.0 C and slowly decreased by 0.1 C/hr over a few days.

Spectroscopy: The molar absorptivity was determined in ethanol and water solutions by serial dilutions using Beer's law of absorbance. The effect of pH on DCM was observed through absorbance and fluorescence. 1.03E-4 M DCM in water buffered with 5mM KAP was prepared, and HCl and NaOH were added to make separate solutions of pH 2.1 and 12.3, respectively. The two were combined to make several intermediate solutions.

After the crystals were collected, the sectors that the dye went into were observed with a fluorescence microscope, and absorbance and fluorescence measurements were collected.

Data

Picture 1: DCM in KAP crystal in daylight.

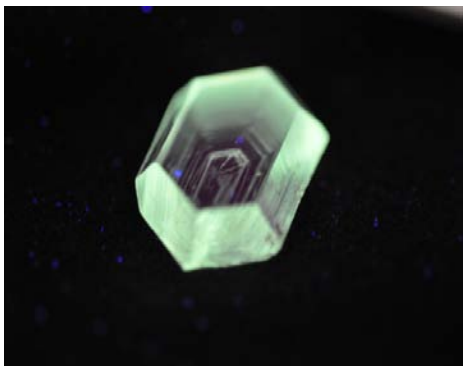

Picture 2: DCM in KAP crystal in UV light.

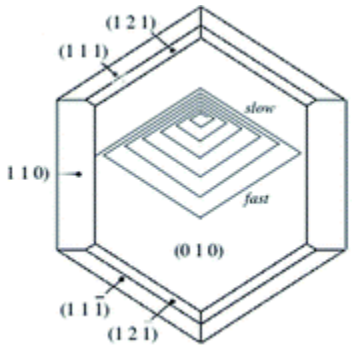

Picture 3: KAP habit.

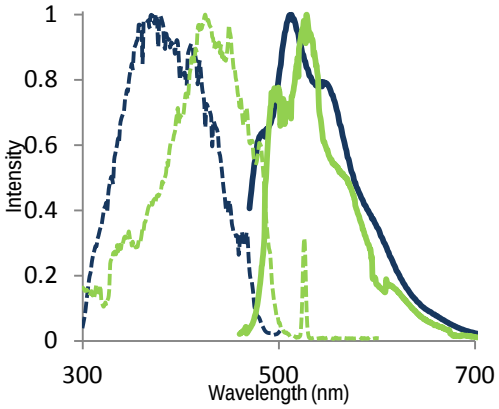

Figure 1: emission (solid) and excitation (dashed) spectra of DCM in a KAP crystal (blue) and DCM in hexanes (green).

The emission spectrum of DCM in KAP is most similar to the solvent hexanes. This suggests KAP provides a similar environment to non-polar hexane. The shift in excitation spectrum is consistent with the larger dielectric constant of KAP (~8.5) than hexane (~1.9). Lippert's equation predicts a larger stokes shift for increased dielectric constant[1].

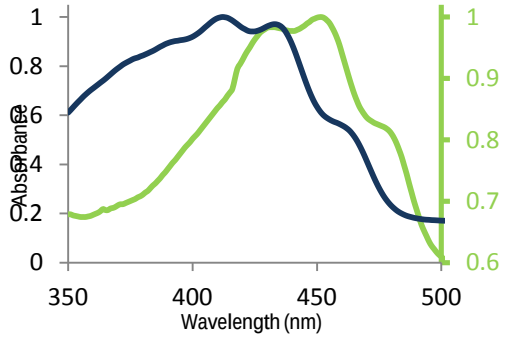

Figure 2: Absorbance spectra of DCM in KAP (blue) and hexanes (green).

The absorbance spectrum of DCM in hexanes and is also similar to DCM in KAP. However, the spectrum of DCM in KAP shows more structure than in hexanes, consistent with a more rigid environment in the crystal. The blue shift in the crystal is consistent with stabilization of the ground state of DCM in KAP.

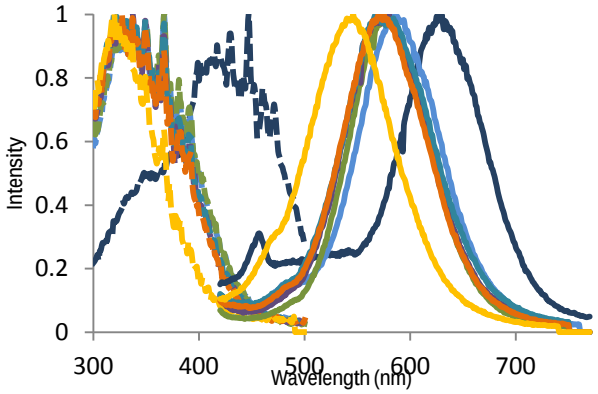

Figure 3: Fluorescence excitation (dashed) and emission (solid) spectra of DCM at pH's 3.42 (dark blue), 3.84 (light blue), 5.01 (green), 6.26 (purple), 7.40 (dark aqua), 10.04 (dark orange), 12.51 (golden yellow).

The fluorescence of DCM in water is less structured than in KAP or hexanes, as can be seen in the aqueous spectra in figure 3. This indicates intermolecular interactions with the solvent, which is polar, that averages out vibrational structure.

The emission spectra of DCM over the pH range 3.42-12.51 is shown in figure 3. A shift to the blue with increasing pH is observed. This may be due to decreased hydrogen bonding with DCM's cyano groups, or a change in isomer. DCM exists as a mixture of cis and trans isomers, where the cis isomer has a lower absorbance than trans. For all pHs past 3.84, the excitation spectra are similar which means that the ground state of DCM at those pHs doesn't change. However, before pH 3.84 the excitation changes drastically, which shows the ground state changing.

Graph 4: DCM pH Absorbance

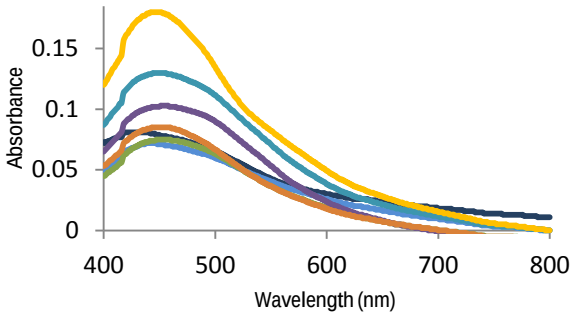

Figure 4: Absorbance spectra of the same solutions in figure 3 [3.42 (dark blue), 3.84 (light blue), 5.01 (green), 6.26 (purple), 7.40 (dark aqua), 10.04 (dark orange), 12.51 (golden yellow)].

The absorbance spectra mostly indicate changes in the molar absorptivity with pH. The pH 12 solution has the greatest absorbance, even though all solutions have the same concentration of DCM. It can be noted that, as the pH of DCM gets more acidic, the spectrum shifts more towards the blue. This appears to start slightly at the pH 3.84, but is very visible at the pH 3.42.

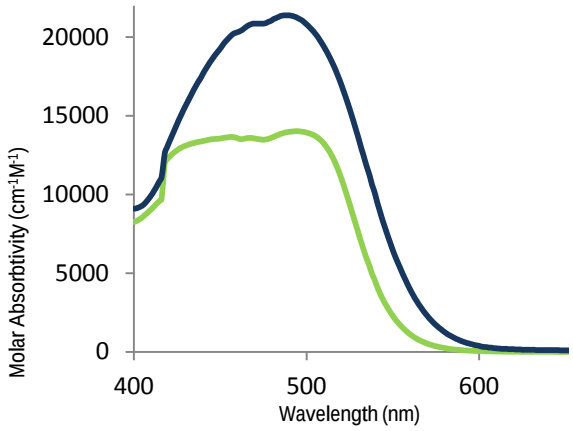

Figure 5: Molar absorptivity of DCM in ethanol (green) and water (blue).

The molar absorbtivity (ε) of DCM was calculated to observe how strongly DCM absorbs light (figure 5). Both DCM in ethanol and DCM in water peak at the same wavelength, but ethanol's molar absorbtivity is lower than that of water's. DCM in solution exposed to light exists as a mixture of cis and trans isomers. This could be due to more of the cis-isomer present in ethanol.

Conclusions

DCM very effectively incorporates itself into a KAP crystal in the [111] and [010] sectors[2]. As the crystal forms, layer by layer, the DCM molecules gather on top of it in between the layers. This can be seen through the slices of one crystal from top to bottom.

The shift in pH of DCM in more acidic solutions is interesting and, as of yet, does not have a clear explanation. It would be interesting to continue to explore that phenomenon since the KAP crystal is an organic salt that contains an extensive hydrogen bond structure between the phthalate monomers. Understanding how DCM interacts with hydrogen bonding solvent is important to understanding its photophysical properties.

So far we have investigated the solvent effects on DCM and have found that the crystal environment is most similar to that in a non-polar solvent. Next we would like to investigate the photo-induced charge-transfer and cis- trans-isomerization that DCM is known to demonstrate in certain solvents. Are these mechanisms operative in DCM/KAP crystals, and can they be resolved? If so, the next step in this research would be to look at DCM on a single molecule level which will provide detailed information on the kinetics of these processes, and determine how the host promotes them. This will allow for better designs of chromophore composite devices such as solar cells.

References

1.Lakowicz, J. *Principles of Fluorescence Spectroscopy. Kluwer Academic*, 1999, *New York*.

2. Barbon, Antonio. *Triplet States of the Nonlinear Optical Chromophore DCM in Single Crystals of Potassium Hydrogen Phthalate and Their Relationship to Single-Molecule Dark States*, 2009.

Acknowledgements

Thanks goes to everyone who help me get past the culture shock of the west coast, and Dr. Lisa Park-Gehrke for telling me about this internship.

Earth Will Have to Dye Another Day: Chromophores to Curtail Catastrophe

PAYTON J. WARD, University of Washington
Peter V. Johnston, Philip J. Reid, University of Washington

Introduction

In 2010 our planet used 142,000 TWh of power; this number is expected to continue to increase with population growth and urban development.[1] The majority of this energy is derived from hydrocarbon sources and has resulted in significant emission of CO_2 into the atmosphere. The CO_2 produced per kWh used has been declining; however, even if the energy used per person was to be held constant, population growth alone will cause CO_2 emission to rise and threaten the quality of life on Earth.[2] Solar power is emerging as a viable and affordable clean energy source with the potential to eliminate the use of non-renewable energy sources. Our charge as scientists is to develop new technology to enable more affordable and more efficient harvesting of solar energy thus eliminating the need for hydrocarbon based fuel.

Solar cell technology is an attractive replacement for fossil fuels. The number of nuclear power plants required to generate 142,000 TWh of power is unreasonable.[2] Wind, geothermal, and other sources of clean energy are not to be ignored, but these aren't as abundant as that of the sun. The amount of energy from the sun that reaches the earth in one hour is more energy than the earth's population consumes in one year. The cost of solar power has prevented a major shift in the source of the planet's energy supply. Still, solar power currently stands out as the single viable solution that can supply the world's current energy needs.[3, 4]

Since the late 1970s photovoltaics (PVs) have been under intense research; the results of which are summarized by the National Renewable Energy Laboratories (Figure 1). Solar cell

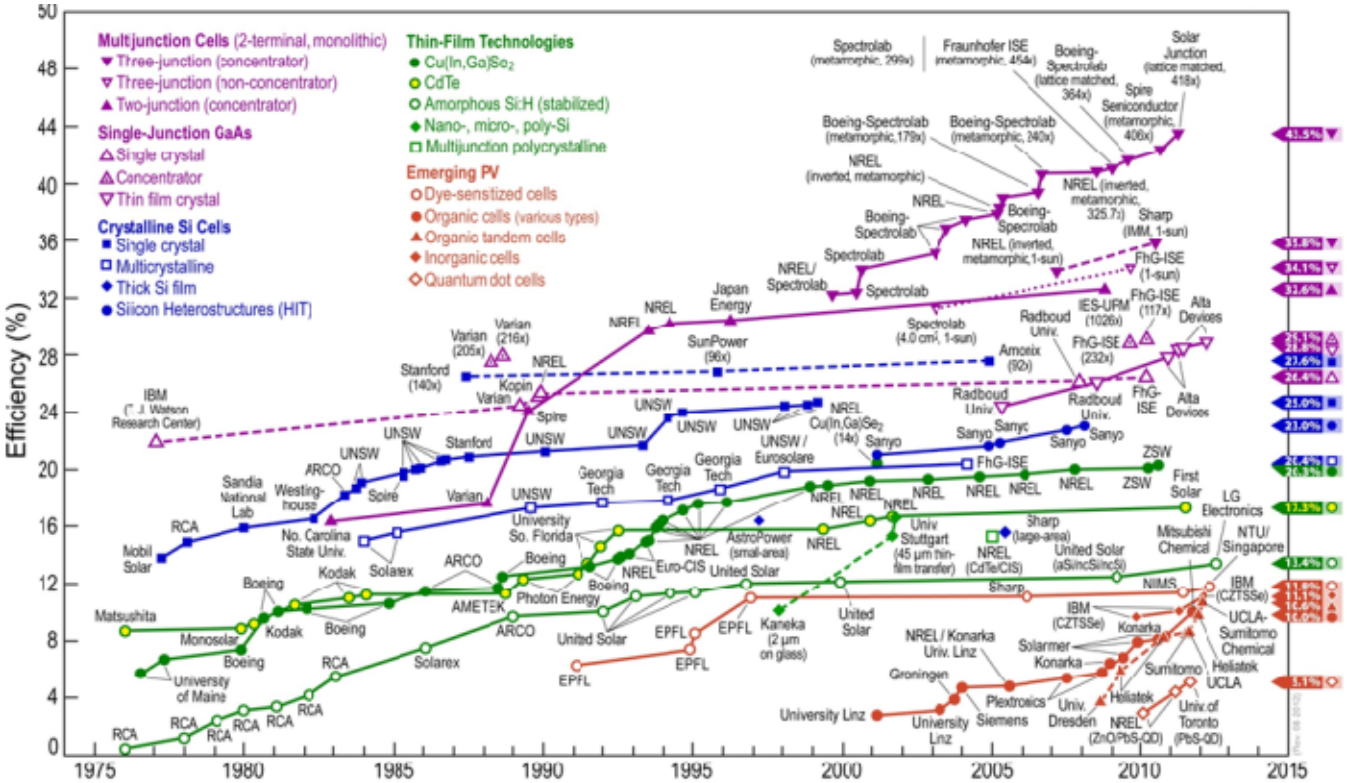

Figure 1. A chart displaying the record conversion efficiencies of research solar cells from 1975 to the present.

technology can be loosely categorized into three main branches: solid-state crystalline, organic polymer, and dye-sensitized. Solid-state, crystalline silicon semiconductors have made great strides in power conversion efficiency (PCE), the percentage of the sun's energy that is converted into electrical energy, but it remains one of the most expensive sources of energy due to manufacturing costs.[5, 6] Nanotechnology has reduced the cost of inorganic PVs, but often rely on toxic materials that must be mined, such as cadmium or lead. Organic polymer cells are inexpensive to manufacture, but they lack the PCE to replace current technology.[5, 6] Our focus is on studying organic chromophores that can be used in dye-sensitized solar cells (DSSCs). DSSCs are not as expensive to make as crystalline silicon cells and have better PCEs than organic cells.[6, 7] It is because of this middle ground between cost and power conversion that make DSSCs an attractive target for investigation.

DSSCs consist of dyes adhered to a metal oxide semiconductor (nanoparticles, typically TiO_2) in an electrolyte solution (Figure 2). The dye molecule absorbs light to form an electron-hole pair, known as an exciton. The electron is separated from the hole and transported to the nanoparticles then ultimately the anode. The electron performs work and eventually returns to the dye via the electrolyte. While this is occurring, the hole is taken by the electrolyte.[7]

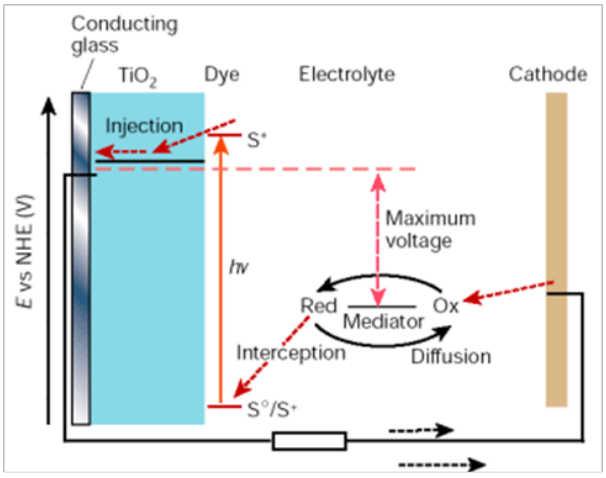

Figure 2. Electron path of an electron in a DSSC and relative energy levels of DSSC components.

Band theory plays an important role in the performance of DSSCs. The lowest unoccupied molecular orbital (LUMO) of the chromophore must be matched to the conduction band of the TiO_2 (-4.26 eV). Then the electrolyte must be able to transfer an electron to the highest occupied molecular orbital (HOMO) of the dye, requiring the energy of dye's HOMO to be lower than that of the electrolyte, -4.87 eV for the I^-/I_3^- electrolyte.[8]

Another piece to the DSSC performance puzzle that involves electron transfer is proton coupled electron transfer (PCET). PCET involves a proton and an electron starting in different molecular orbitals of the same molecule and being transferred to different molecular orbitals of another molecule. Recent finding suggest that PCET not only plays a role in transferring the photoexcited electron from the dye to the TiO_2 but also in the electron transfer among the TiO_2 nanoparticles.[9]

These factors must be considered when developing a synthesis targeting a molecule for use in DSSCs. We utilized well understand methods developed for electro-optic chromophores and adapted them to meet the previously stated requirements. We chose to develop molecules with tetraene bridges knowing that they would have high absorptivity in the visual spectrum. The tetraene bridges were ring-locked using isopherone units in order to improve photo and thermal stability. We also incorporated a carboxylic acceptor based on the acceptor of Y123, an organic DSSC chromophore (Figure 3).[10] Our ultimate goal in this study is to develop an organic, synthetic dye to replace the ruthenium-based dye used in typical DSSCs.

Experimental Methods

The three organic chromophores were synthesized and their performance as sensitizers in dye-sensitized solar cells (DSSCs) was compared. The dyes possessed the same tetraene, π-conjugated bridge and cyanoacetic acid electron-accepting group but differing electron-donating groups. The dyes were utilized in prototype DSSCs. TiO_2 was used as the semiconductor nanoparticles and I^-/I_3^- as the electrolyte.

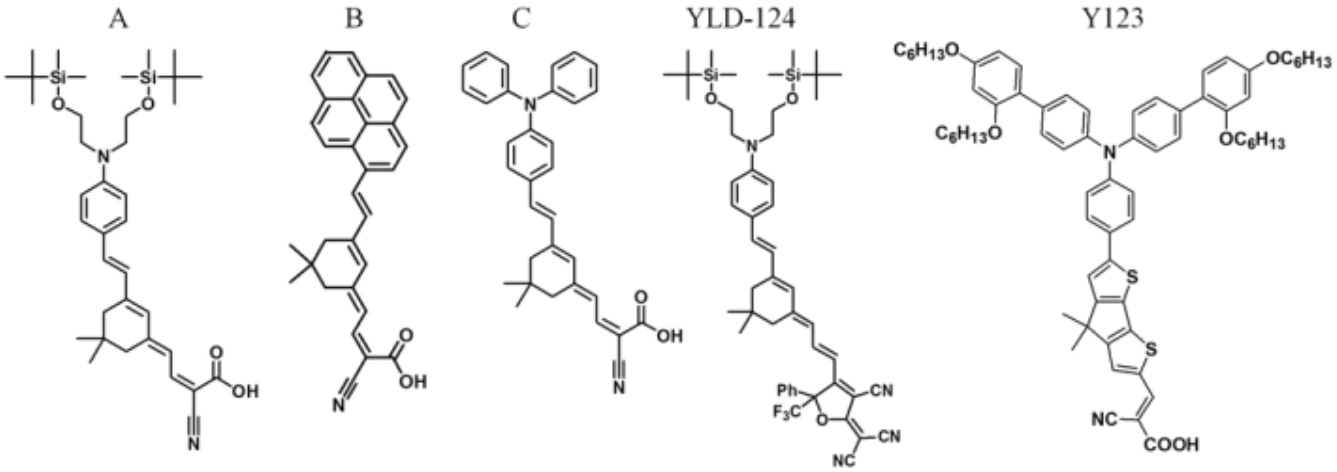

Figure 3. The dyes synthesized along with YLD-124 and Y123.

Synthesis of chromophores:

Addition of the isopherone unit of the bridge to the donor aldehyde proceeded via Knoevenagel condensation by reacting it with 10 molar equivalents of sodium methoxide and 2.1 molar equivalents of isopherone in methanol. The bridge was then extended at the carbonyl carbon by a modified Wittig-Horner cyanomethylation using 7.5 molar equivalents of NaH, cyanomethylphosphonate, and **2** in THF. Next, DIBAL reduction with 1.7 molar equivalents of DIBAL-H in toluene produced **4** in good yield.[11] Finally, Knoevenagel condensation of **4** with 3.5 molar equivalents of cyanoacetic acid and 12 molar equivalents of piperidine in chloroform resulted in the final product.[12] Chromophores characterized by ^{1}H NMR and ESI mass spectrometry.

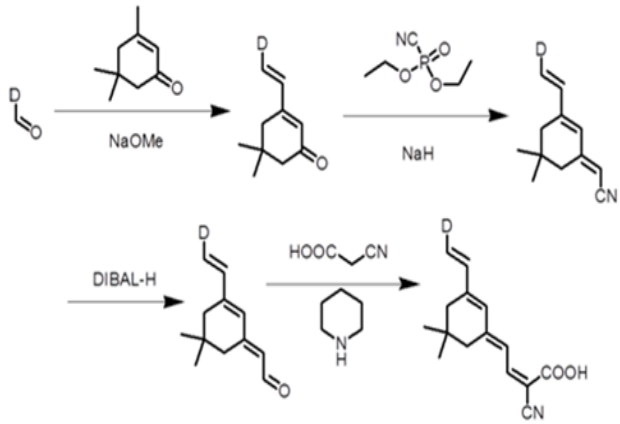

Figure 4. Reaction scheme used for bridge extension and acceptor addition.

Device Fabrication:

TiO_2 nanoparticles were made into a paste by mixing commercially obtained DegussaP25 TiO_2 and an acetic acid solution with a pH of ~4.0. The electrolyte was prepared by dissolving iodine in anhydrous ethylene glycol then mixing this solution with KI in a dark container.[13]Glass/indium tin oxide (ITO) slides were cleaned by sonication in acetone and isopropanol. The cleaned slides were taped leaving 0.5625 in^2 of ITO exposed. The TiO_2 paste was spread evenly across the exposed ITO with the side of a glass rod. The TiO_2 was sintered to the slides at 450°C for 30 minutes.[13] Concentrated solutions of the chromophores in acetone were then dropped onto the sintered slides so that the dye completely covered the TiO_2. After the acetone had been allowed to evaporate, the slide was rinsed to remove the excess dye.

On another slide a layer of hydrocarbons was placed onto the ITO side by holding the slide over a candle flame.[13] The electrolyte solution was dropped onto the carbon. The electrolyte and nanoparticle slides were sandwiched together and held together with binder clips.

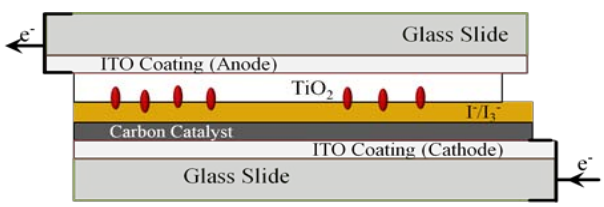

Figure 5. Device architecture used for the solar cells fabricated.

Device Testing:

The completed devices were kept out of light until tested. The devices were tested using two different methods. In the first method, each device was exposed to the light of a fluorescent bulb at a distance of 48.5 in for one minute with a voltmeter was assumed that the energy maximum absorbance corresponded to the dyes' energy band gaps. This may pose a problem as these measurements were taken in solution, but the chromophores in the devices are in the solid state.

After testing the solar cells under the fluorescent bulb, it was found that there was no statistical difference between the dyes synthesized with the tetraene bridge and cyanoacetic acceptor.

However, there were individual devices using dye C that outperformed devices using the other dyes. The devices with the synthesized dyes also outperformed the devices lacking chromophores and far outperformed those utilizing YLD-124.

Dyes	Energy of Light of Max. Absorbance (eV)	Molar Absorptivity ($L\ mol^{-1}\ cm^{-1}$)	Average Open Circuit Produced in Devices (mV/cm^2)
A	2.363	7625.6	59.2
B	2.601	27863	79.4
C	2.487	19346	88.7
YLD-124	1.592	58335	-1.7
No Dye	--	--	15.0

Chart 1. Data collected from UV-vis measurements of the dyes and the average open circuit voltages of the devices under a fluorescent bulb.

attached. The greatest open circuit voltage (V_{OC}) reading during the minute the device was being tested was recorded. Devices without any chromophore and devices using YLD-124 (an electro-optic chromophore not designed for use in DSSCs) were used as controls. In the second method, devices modified with tape around 3 sides of the TiO_2 square and containing either dye B or C were attached to a source measurement unit and set in front of an AM 1.5 solar simulator operating at a source power (P_{source}) of 299.5 W. From this method, current vs. voltage plots for the devices were obtained.

Results and Discussion

Spectral measurements for all four chromophores used in the devices were obtained. Dye A had the lowest molar absorptivity, with less than half the absorptivity of the second least absorbent dye. YLD-124 had more than twice the molar absorptivity of the second highest dye. Dyes A, B, and C all had maximum absorbances in the 2.485-2.605 eV range. YLD-124's maximum absorbance was in light of lower energy: 1.592 eV (Chart 1). It

However, there were individual devices using dye C that outperformed devices using the other dyes. The devices with the synthesized dyes also outperformed the devices lacking chromophores and far outperformed those utilizing YLD-124.

The testing of the solar cells under a solar simulator yielded current vs. voltage curves (Chart 2). From these curves we were able to find a least square regression polynomial function with an order of 6.0 for the section of the plot where the voltage was greater than or equal to 0.0 and the current was less than or equal to 0.0. Utilizing the equation for the regression, we found the maximum power (P_{max}) output of the cells, as well as, the V_{OC} and short circuit current (I_{SC}) and used these to calculate the PCEs of the devices (Equation 1).

$$\eta = \frac{V_{OC} \times J_{SC} \times FF}{I_{source}} \qquad (1)$$

$$FF = \frac{P_{max}}{V_{OC} \times Jsc} \quad (2)$$

$$I_{source} = \frac{P_{source}}{Area} \quad (3)$$

These calculations gave the results of 7.82E-4% conversion for dye B and 7.85E-4% for dye C.

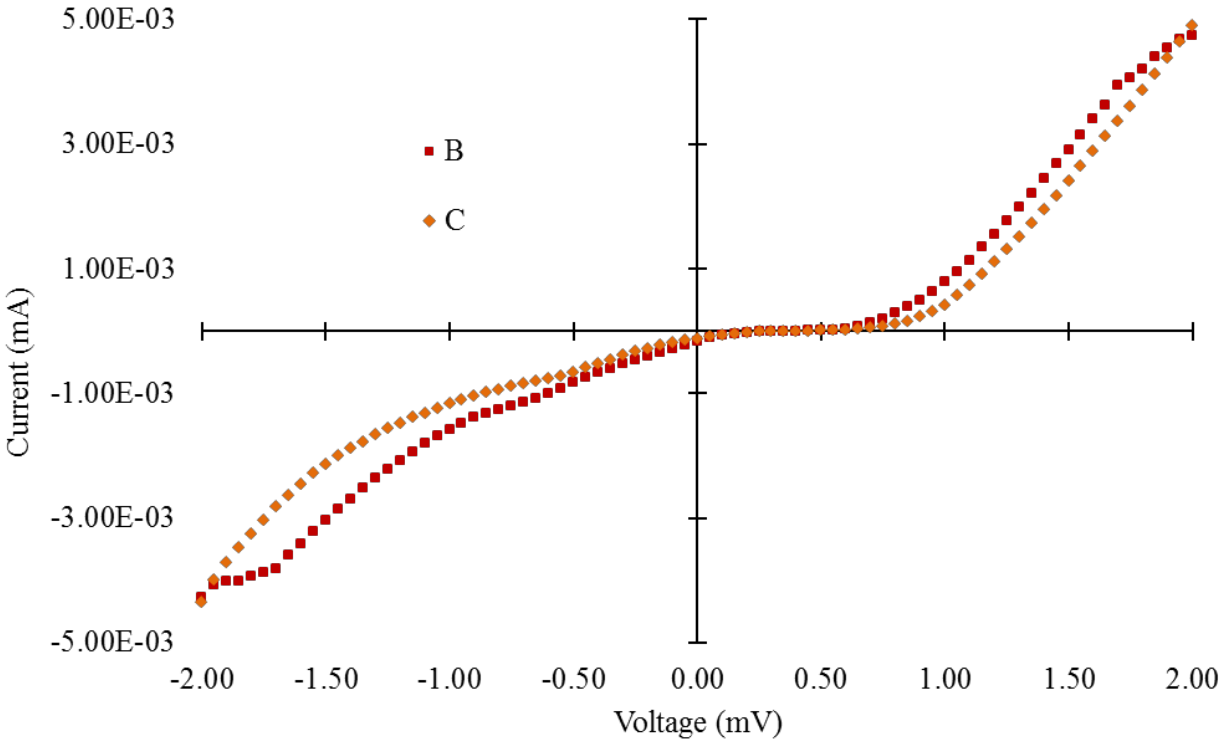

Chart 2. J/V curves for devices using dyes B and C under the light of a solar simulator.

Conclusion

As previously stated, it is known that the band gap of the dye plays a role in DSSC performance. This is the basis for a hypothesized reason for the YLD-124's underperformance in the devices compared to the other dyes: it has a lower band gap. The conduction band edge of TiO_2 is at -4.26 eV and the redox potential of the electrolyte used is at -4.87 eV. This means that the dye used must at least absorb light of 0.61 eV to even operate.

However, absorbing light at this energy by no means guarantees operation. The absolute energy levels of the dye could be shifted so that the HOMO is above the energy of the electrolyte or the LUMO is below the TiO_2 conduction band. Since YLD-124 yielded a negative V_{OC}. It seems likely that for YLD-124 one of these scenarios is the case. Increasing the band gap of the dyes does increase the probability of the absolute energy levels of the dyes matching the energy levels of TiO_2 and electrolyte appropriately however. With this, one can claim that chromophores with larger band gaps don't guarantee better performance but show a trend of better performance.

A second hypothesized reason for the poor results of YLD-124 is that it lacks a carboxyl or hydroxyl group. As stated earlier, PCET is believed to play a role in electron transfer in DSSCs. Since YLD-124 does not have any functional group that could possibly be proton donating, it cannot possibly participate in PCET on its own. This may be hindering the electron transfer between the YLD-124 and the TiO_2 nanoparticles, causing the hole and electron of the exciton formed by photoexcitation to recombine.

To determine why the devices using YLD-124 as its chromophore had poor performance, we want to synthesize more chromophores. Some of these chromophores will be synthesized to absorb light at energy close to that of light absorbed by YLD-124, done by having longer pi-conjugate chains, as well as allow PCET by possessing a carboxyl group in the electron acceptors. Other dyes will be synthesized with shorter chains and without carboxyl groups at the electron-accepting groups

with the purpose of absorbing higher energy light and lacking the ability to perform PCET.

Another important avenue of study is the creation of dyes with the replacement of the I^-/I_3^- electrolyte in mind. One of the current issues with DSSCs is the use of this electrolyte because it is corrosive to gold, silver, and copper. I^-/I_3^- is also a solution-based electrolyte, making it non-ideal to use in a device whose purpose is to be out in the sun at all times.[14] With the change in electrolyte to either noncorrosive solutions or even solid state materials come changes in the redox energy. Because of this, it would be advantageous to develop an understanding of the absolute energy values of molecular orbitals of DSSC molecules and their bandgaps so that dyes can be adapted for electrolyte replacement.

References

1. U.S. EIA International Energy Statistics. http://www.eia.gov/countries/data.cfm (accessed August 20, 2012).
2. Lewis, N. S. Powering the Planet. *MRS Bulletin*. 2007, *32*, 808-820.
3. *Renewable Global 2010 Status Report*; Renewable Energy Policy Network (Ren 21), 2010.
4. *Electric Power Monthly*; U.S. Energy Information Administration, U.S. Department of Energy, July 2012
5. Reid, P. J. *Organic Photovoltaic Technology*, Hooked on Photonics Program, Seattle, WA, June 28, 2012.
6. *Best Research-Cell Efficiencies*. Report for National Renewable Energy Laboratories: Golden, CO, July 2012.
7. Gratzel, M. *Nature*. 2001, *414*, 338-344.
8. Nattestad, A. *et al*. *Nanotechnology*. 2008, *29*, 1-9.
9. Schrauben, J. N. *et al*. *Science Mag*. 2012, *336*, 1298-1301.
10. Yum, J-H. *et al*. *Nat. Comm*. 2012, *3*, 1-8.
11. Dalton, L. R. *et al*. *Org. Thin Films Photon. App*. 2010, *1039*, 13-33.
12. Tsao, H. N. *et al*. *ChemSusChem*. 2011, *4*, 591-594.
13. Smestad, G. P.; Gratzel, M. *J. Chem. Ed*. 1998, *75*, 752-756.
14. Chung, I. *et al*. *Nature*. 2012, *485*, 486-489.

Ackowledgments

I would like to thank the Hooked on Photonics program, all members of the Dalton group, Robb Wallace, David Ginger, and Michael Salvador. Funds for this research were provided by the Center on Materials and Devices for Information Technology Research (CMDITR), and the NSF Science and Technology Center No. DMR 0120967.

Payton Ward is an incoming junior at the University of Washington majoring in chemical engineering. After graduation Payton plans to pursue a PhD in either chemical or material science engineering.